POLITECNICO DI TORINO

Master's Degree in Electrical Engineering

Master's Degree Thesis

Feasibility study for planning of a large scale photovoltaic generation plant in electrical networks.

Supervisors

Prof. FILIPPO SPERTINO

Prof. FRANCISCO DIAZ GONZALEZ

Candidate

DAVIDE BENEDETTI

02-2025

Abstract

The primary objective of this thesis is to conduct a feasibility study for a large-scale photovoltaic plant designed to work alongside traditional non-renewable energy sources in electricity generation. The ultimate goal is to improve the quality of life from both a social and an economic perspective, without ignoring the environmental impact.
In particular, the study is structured as follows: after an accurate review of the relevant scientific literature, a simulation model of a photovoltaic generation system is developed. This model enables a comparative analysis of different plant topologies, assessing their efficiency and adaptability to various operating conditions.
The proposed model will be implemented using the PLECS simulation software, incorporating the key components of a photovoltaic system. These include a detailed model of a photovoltaic module to simulate its behavior under different irradiance and temperature conditions, as well as the closed-loop control of a three-level three-phase inverter specifically designed for solar power generation.
The data obtained from the simulations will be analyzed to compare the different topologies under consideration, with the aim of identifying the most efficient solution in terms of both economic and functional performance.

ACKNOWLEDGMENTS

"I sincerely want to thank all the people who have supported me and stood by my side during the last few years in the academic journey for my master's degree. They have allowed me to reach this goal, overcoming all the unexpected challenges and insecurities that would otherwise have slowed me down and made things more difficult. In Turin, I found genuine people who made me forget the distance from home and helped me grow as a person. During my experience abroad, I met authentic people who taught me a new perspective and gave me unforgettable memories that will last a lifetime. But above all, I am grateful to my family and loved ones back home, who, despite the distance, have always supported me and believed in me. From the deepest part of my heart, thank you all."

Davide.

Table of Contents

List of Tables

List of Figures

Chapter 1

Introduction

1.1 International overview on Photovoltaic Generation

The production of useful processes from renewable sources represents one of the future pillars to create a more sustainable society, in which the development of humanity grows without neglecting its impact on the environment and social tissue. Nowadays, the generation of electricity from renewable sources has become widespread and represents a rapidly expanding industry worldwide.

The Climate Change is a reality that cannot be underestimated, requiring to implement policies aimed at reducing the environmental impact of human activities. In 2023, photovoltaic technology maintained its position as the fastest growing energy source worldwide, exceeding both renewable and non-renewable alternatives. Data collected from the IEA PVPS [1] indicate that 446 GW of new PV capacity was added over the 2023, representing an increase of 85% compared to the previous years (fig. 1.1).

[1] Photovoltaic Power System Program of International Energy Agency

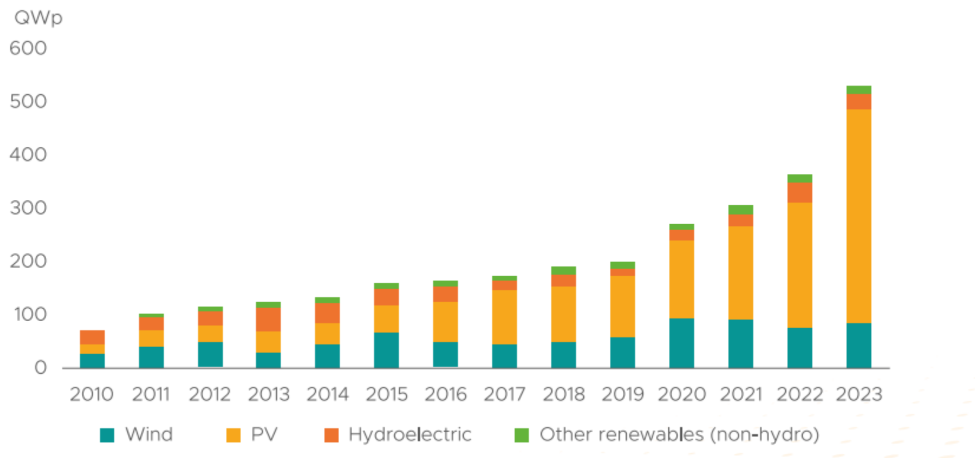

Figure 1.1: Renewable installed capacity, by IRENA

As it is possible to predict, China guides the photovoltaic expansion in 2023 with an increase of the installed capacity in 2023 of 235.5 GW, followed by the European Union with 55.9 GW and the United States with 29.6 GW.
According to IRENA [2], solar PV accounted for 37% of the total renewable generation capacity worldwide, making it the most significant renewable generation source.

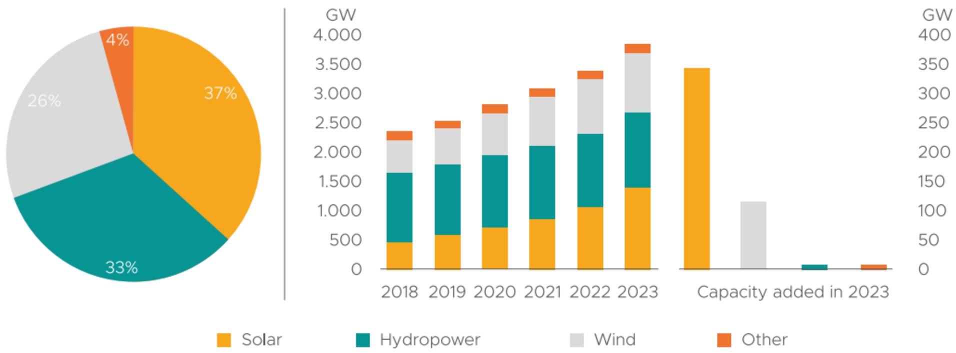

Figure 1.2: Renewable added capacity up to 2023, by IRENA

By 2023, global cumulative photovoltaic capacity had risen to 1,624 GW, reaffirming the dominant role of solar energy in the renewable sector. China maintains its position as the global leader, with an total installed capacity of 662 GW, followed by the European Union with 268.1 GW and the United States with 169.5 GW.

[2] International Renewable Energy Agency, build of a cooperation of over 169 different countries

In particular, India has outpaced Japan to claim fourth place, reaching 95.3 GW compared to Japan's 91.7 GW.
Within the European Union, Germany remains at the forefront with 81.6 GW of installed capacity, while Spain follows with 37.6 GW. Italy (30.3 GW), France (23.5 GW), and the Netherlands (22.4 GW) complete the ranking, reflecting the continued commitment of the continent to photovoltaic expansion.

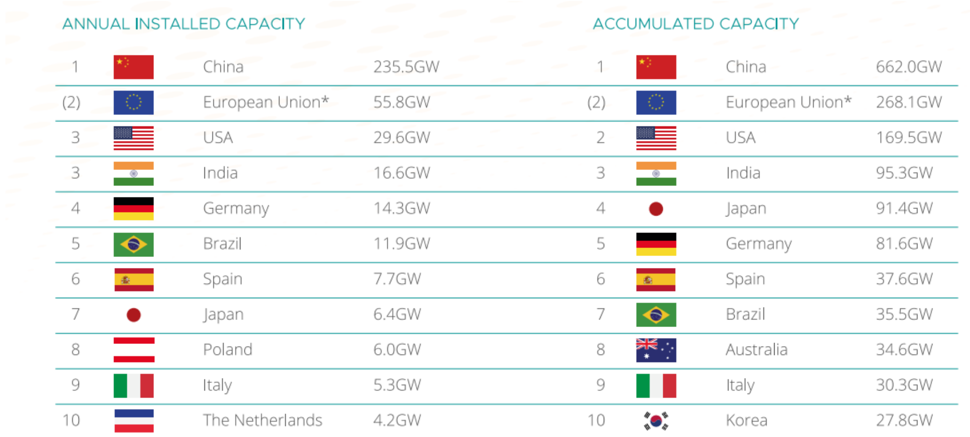

ANNUAL INSTALLED CAPACITY			ACCUMULATED CAPACITY		
1	China	235.5GW	1	China	662.0GW
(2)	European Union*	55.8GW	(2)	European Union*	268.1GW
3	USA	29.6GW	2	USA	169.5GW
3	India	16.6GW	3	India	95.3GW
4	Germany	14.3GW	4	Japan	91.4GW
5	Brazil	11.9GW	5	Germany	81.6GW
6	Spain	7.7GW	6	Spain	37.6GW
7	Japan	6.4GW	7	Brazil	35.5GW
8	Poland	6.0GW	8	Australia	34.6GW
9	Italy	5.3GW	9	Italy	30.3GW
10	The Netherlands	4.2GW	10	Korea	27.8GW

Figure 1.3: Top 10 countries by highest annual and cumulative installed capacity, by IEA PVPS

1.2 General overview about the Renewable Energy Market in Spain

To better understand the main topic of this project, could be useful to describe the impact of the renewable energy market in Spain in recent years, highlighting the fundamental role of photovoltaic generation.
In 2023, as widely described in [1], the Spanish photovoltaic market exhibited signs of stabilization after years of rapid expansion. A total of 6,939 MW_{DC} (5,783 MW_{AC}) of ground-mounted photovoltaic capacity were installed, reflecting a 26% growth compared to 2022. In contrast, the self-consumption segment experienced a contraction, with newly installed capacity estimating of 2,047 MW_{DC} (1,706 MW_{AC}), representing a decrease 32% to the previous year. Despite this downturn, the overall installation trends suggest that the sector is reaching equilibrium after the record-breaking deployment of 2022.

Looking ahead, the outlook for ground-mounted photovoltaic installations remains positive. By 2023, a substantial volume of photovoltaic capacity was undergoing administrative authorization. In July 2024, 28 GW of photovoltaic projects had been approved for construction, accounting for approximately 90% of all permits issued for new renewable energy capacity.
From a legislative perspective, several key regulatory measures have been introduced at the European level to support the long-term development of PV. In January 2023, the European Commission launched the Green Deal Industrial Plan [2], a strategic initiative aimed at enhancing the competitiveness of European industries in the transition toward net zero emissions. Within this framework, the European Union has implemented multiple actions to accelerate these objectives:

- The Net-Zero Industry Act [3], which seeks to scale up clean technology manufacturing to fulfill at least 40% of the EU's requirements by 2030, streamline regulatory procedures, and attract investment.
- The Critical Raw Materials Act [4], designed to secure a stable and sustainable supply of essential raw materials, such as lithium, cobalt, nickel, and gallium, critical to the renewable energy value chain. This legislative measure aims to strengthen Europe's domestic industry, increase supply chain resilience, and create a circular, sustainable economy

Together, these regulatory frameworks provide a solid foundation for the continued expansion of Spain's photovoltaic sector, ensuring its alignment with broader European energy transition objectives.

In 2023-2024 [5], the share of electricity generated from renewable sources in Spain remained consistently above 50%. This marks a record for the Iberian country, which formally approved its updated National Integrated Energy and Climate Plan (PNIEC), representing one of the most advanced European countries.

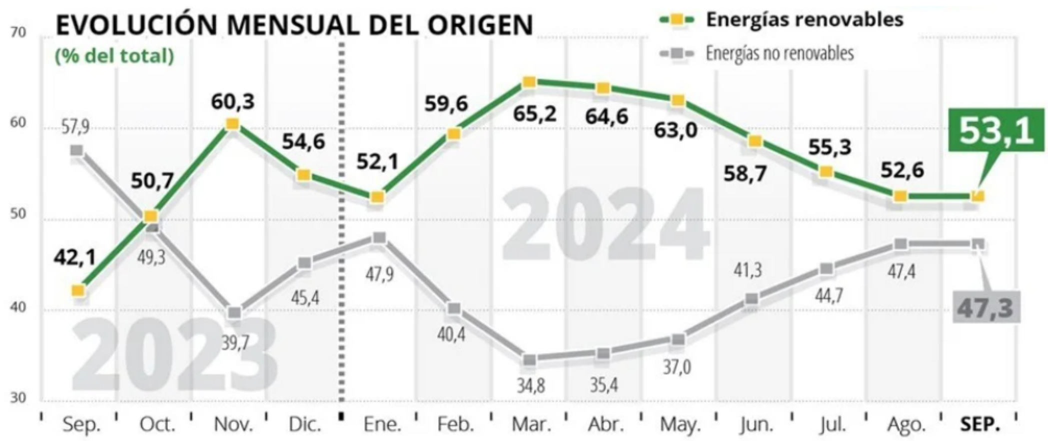

Figure 1.4: Renewable energy generation in Spain 2023-2024, by Appa

The moving average for the past year, from October 2023 to September 2024, establishes the share of electricity from renewable sources at 56.8%, as described in fig 1.4.
According to [5] , this is a significant increase, primarily attributed to two factors:

- On the one hand, there was a notable increase in photovoltaic generation (+22.3%), achieved due to the growth in installed capacity. Although these figures represent a slowdown compared to 2022 and are expected to decline further in 2024, they remain substantial enough to contribute significantly to the record levels of renewable electricity generation.

- Secondly, hydroelectric generation saw a remarkable increase (+67.5%), mainly due to exceptionally high rainfall in 2024. However, this growth is expected to have lasting effects. When adjusting the data to exclude extraordinary precipitation levels in 2024, renewable energy sources are still projected to cover 54% of electricity consumption an increase of four percentage points compared to previous years.

Looking at the National Integrated Energy and Climate Plan [6], it sets a target of 81% renewable electricity generation by 2030 over the total energy production. To achieve this, the Plan establishes ambitious installed capacity goals for 2030: 76 GW of photovoltaic, 62 GW of wind, 4.8 GW of solar thermal and 1.4 GW of biomass. Among these technologies, only PV generation maintains a pace consistent with the goals set for 2030. However, the prediction has to take into account that the electricity demand will increase in the future: PNIEC projects an electricity demand of 358 TWh in 2030, which is 34% higher than the current level. Therefore, specific measures will need to be promoted to electrify and make demand more

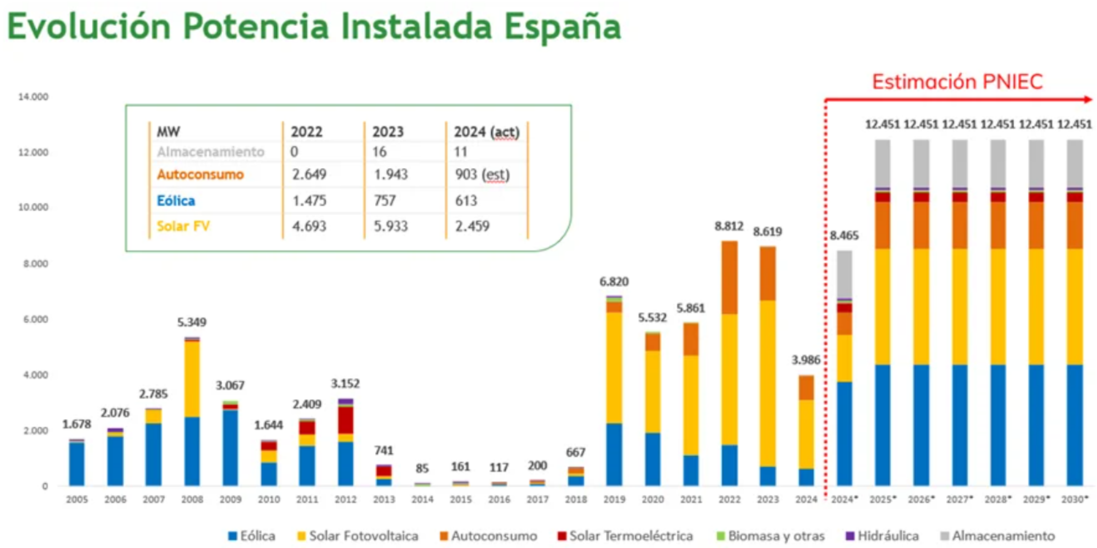

Figure 1.5: Evolution of renewable installed power

flexible.

Equally important will be the path to achieving the storage target, set at 22.5 GW by 2030, given the current interest in the sector. The industry is waiting for specific regulations that will attract investments and foster the development of energy storage in Spain, which will be crucial to integrating the planned renewable capacity in the coming years.

1.3 Operation Principle of a photovoltaic cell

To better understand how a photovoltaic system transforms solar power into useful electrical energy, the basic principles of operation of a solar cell ([7]) will be reported and analyzed in the following section.
The solar photovoltaic cell is the basic element of a solar system capable of direct conversion of sunlight into electricity. The cell is made of mono or poly-crystalline silicon, which presents a tetravalent atomic structure crystal and the ability to use its 4 valence electrons to react and create chemical bonds with surrounding atoms. To realize a cell that works as a unidirectional switch (diode operation), the silicon has to be "doped" with the addition of trivalent elements (like boron, with a lack of a negative charge) and pentavalent elements (like phosphorous, with an excess of negative charge). The structure is composed by two layers of different doped silicon (called respectively *n-type* and *p-type*) is the P-N homo junction and is in

charge of solar generation.

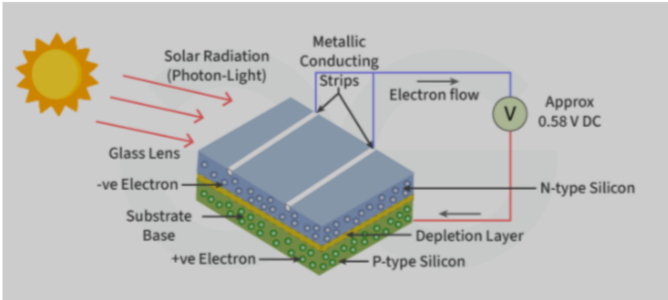

Figure 1.6: Structure of the P-N silicon based junction

When the two layers are attached to realize the junction, the majority carriers of the *n-type* layer (electrons) and the *p-type* layer (holes) diffuse in the opposite part, forming a depletion region without mobile carriers.
This "potential energy barrier" created in such a way does not allow the junction to conduct electricity unless a forward bias is applied: As a result of this configuration, the junction acts as a rectifier (diode operation). To obtain a current, the junction must receive enough energy to allow the electrons to jump the potential barrier. This energy could be given by photons that are able to promote electrons into the conductance band, resulting in a photo-generated current flowing into the junction.

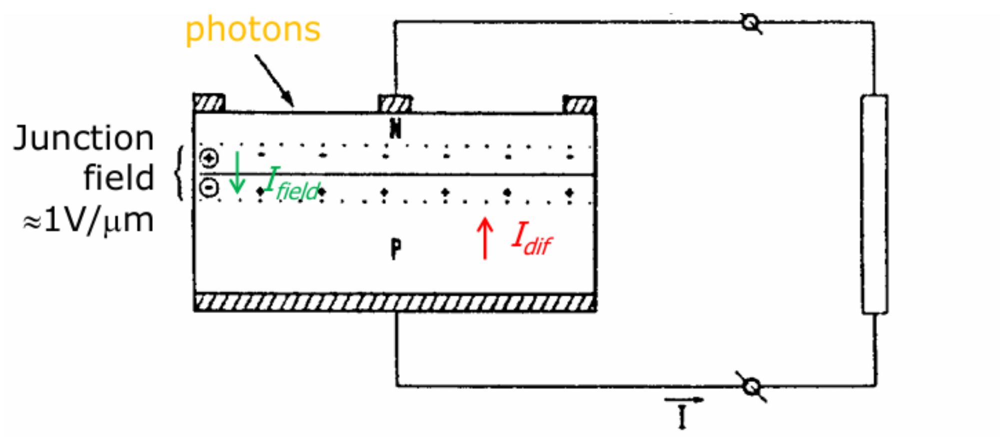

Figure 1.7: Solar cell under sunlight

Looking at the mathematical relationship between the physical quantities, the reaction can be described as:

$$E_{ph} = h \cdot \frac{c}{\lambda} \geq E_{gap} \tag{1.1}$$

in the eq. 1.1 is shown that the energy of the electrons E_{ph}, which depends by the Plank constant h, the speed of light c and the wave-length λ, has to be higher than the energy gap created by the depletion region, in order to permit the current to flow. Is also true that not each electron that impacts the junction has enough energy to win the barrier, leading to losses and thermal overheating.

Losses in the Photovoltaic Effect

In general, the photovoltaic effect presents intrinsic losses that are unavoidable, such as

- Photon energy-related losses: the electron-hole pair can be generated only by photons with the right amount of energy. If they have a lower or an higher value (everything above ultraviolet), the solar power is dissipated as heat;
- Reflection related losses: not all incident photons penetrate into the cell, but a part is reflected and vanishes in the frontal electrode. This effect can be reduced by the surface texturization of the cell;
- Recombination related losses: occurs when the recombination between holes and electrons happens before the separation caused by the potential barrier.
- Voltage drop-related losses: caused by the cell resistance that depends on the type of construction of the PN-junction, and the materials employed.
- Leakage current-related losses: related to the non perfect electric isolation of the four lateral surfaces of the cell.

1.4 Solar Cell Equivalent Circuit

For the realization of a complete model capable to simulate a solar generation plant, the crucial aspect is to describe the behavior of the solar cell under light and dark conditions, using an equivalent circuit that links all the important internal variables with the input of temperature and irradiance.
In general, when the cell is under direct sunlight, it is possible to model it as a current generator in parallel with a diode (rectifier behavior). The photo-generated current is proportional with an exponential evolution to the irradiance G and the ambient temperature at which the cell works. The precision of the model depends on the number of parameters used for the equivalent circuit [7].

1.4.1 3 - Parameter Equivalent Circuit

The 3 parameters solution is the simplest one and is described in fig. 1.8. The current at the output terminals of the cell is dependent only by the photo-generated current and the current absorbed by the diode.

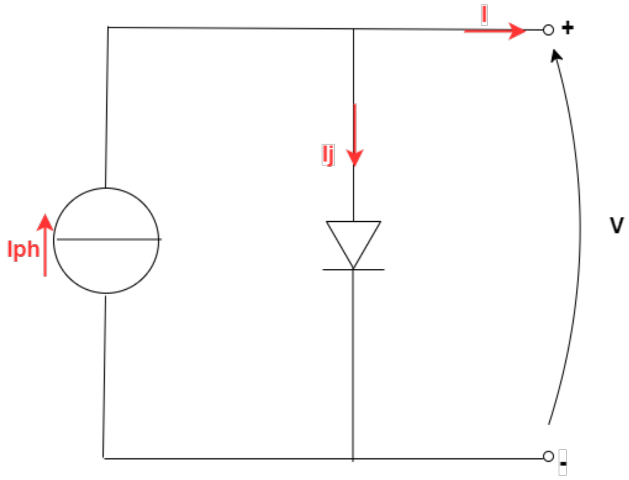

Figure 1.8: 3-Parameters Equivalent Cell Circuit

Looking at the current balance, it can be noticed that:

$$I = I_{ph} - I_j \tag{1.2}$$

where the junction current is described by the exponential relation:

$$I_j = I_0 \cdot (e^{\frac{q \cdot V_j}{mkT}} - 1) \tag{1.3}$$

in which I_0 is the inverse saturation current, q is the electron charge $(1.602 \cdot 10^{-}19)$, V_j is the voltage across the junction (in this case equal to V), k is the Boltzmann constant and m is the quality factor of the junction[3].

The simulation program exploits a solution for the PV equivalent model as the 3 parameters one, since the behavior of the real cell will be described by a custom LUT solution, which calculates the correct current value depending on the manufacturer datasheet of the chosen component.

[3]The quality factor of the junction has an ideal value 1, and represents the presence of defects in the junction that cause the recombination losses.

1.4.2 5- Parameters Equivalent Circuit

To increase the precision of the equivalent model of the PV panel, without enhancing the computational burden of the simulation, a 5-Parameters circuit can be used. As it possible to observe in fig. 1.9, this solution takes into account the series resistance R_s that depends on the number of busbars in the front connection and the parallel shunt resistance R_{sh} that depends on the isolation level of the lateral surfaces.

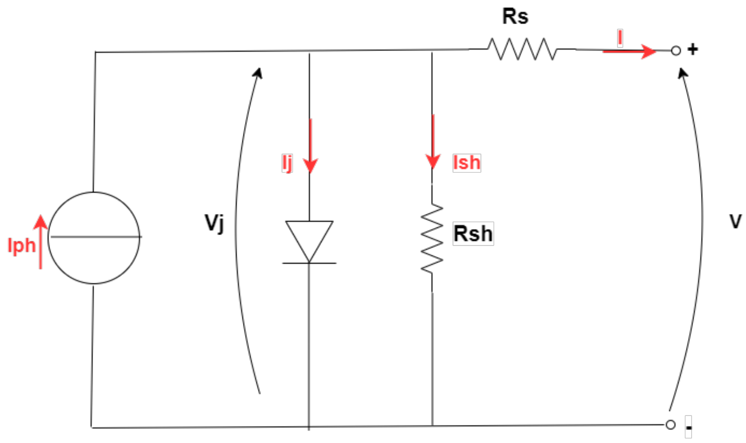

Figure 1.9: 5-Parameters Equivalent Cell Circuit

The balances of current and voltage change from the previous case as following:

$$I = I_{ph} - I_j - I_{sh} = I_{ph} - I_j - \frac{V_j}{R_s h} \tag{1.4}$$

$$V = V_j - R_s \cdot I \tag{1.5}$$

using the eq.1.3 and the current balance in 1.4 is possible to obtain the voltage at the junction

$$V_j = \frac{m \cdot k \cdot T}{q} \cdot ln(\frac{I_0 + I_j}{I_0}) \tag{1.6}$$

and as direct consequence the output voltage of cell using eq. 1.5

$$V = \frac{m \cdot k \cdot T}{q} \cdot ln(\frac{I_0 + I_j}{I_0}) - R_s \cdot I \tag{1.7}$$

This procedure permits to calculate the I-V characteristic by choosing a specific level of irradiance G and temperature (the irradiance affects the saturation current I_0).

The eq. 1.7 describes the relation between the output voltage and the current of the cell. If this relation is plotted, the I-V characteristic will be found:

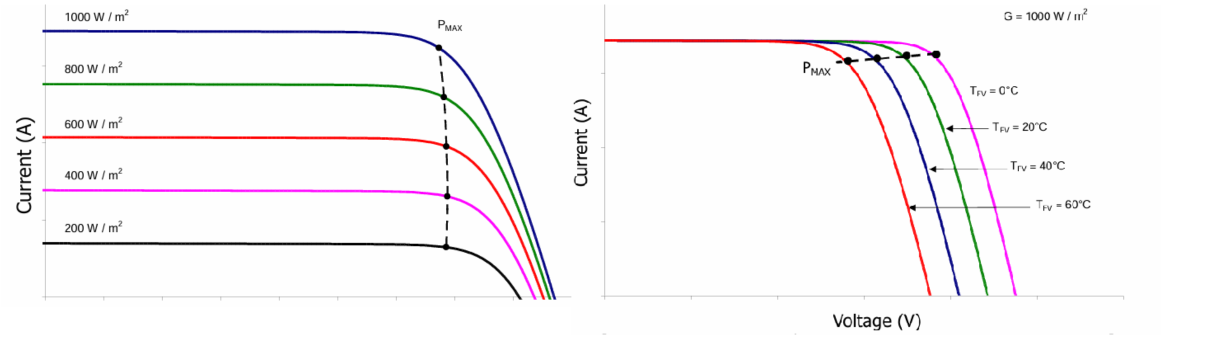

Figure 1.10: General I-V characteristic of a PV panel

in fig. 1.10 is reported the dependence of the I-V characteristic on the irradiance (starting from the STC[4] value of 1000 W/m^2) and the temperature (STC value of 25 °C). In particular, is possible to observe that I_{sc} and I_{mpp} [5]change roughly in proportion with the incident irradiance, instead V_{OC} and V_{mpp}[6] have minor variations.
If is the temperature that change, the most affected parameters are V_{OC} and V_{mpp}, with a lower variation of the currents. The percentage of variation depends on the materials used for the construction of the cell.

[4]Standard Test Conditions

[5]I_{sc} and I_{mpp} are respectively the short circuit current obtained when the load voltage is zero, and the maximum power point current

[6]V_{OC} and V_{mpp} are respectively the open circuit voltage and the maximum power point voltage

Chapter 2

LS-PVPP Structure

2.1 State of the Art about LS-PVPP Topology

Following the available literature, several different structures can be selected to realize a PV plant, relying on the available power, the dimension and the covered surface. Usually, they can be distinguished into: centralized, string, multi-string and AC modular. Each of them presents advantages and drawbacks, depending on which aspect of the analysis is taken into account, from the conversion efficiency at fixed power to the realization cost [8]

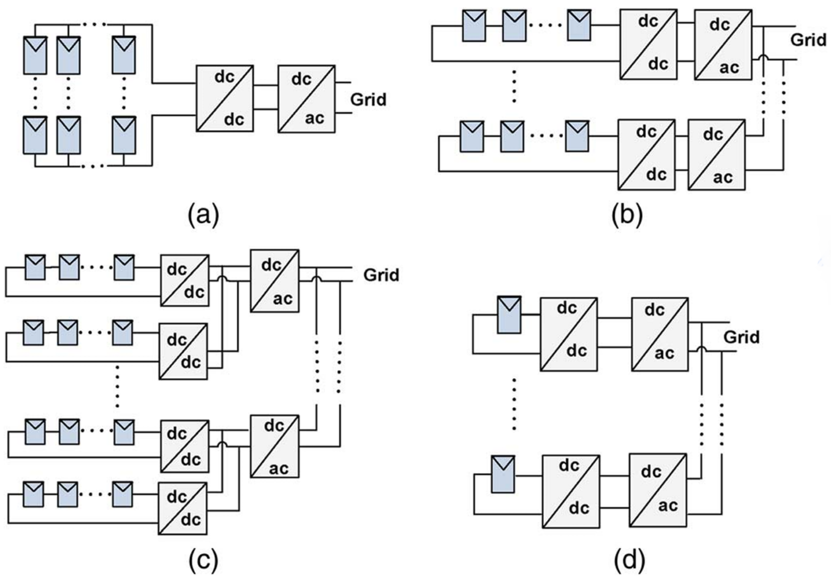

Figure 2.1: Graphic description of different topologies: (a) Centralized; (b) String; (c) Multi-string; (d) Modular

2.1.1 Centralized Topology

In the centralized configuration, PV panels are arranged in series to create a string with a predetermined voltage level (fig. 2.1 (a)). These series are then connected in parallel to produce the required power output for the PV plant. The power generated is delivered to the grid through a single high-power DC/AC converter. Typically, the first stage involves a DC/DC converter controlled with MPPT technique to regulate the PV system's operating voltage in case of shading effect or mismatch. This type of configuration has to face less cost due to the presence of a single large high-power inverter, but its efficiency decreases proportionally with the size of the plant.

2.1.2 String Topology

In the string configuration, the whole energy system is divided into independent subsections called PV strings, that are formed by series-connected PV panels (fig. 2.1 (b)). Each of them has a dedicated inverter (double-stage conversion formed by a DC/DC for MPPT following and a DC/AC low-power grid connection). This solution improves the reliability of the system facing mismatch or shading events, but with an increase in general cost, due to the fact that each PV string needs a suitable inverter connection necessitating higher capital for the initial investment.

2.1.3 Multi-string Topology

It represents a sort of compromise between centralized and string topology: to increase the overall efficiency, more than one single centralized inverter is used, but each conversion unit is associated with more than one PV string, to decrease cost in comparison of the string topology (fig. 2.1 (c)). This solution can be also used in DC power transmission systems, improving the capability of large-scale PV power plants that support this type of transmission.

2.1.4 Modular Topology

In the modular configuration, each PV panel mount directly a low power micro-inverter and each panel is connected to the system via an AC link (fig. 2.1 (d)). Reliability and efficiency are high, but this structure is not feasible for a large-scale plant, due to the presence of enormous surfaces of PV panels, which make initial investment too expansive.

2.2 Topology preliminary confront

The preliminary comparison distinguishes across several aspects, such as the general characteristics, average power losses and costs. The first category, general characteristics, evaluates attributes such as robustness, reliability, flexibility and MPPT efficiency. For example, the central topology is characterized by low levels of reliability, flexibility, and MPPT efficiency. However, it demonstrates greater robustness compared to other topologies.

The second category, power losses, collects mismatching losses, switching losses, and both AC and DC losses. Mismatch losses are unavoidable in any photovoltaic array and arise due to factors such as uneven PV string degradation, shading, cloud cover, dust accumulation, cooling efficiency, and MPPT performance. In this comparison, the central topology typically experiences higher mismatching losses as multiple strings are connected to a single inverter. Switching losses depend on the inverter's components and control strategies (which are taken into account in the model with an adequate thermal equivalent). The DC losses are higher in the centralized topology with respect to the others, due to the presence of a high number of parallel connections of multiple strings.

The third category involves the cost caused by installation, land use, length of cables and maintenance on both AC and DC side. The preliminary confront cannot establish the best solution, because costs strictly depend on the chosen location, the technology exploited and several others aspects.

	Central	**String**	**Multi-String**	**Module-Int**
Reliability	L	H	M	V-H
Flexibility	L	H	M	V-H
Robustness	H	L	M	V-L
MPPT ni	L	H	M	V-H
Mismatch	H	V-L	L	V-L
Switching	H	L	M	V-L
DC losses	H	L	M	V-L
AC losses	L	M	M	H
Voltage balance	H	M	L	L
Installation cost	M	H	M	V-H
Maintenance	L	M	H	V-H

Table 2.1: Preliminary topology confront: (very)High, Medium, (very)Low

In general, it can be noted that the central topology has some advantages, such as robustness, low AC losses, more stability on the AC output and maintenance and installation costs more acceptable than the others. On the other hand, the efficiency is higher in the string and multi-string solution but with an increasing number of needed inverters, the costs grow. String and multi-string are similar in general, but the first solution, since presents a low-power inverter for each module array, is preferred if the location of the pv installation has different orientation angles. A result of the preliminary confront looking at the available literature is presented in tab. 2.1

2.3 Power Request from Target Plant

In this section, a performance target is presented using data from a real LS-PVPP. The power profile is given for a specific day (19/07/2020) during the normal operating cycle of the PV plant with a time span of one second, starting from 19:00; all the data given consist of the active power delivered to the grid by all the inverters of the plant. Taking the inverter output as a starting point will be the key to find the best topology that minimizes losses and costs while maintaining the overall performance of the structure. [1]

2.3.1 Active Power Output

The data given from the real plant are summarized in characteristics in fig.2.2, in which it is possible to observe the profile of average solar generation. The plant is formed by 146 inverters (coupled in pair) and, for the sake of simplicity, only two coupled characteristics are plotted. The peak of the production occurs around 14:26, with a maximum generation of almost 2.3 megawatts.

The bell-shaped profile follows the expected generation in a sunny day, reaching the target output value. As it possible to notice, the plot presents some kind of abrupt changes, due to the presence of shading events, like clouds that cover a portion of the PV surface leading to mismatch, showing that even in the best possible conditions for solar generation, it is always true that this resource is not completely controllable. It's also true that, for the given time span in which data are collected, some inverters do not work profitably presenting almost zero generation at the output. In a large scale plant of this kind, a proper optimization

[1]The data taken to start this kind of analysis, are covered by confidential information about the company who produce them and no precise information about how they are collected will be given to respect their status.

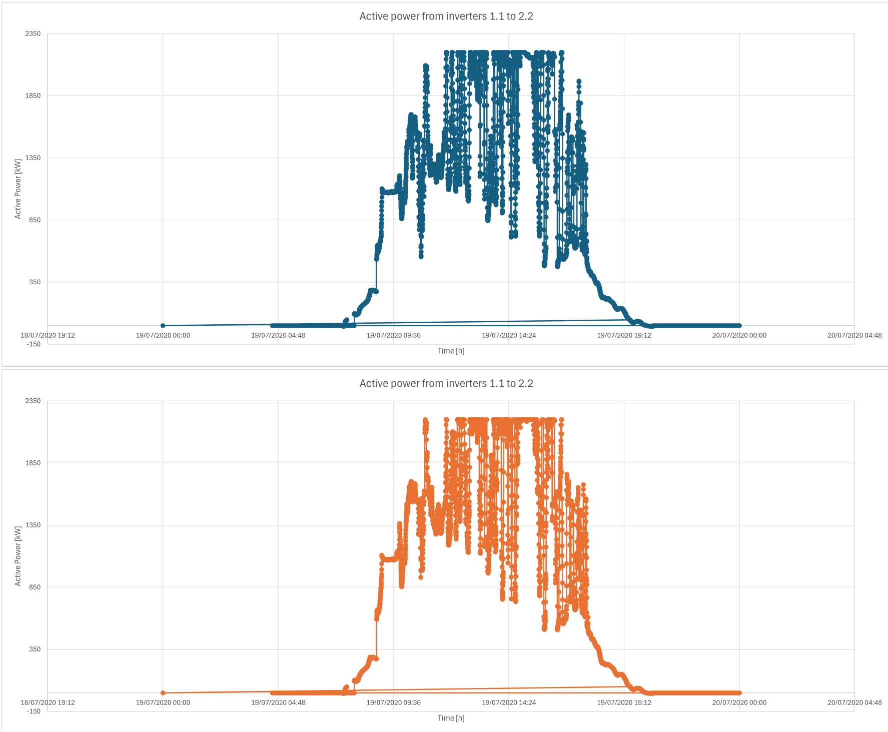

Figure 2.2: Inverters 1.1-1.2 Generation Profile

analysis could be crucial to exploit the resources as better as possible.

The total generation profile, given by the sum of every output of active power of each inverter, is presented in fig. 2.3: the LS-PVPP under analysis reaches a maximum power output of around 260-275 MW.

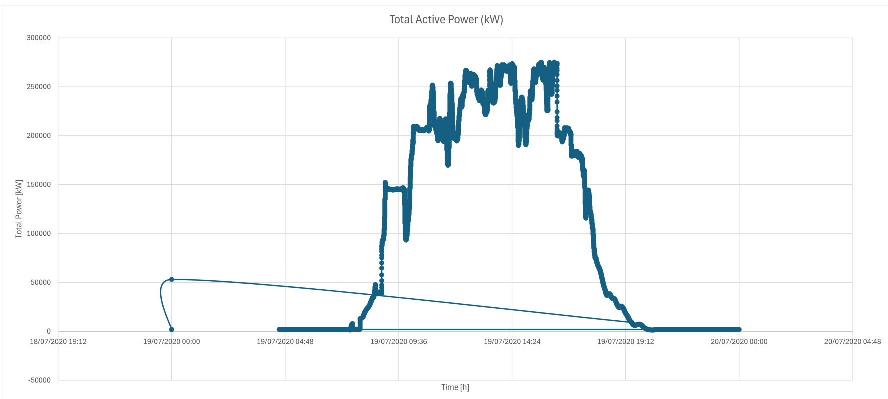

Figure 2.3: Total Generation Profile

2.4 Plant's Inverter estimation

For the design of a photovoltaic system with an active power generation profile as described in the previous section in fig.2.3, the most critical aspect is the selection of a suitable inverter, depending on the chosen topology.
The following inverters, available on the market, exhibit characteristics suitable for the application in question, although there is a substantial difference in their capacities.
The values taken from the components datasheets will be used to calculate key parameters of the system to be simulated, including the equivalent model of the photovoltaic generator, the voltage level on the DC-Link, and the internal switch topology, which are necessary for the thermal model.

2.4.1 Centralized topology inverter

The centralized solution is the most common for the chosen power of the plant, presenting a variety of different and competitive options on the market. The chosen product has to overcome several important aspects such as the possibility to work in the optimal conditions at different temperature level, a suitable range of input DC voltage to perform MPPT strategies and the highest reliability and robustness. The chosen product is the highly advanced and high performance HIVERTER NP-215L Series, produced by HITACHI [9]. Its general specifications are reported in tab.2.2

Model	***HIVERTER NP215L***
Solar PCS Rating AC	2500 kW
DC-AC Conversion System	3 Level High freq. PWM Inverter
Control System	MPPT and AC Current Control

Table 2.2: Centralized Inverter general specifications

Grid Data	Value	Unit
Power Rating	2500(50 °C) - 2700(25°C)	kW
Max AC Current	2223(50 °C) - 2474(25 °C)	A
Output THD	$\leq 3\%$	-
Nominal Output Voltage	650 (AC)	V
Output Voltage Range	650 ± 10 %	-
Output Frequency Range	$50/60 \pm 2\%$	Hz
Peak Efficiency	99%	-
Euro Efficiency	98.6%	-
Power Factor (Adjustable)	0.8 Lead to 0.8 Lag	-

Table 2.3: Centralized inverter Grid side specifications

For the grid connection part, the structure provided by the manufacturer does not include a transformer to adapt the output voltage to the grid level (230 Vrms). The THD represents the Total Harmonic Distortion of the output voltage, which ensures a quality of the power wave injected into the grid inside the restriction imposed by the European community. The power ratings and the maximum allowable current are given with a temperature specification that is related to the ambient working temperature.

PV side	Value	Unit
Max DC Power Loading	2535	kW
MPPT Voltage Range	950-1300	V
Max DC Input Volatge	1500	V
Min DC Input Voltage	950	V
Max Input Current	2688	A

Table 2.4: Centralized inverter PV side specifications

Tab.2.4 and 2.3 are used to define operative parameters useful for the simulation model. The manufacturer ensures a full set of protection devices, such as islanding and temperature protection, ground fault and short circuit detection, breakers, over voltage and temperature both DC and AC and many more.

2.4.2 String topology inverter

The string solution exploits the same concept as the centralized one, but with a considerable reduction of the inverter power size: the idea is to recreate the output, changing the equivalent module configuration to supply the chosen converter. Obviously, to obtain the same result, the number of total requested inverters grows,

with an increase of the installation costs. Therefore, a higher number of inverters has the advantage of increasing overall efficiency when shading or mismatching events occur.
For the string topology, the selected product is the PVI-12.5-TL-OUTD developed by ABB.

Model	***PVI-12.5-TL-OUTD***
Rated Nominal Power	12.5 kW
Topology	String Inverter with MPPT
Number of independent MPPT	2

Table 2.5: String inverter general specifications

The adopted string solution uses two independent MPPT channels and presents a wide range of input voltages, resulting in a functional solution for different levels of available power.

Grid Data	Value	Unit
Max AC Apparent power	13.8	kVA
Max Output AC Current	20	A
Output THD max	2%	-
Rated Output Voltage	320-480	V
Rated Output Frequency	50/60	Hz
Peak Efficiency	97.8%	-
Euro Efficiency	97.2%	-
Power Factor (adjustable)	-0.9: +0.9	-

Table 2.6: String inverter grid side specifications

PV side Data	Value	Unit
Max DC Input Voltage	900	V
Starting DC Voltage	360	V
MPPT Voltage Range	0.7*360 - 850	V
Nominal Input DC Power	12.8	kW
Max DC Input Current	36	A

Table 2.7: String Inverter PV side specifications

2.4.3 Multi-string topology inverter

The multi-string inverter represents a compromise between the centralized solution and the string one: the overall efficiency is increased in case of mismatch or shade, but with a lower use of resources because the number of inverters is lower than the string solution.
The chosen product for the multi-string topology is the SUN2000-50KTL-M0 realized by Huawei:

Model	***SUN2000-50KTL-M0***
Rated AC Active Power	50 kW
Topology	Multi-String Inverter with MPPT
Numbers of independent MPPT	6

Table 2.8: Multi-string Inverter general specifications

The chosen configuration takes advantage of all available independent MPPT channels, in which a PV string with a fixed voltage level is attached. Each MPPT channel can extract the maximum possible power from the string in a independent way, allowing to increase the efficiency if a string is shaded by atmospheric events. All useful specifications are reported in tabs.2.9 and 2.10

Grid Data	**Value**	**Unit**
Max AC Apparent Power	55	kVA
Max Output AC Current	79.4 at 400 V	A
Output THD Max	3%	-
Rated Output Voltage	220/380, 230/400	V
Rated Output Frequency	50/60	Hz
Peak Efficiency	98.7%	-
Euro Efficiency	98.5%	-
Power Factor (Adjustable)	0.8 lead to 0.8 drag	-

Table 2.9: Multi-string inverter grid specifications

PV Side	**Value**	**Unit**
Max DC Input Voltage	1100	V
Max Current per MPPT	22	A
MPPT Operating Voltage Range	200-1000	V

Table 2.10: Multi-string inverter pv side specifications

Chapter 3

PV Plant Sizing

This section focuses on the sizing procedure needed to project a photovoltaic plant of the desired power. The requested application has to follow the output power reported in the previous section, in fig.2.3, for the total number of inverters installed. The suggested procedure consists of the following steps:

- Estimation of a possible real location for the plant based on the total amount of installed power, the irradiance and temperature conditions.
- Estimation of the power dimension of the PV plant, starting from the AC output given and finding the respective matching DC input.
- Estimation of the base unit of the module (series and parallel), depending on the topology chosen.
- Calculation of the useful parameters for the simulation model, after the selection of a suitable PV module on the market.

A solar photovoltaic plant with installed power over 270 MW could represent a crucial solution in the energy mix, satisfying the needs of many people from a social and economic point of view, increasing the quality of life and allowing the development of a florid energy community.

3.1 PV Plant Site Estimation

A power plant with a considerable dimension needs a specific site in which the best possible irradiance, meteorological and temperature conditions are met for the majority of time.
To select a location suitable for the purpose of this project, updated documents about the penetration of solar and photovoltaic generation into the Spanish electricity market are taken into account.
In particular [5] and [1] provide a division of the renewable energy mix at the end of 2023, presented in fig. 3.1.

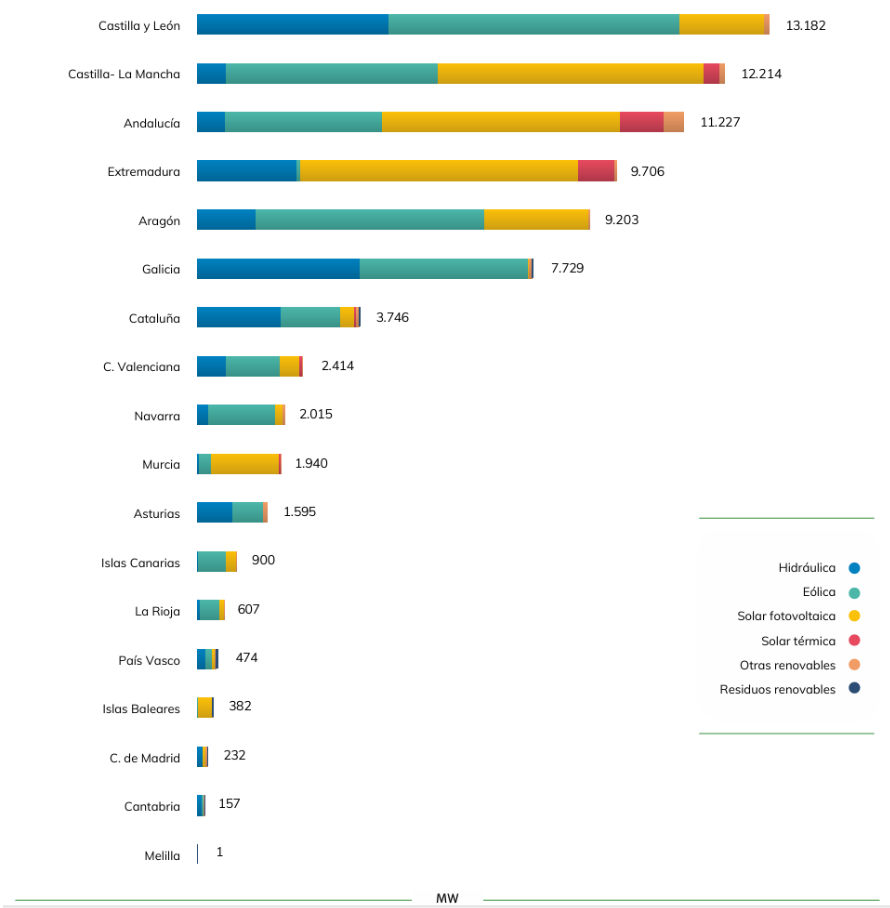

Figure 3.1: Regional Renewable Energy mix in Spain at the end of 2023

Focusing on the solar photovoltaic sector, fig. 3.2 presents the capacity map of the Spanish regions in ground-mounted plans.

The total installed capacity is higher in the center-southern region, near the

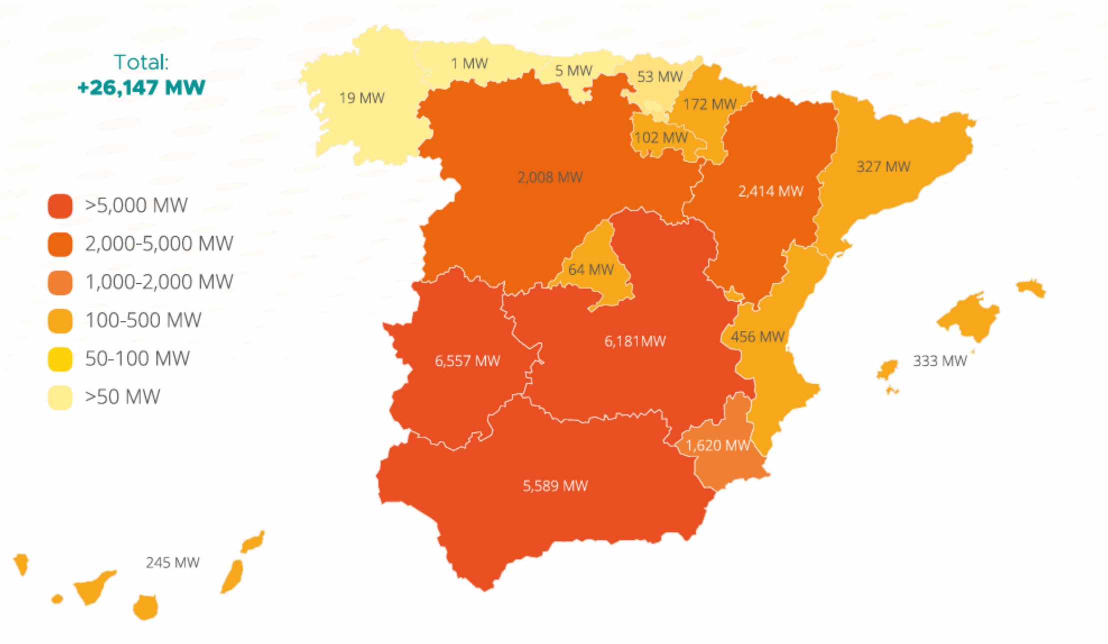

Figure 3.2: Regional Photovoltaic capacity in ground-mounted plants, end of April 2024

equatorial zone, in which temperature and irradiance conditions are perfect for solar generation. A high-power solar plant (more 200 MW) usually needs a custom design structure to inject power into the national grid, which works better if the plant is close to the distribution center. A large and unobstructed area close to an industrial pole would be perfect for the purpose of this application, in which the generated electricity can be employed directly for useful processes, reducing the storage operation at minimum.

Crossing the data of regional solar generation with the ambient data, obtained using the PVGIS[1] software, the selected location is near Seville in the western part of Andalusia, which has optimal conditions on average. The most relevant temperature and irradiance values, extracted from the solar European database, are reported in tab. 3.1.

[1]Photovoltaic Geographical Information System, PVGIS developed by the European Commission Science Hub

Location Data : Seville (Spain)	Value	Unit
Max Recorded Temperature	41	$°C$
Min Recorded Temperature	1	$°C$
Max Recorded Irradiance	1129,2	W/m^2

Table 3.1: Relevant Ambient Condition in Seville 2023

3.1.1 PVGIS data evaluation

The European Solar Database is a data repository that enables the retrieval of a comprehensive set of accurate measurements of temperature, solar irradiation, and wind speed at any given time. It provides a temporal resolution of months, days, and even hours. In the development of the model, the average values sampled over predefined time intervals were considered, and their trends are presented below.

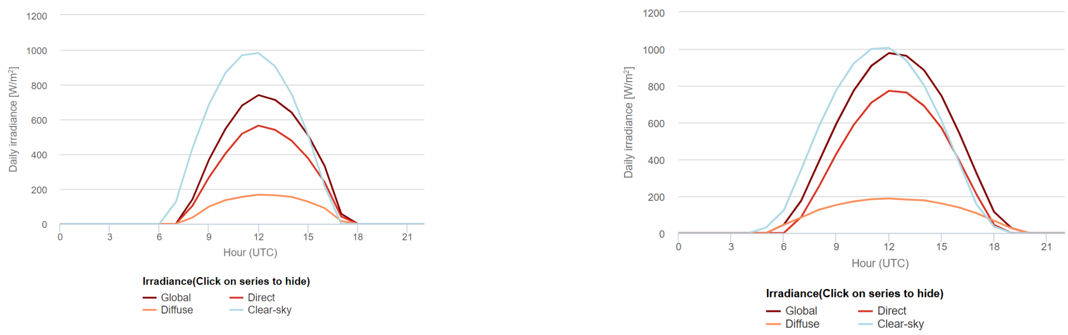

Figure 3.3: Average Irradiance Daily profile confront January-July 2023

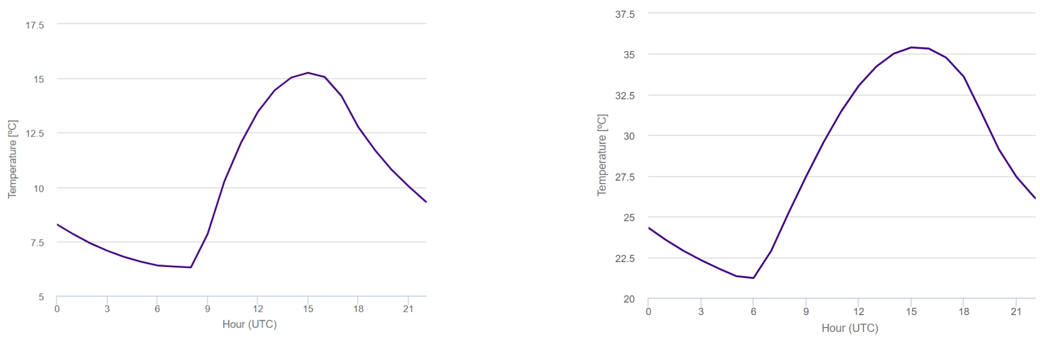

Figure 3.4: Average Temperature Daily profile confront January-July 2023

The confront presented in fig. 3.3 and fig.3.4 shows the average difference between the irradiance profile in the most significant months of 2023 January (which has the lowest average irradiance and temperature recorded) and July (which has the highest average irradiance and temperature recorded).
The peak of irradiance is reached approximately in a range between 12-13 with the classical bell-shaped profile of solar generation. The most significant values are reported in tab. 3.2

PVGIS fixed plane measures	January	July
Peak Global Irradiance $[W/m^2]$	740	978
Peak Clear-Sky Irradiance $[W/m^2]$	981	1006
Peak Temperature $[°C]$	15.26	35.4

Table 3.2: PVGIS monthly confront values

The Clear-sky value surpass the STC value of 1000 W/m^2 due to the proximity of the site to the equatorial zone, in which the irradiance conditions are optimal for solar generation. This is important to keep in mind, during the sizing of the PV Panel structure, for the calculation of NPR that is performed after this section.

Looking at the PVGIS estimation more in detail, is possible to obtain the irradiance and temperature profiles in a specific day, that can result useful for the given power data set reported in the previous chapter in fig. 2.2.

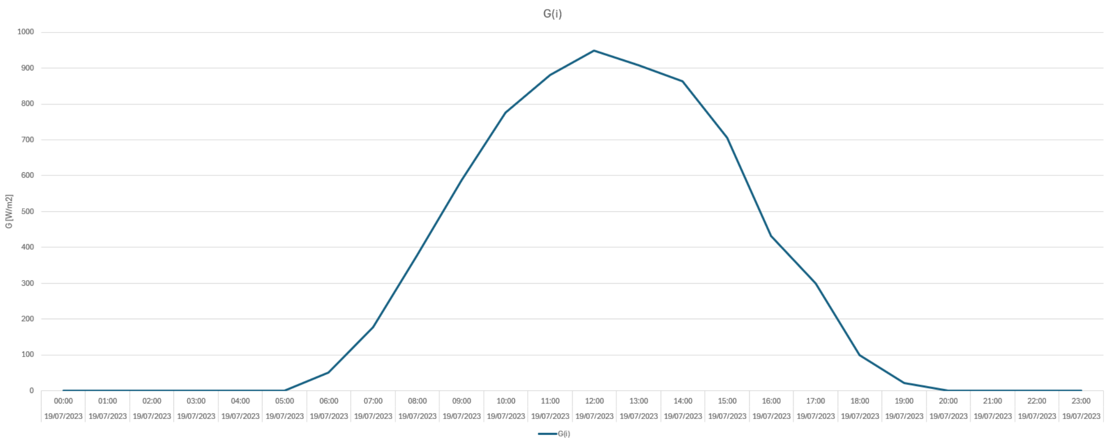

Figure 3.5: Irradiance profile on target day 19/07/2023

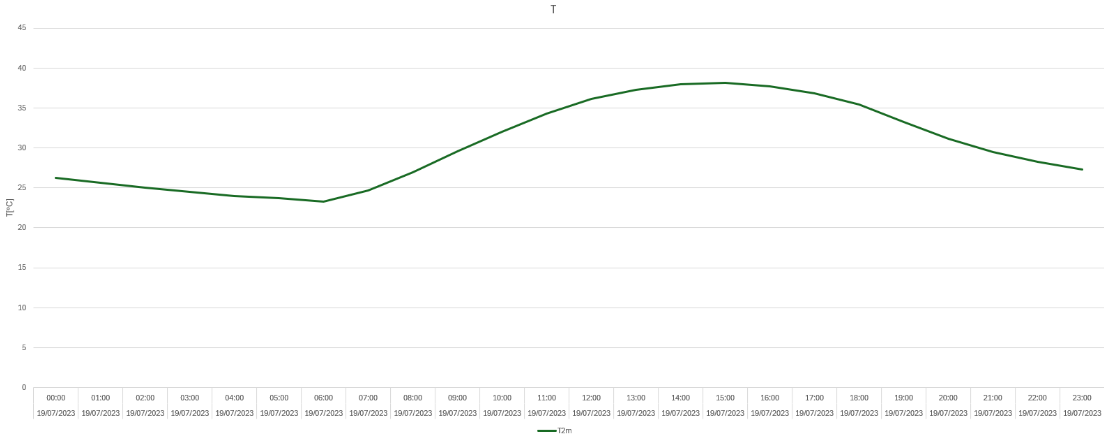

Figure 3.6: Temperature profile on target day 19/07/2023

3.2 PV Plant Power Dimensions Estimation

Looking at the power specification described in the fig. 2.2 the AC output, represented as a variation of the amplitude of the 3-phase power injected into the grid, is the starting point for the sizing procedure.
The active AC power depends on the apparent power of the converter(S_{AC}) and the power factor of the application ($cos\phi$), following the must-known relation:

$$P_{AC} = S_{AC} \cdot cos\phi \tag{3.1}$$

in which, for the considered application, the power factor is taken equal to one, representing the plant as an ideal active power generator.

Starting from the AC given power output is calculated the DC input power of the inverter taking into account the given efficiency and looking at the datasheet specifications written by the inverter manufacturer (in tab. 2.3, 2.9 and 2.6).

$$P_{DC} = \frac{P_{AC}}{\eta_{inv}} \tag{3.2}$$

in which for each topology is considered the efficiency η_{inv} of the chosen inverter.

The last step for the estimation of the power dimension is to choose a suitable value for the NPR parameter, resulting in an oversizing or undersizing of the PV array. The NPR (Nominal Power Ratio) is defined by the following equation:

$$NPR = \frac{P_{DC}}{P_{DC,GEN}} \tag{3.3}$$

in which P_{DC} is the input power requested by the conversion stage and $P_{DC,GEN}$ is the output power of the PV array.
This strictly depends on the location chosen for the installation, because the irradiance and the temperature impact the voltage and current output of the solar cell. Since Spain is in a climatic zone that reaches and even exceeds the STC value of irradiance (seen in the tab. 3.1), the choice to undersize the PV array could be the correct approach to avoid unexpected overcurrents during clear-sky summer days. Thus, results in a choice of $NPR = 0.95$ (The $P_{DC,GEN}$ results as the 95 % of the requested power by the inverter).

3.2.1 Sizing of the Voltage Dimension

Now, since the power dimension is calculated, the sizing proceeds by estimating the voltage dimension considering the technical specifications given by the panel manufacturer. As specified in the related literature [7], the open-circuit voltage of the PV panel is highest at lower temperatures.

$$V_{DC,Max} = V_{OC,T_{min}} = V_{OC} \cdot \left(1 + \frac{\alpha_{V_{OC}} \cdot \Delta T}{100\%}\right) \tag{3.4}$$

The parameters considered in the eq. 3.4 are the open-circuit thermal coefficient $\alpha_{V_{OC}}$ (which specifies the voltage variation with respect to a temperature variation), T_{min} for the estimated site (tab.3.1) and a temperature variation $\Delta T = T_{min} - T_{STC}$ with respect to the Standard Test Conditions.
As might be expected, the minimum MPP voltage can be calculated as the previous one, taking the highest possible temperature and using the related thermal coefficient to estimate the updated value of V_{MPP}.

$$V_{DC,Min} = V_{MPP,T_{max}} = V_{MPP} \cdot \left(1 + \frac{\alpha_{V_{MPP}} \cdot \Delta T}{100\%}\right) \tag{3.5}$$

In which the only notable difference is the $\Delta T = T_{Max} - T_{STC}$ with T_{Max} is reported in tab. 3.1. The final estimation is related to the short circuit current, that reaches its maximum value when the temperature is high:

$$I_{DC,Max} = I_{SC,T_{max}} = I_{SC} \cdot \left(1 + \frac{\alpha_{I_{SC}} \cdot \Delta T}{100\%}\right) \tag{3.6}$$

in which $\alpha_{I_{SC}}$ is the short circuit thermal coefficient given by manufacturer.

3.3 PV Panel Equivalent Array Estimation

Now, since all the limit values of current and voltage are estimated for the worst operational conditions, is needed to calculate the number of panels per string, to define the equivalent module to insert in the simulation system. This number of modules has to ensure a minimum voltage value that is above the minimum MPPT inverter limit, to allow the system to work without any problem. If the voltage falls below the MPPT limit, yield losses can occur considering non optimal maximum power point tracking. The same reasoning is also applied for the maximum voltage allowable as a result of the upper limit of the MPPT inverter operation. The boundaries of minimum and maximum number of series connected modules are estimated as:

$$N_{Series,Min} \geq \frac{V_{MPPT,Min}}{V_{DC,Min}} \tag{3.7}$$

$$N_{Series,Max} \leq \frac{V_{MPPT,Max}}{V_{DC,Max}} \tag{3.8}$$

The selected number of series connected pv modules per string (N_{Series}) is in the middle of the range set by eq. 3.8 and 3.7, to present a value for the power output of each different topology.
The last step for the equivalent module realization is to calculate the number of strings, using the reference power output estimated in eq. 3.3.

$$N_{Parellel} = \frac{P_{DC,GEN}}{N_{Series} \cdot P_{Max,mod}} \tag{3.9}$$

3.3.1 Choice of a suitable PV Panel

The selected PV panel on the market is the RCM-610-7RCF realized by the manufacturer RECOM, presenting several key features that are suggested for a power plant several of MW.
The RCM-610-7RCF is a N-type mono crystalline half-cut PV module with the rear connection method called "Back Contact", increasing the absorption of diffused and reflected irradiance. Its general characteristics are reported in tab 3.3 below.

m-si RCM-610-7RCF	Value	Unit
P_{max}	610	W
V_{MPP}	45,41	V
I_{MPP}	13,43	A
V_{OC}	53,6	V
I_{SC}	14,03	A
η_{PV}	23,6	$\%$
$\alpha_{V_{OC}}$	-0,24	$\%/°C$
$\alpha_{I_{SC}}$	0.05	$\%/°C$
$\alpha_{V_{MPP}}$	-0,29	$\%/°C$

Table 3.3: PV panel manufacturer data

The selected module presents a I-V characteristic shown in fig. 4.2

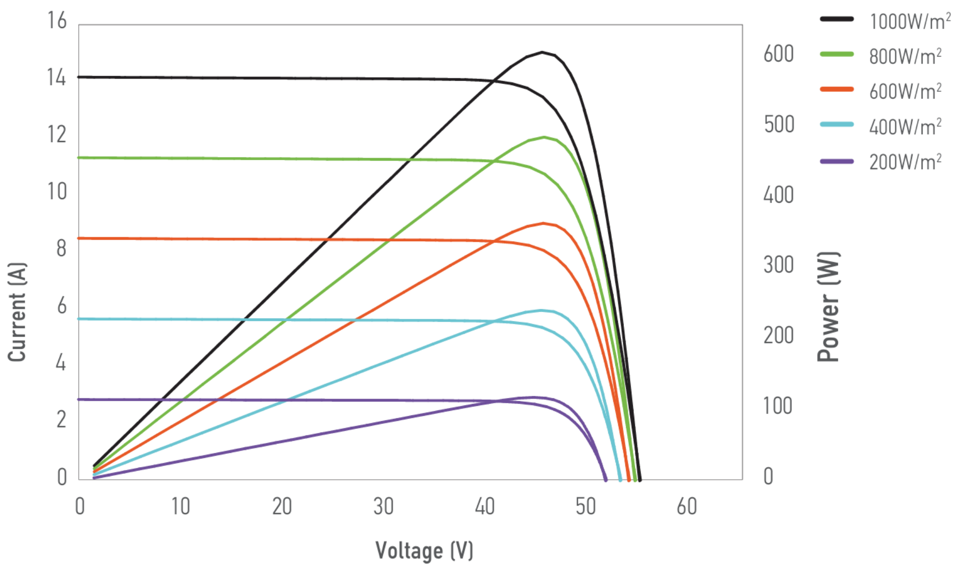

Figure 3.7: Manufacturer PV panel I-V-P Characteristics

3.3.2 Results of parameters calculation

Using the procedure described in the previous section with the data taken from the panel manufacturer in tab. 3.3 and the Inverter manufacturers in tab. 2.4, 2.7 and 2.10, in this section are calculated all useful parameters used as the starting point for the simulation.

Centralized Topology	**Value**	**Unit**	**Description**
P_{inv}	2200	kW	*inverter minimum requested power*
P_{DC}	2223,13	kW	*Max input DC power at the inverter*
NPR	0.95	-	*Nominal Power Rateo*
$P_{DC,GEN}$	2111,2	kW	*PV array requested power*
ΔT_{max}	16,56	$°C$	*temperature variation from STC*
ΔT_{min}	-24,3	$°C$	*temperature variation from STC*
V_{nom}	1200	V	*nominal input DC voltage (chosen by MPPT)*
$V_{OC_{max}}$	56,726	V	*Max PV open circuit voltage*
$V_{MPP_{min}}$	43,229	V	*Min PV voltage at Max power*
$I_{SC_{max}}$	14,146	A	*Max PV short circuit current*
$N_{S,max}$	26	-	*Max number of series connected modules*
$N_{S,min}$	22	-	*Min number of series connected modules*
N_S	25	-	*number of series connected modules*
N_P	139	-	*number of parallel connected arrays*
N_{PV}	3475	-	*total number of PV panels per inverter*
N_{inv}	126	-	*number of total inverters per topology*

Table 3.4: Centralized Plant Parameters Calculation

Multi-string Topology	**Value**	**Unit**	**Description**
P_{inv}	50	kW	*inverter minimum requested power*
P_{DC}	50,66	kW	*Max input DC power at the inverter*
NPR	0,95	-	*Nominal Power Rate*
$P_{DC,GEN}$	48,125	kW	*PV array requested power*
ΔT_{max}	16,56	$°C$	*temperature variation from STC*
ΔT_{min}	-24,3	$°C$	*temperature variation from STC*
V_{nom}	800	V	*nominal input DC voltage (chosen by MPPT)*
$N_{S,max}$	17	-	*Max number of series connected modules*
$N_{S,min}$	5	-	*Min number of series connected modules*
N_S	16	-	*number of series connected modules*
N_P	5	-	*number of parallel connected arrays*
N_{PV}	80	-	*total number of PV panels per inverter*
N_{inv}	5504	-	*number of total inverters per topology*

Table 3.5: Multi-string Plant Parameters Calculation

String Topology	**Value**	**Unit**	**Description**
P_{inv}	12,5	kW	*inverter minimum requested power*
P_{DC}	12,78	kW	*Max input DC power at the inverter*
NPR	0,95	-	*Nominal Power Rate*
$P_{DC,GEN}$	12,7	kW	*PV array requested power*
ΔT_{max}	16,56	$°C$	*temperature variation from STC*
ΔT_{min}	-24,3	$°C$	*temperature variation from STC*
V_{nom}	400	V	*nominal input DC voltage (chosen by MPPT)*
$N_{S,max}$	13	-	*Max number of series connected modules*
$N_{S,min}$	9	-	*Min number of series connected modules*
N_S	12	-	*number of series connected modules*
N_P	2	-	*number of parallel connected arrays*
N_{PV}	24	-	*total number of PV panels per inverter*
N_{inv}	22014	-	*number of total inverters per topology*

Table 3.6: String Plant Parameters Calculation

Chapter 4

Simulation Model

The study of the behavior of the considered plant, with the purpose of finding the best topology to reduce losses and cost, begins with the realization of a common generic model capable of simulating the system under different irradiance conditions. The goal of this section is to present a simulation pattern in which is possible to change the crucial parts simply, to confront different solutions and find the best one.

The proposed system consists of the following parts:

- An accurate PV-panel model, based on devices find on the market;
- A three-phase active voltage load that simulates the grid;
- A three level, 3-phase inverter with two stage conversion structure;
- A LCL filter to properly connect the conversion stage with the grid equivalent;
- A custom made thermal model based on the real device used for the related topology, to estimate losses;

4.1 PV Simulation Model

As reported in the previous chapters, it is possible to simulate the behavior of the photovoltaic panel summarizing it as a current generator controlled by temperature and solar irradiance, with a capacitor in parallel, to fix the voltage level required by the application. The visual scheme of this configuration can be seen in fig. 4.1

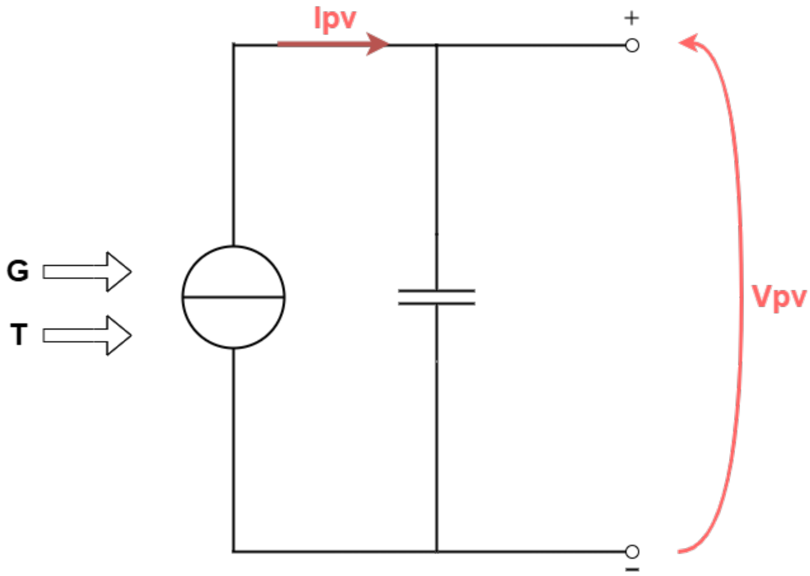

Figure 4.1: PV generator Model

The dependence of the panel on solar irradiance is one of the crucial points to perform an accurate analysis of the PV generation under a daily sun cycle, because the power injected into the grid is widely affected by the changing of these parameters.
The adopted solution in PLECS workspace is a 2D Look-Up Table model (LUT), realized starting from the datasheets of the chosen components.
This LUT schematic is able to parameterize the I-V characteristic for a given value of irradiance (G) and temperature (T), presenting a specific photo-generated current value at its terminals.

4.1.1 Look-Up Table of PV generator

The starting point for LUT creation is the I-V characteristic of the selected component datasheet, summarized in tab. 3.3

Looking at the I-V diagrams in fig. 4.2, the most important points to know

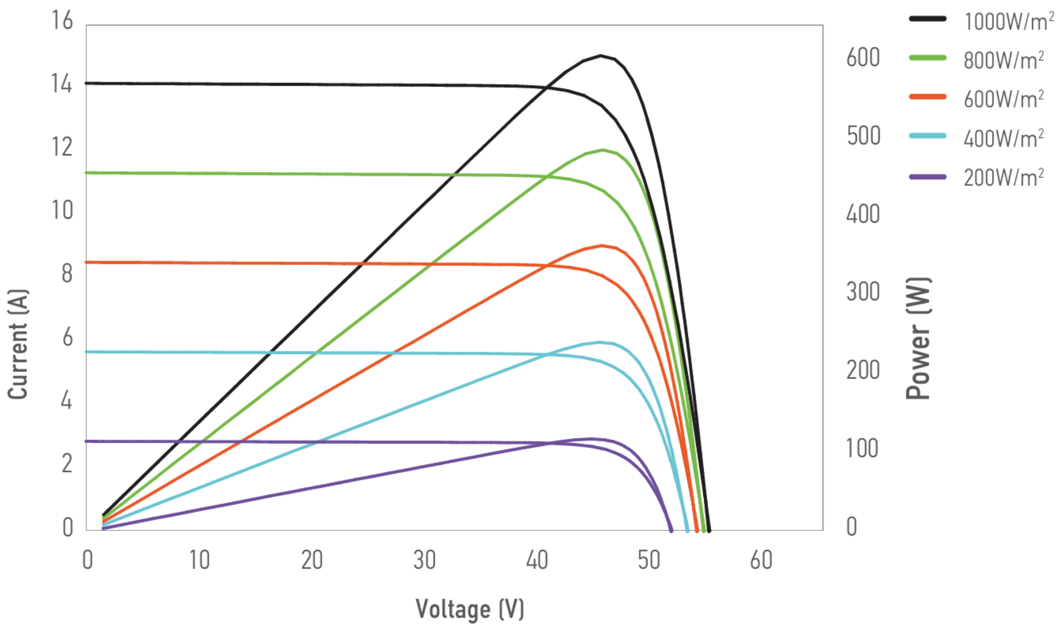

Figure 4.2: manufacturer PV panel I-V-P Characteristics

are the open circuit voltage (Voc), the short circuit current (Isc), MPP [1] current and voltage. The mathematical procedure adopted to extrapolate parameterization starts from the Standard Test Condition (STC) values of these parameters (with a fixed irradiance $G = 1000W/m^2$ and a fixed temperature $T = 25$ °C).
As widely discussed in [7], the variation of irradiance and temperature drastically changes the behavior of the solar cell:

- With a change in sun irradiance, the most affected parameter is the current (I_{SC} and I_{mpp}), which can decrease more than half of its expected value under ST conditions. For the voltage, the variation can be negligible.
- With a temperature variation, the voltage is the parameter most affected (V_{OC} and V_{mpp}). In general, a variation of G and T below the STC values decreases the overall performance of the entire PV system.

For the proposed model, the challenge is to realize a mathematical approximation of the real behavior of the solar cell, to adapt the PV voltage and current used to extract the losses from the plant and, as a direct consequence, the choice the correct topology for the application.
Following this path, it is necessary to define some mathematical relation between

[1]Maximum Power Point

the parameters of interest, as widely defined in the article [10].

The photogenerated current can be expressed as:

$$I = I_{SC} \cdot \left[1 - C1 \cdot exp\left(\frac{V}{C2 \cdot V_{OC}}\right)\right] \tag{4.1}$$

where $C1$ and $C2$ are two coefficients used as fitting factors for the two graphs (two analytic parameters necessary to follow the envelope of the I-V graph), calculated as:

$$C1 = \left(1 - \frac{I_{mpp}}{I_{SC}}\right) \cdot exp\left(\frac{-V_{mpp}}{C2 \cdot V_{OC}}\right) = \frac{I_{sc}}{1 - exp\left(\frac{-V_{OC}}{C2}\right)} \tag{4.2}$$

$$C2 = \frac{V_{mpp} - V_{OC}}{Ln\left(1 - \frac{I_{mpp}}{I_{SC}}\right)} \tag{4.3}$$

These two fitting factors are computed using STC values and the results are placed into eq. 4.1 to obtain the I-V curve profile. Now, it is necessary to update all parameters under different irradiance and temperature conditions, to change the shape of the characteristic ([7] and [10]).
The current update is performed as:

$$I_{SC} = I_{SC_{STC}} + \Delta I \tag{4.4}$$

where ΔI is computed as:

$$\Delta I = I_{SC_{STC}} \cdot \left(\frac{G}{G_{STC}} - 1\right) + \mu_{I_{SC}} \cdot \frac{G}{G_{STC}} \cdot \Delta T \tag{4.5}$$

where G is the received irradiance with respect to the STC one, ΔT is the temperature variation between the STC value and real one and $\mu_{I_{SC}}$ is the thermal variation coefficient of the short circuit current extracted from the manufacturer datasheet described in tab.3.3.
It is necessary to modify also the open circuit voltage value, with a similar configuration as the one nearly discussed:

$$V_{OC} = V_{OC_{STC}} + \Delta V \tag{4.6}$$

In this case, ΔV has the following equation

$$\Delta V = \mu_{V_{OC}} \cdot \Delta T - R_S \cdot \Delta I \tag{4.7}$$

in which is considered the thermal coefficient of the open circuit voltage, $\mu_{V_{OC}}$, given by the panel manufacturer as before, and the internal series resistance of the panel ($R_S = 10\, m\Omega$).
For the simulation model, these formulas are translated into code in a MatLab script, obtaining the plot in fig. 4.3

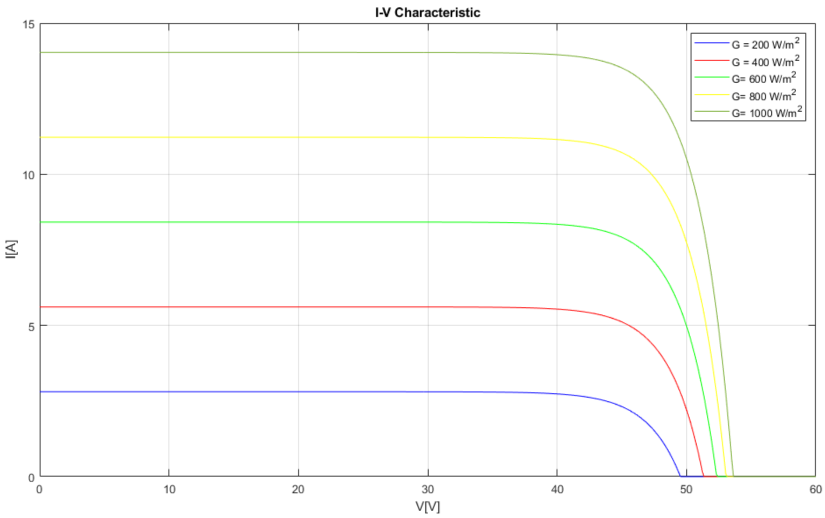

Figure 4.3: Approximated Matlab I-V Characteristics (G variation)

The calculated values are saved and stored inside a matrix that is directly reported to the PLECS workspace inside the PV Module subsystem. The Matlab code used to fill the matrix is reported in Appendix C.

4.1.2 PLECS PV-module implementation

As discussed in the previous subsection, the photovoltaic system can be summarized as a current generator controlled by an input of irradiance (or temperature) with a capacitor in parallel at a fixed voltage level. The proposed schematic is presented in fig. 4.4

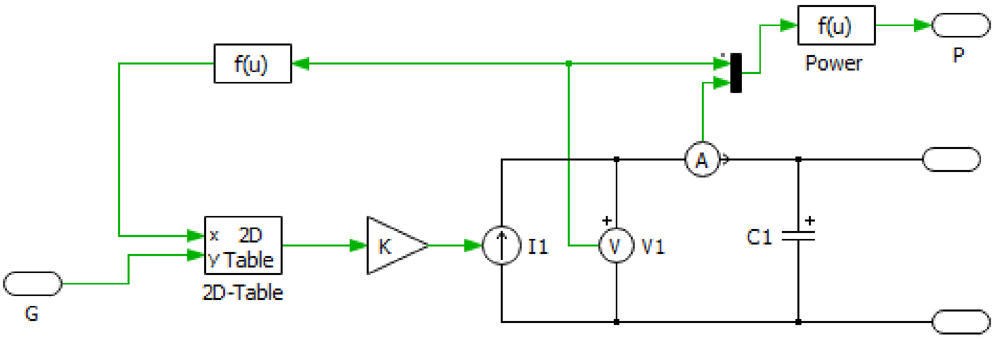

Figure 4.4: PV Panel PLECS sub-model

The reported mask has been updated with values coming from tab. 3.4, 3.5, 3.6 and the active power produced is calculated by the PV, to extrapolate the overall efficiency and calculate thermal losses in the different parts of the structure.

PV Panel Mask Input Values	Centralized	Multi-string	String
N_{Series}	25	16	12
$N_{Parallel}$	139	5	2
V_{init} [V]	1200	800	600
C_{PV} [F]	$1 \cdot 10^{-6}$	$1 \cdot 10^{-6}$	$1 \cdot 10^{-6}$

4.2 LCL filter

To connect the converter to the grid, sizing a proper filter is mandatory for two reasons: An inductive filter is always needed to face a voltage source inverter with respect to a voltage source active load (that is the adopted model to simulate the grid behavior); more importantly, the filter is necessary to cancel the majority of harmonics created by the opening and closing of the converter's transistors, which could create disturbances in the output power signal. In fact, if the 3-phase voltage is full of unwanted harmonics, the resulting power transfer will be affected, causing the occurrence of unpredictable and even dangerous events.

For a solar application with power around megawatts, the topology of filter selected in the majority of systems is LCL, which has a structure shown in fig.4.5.

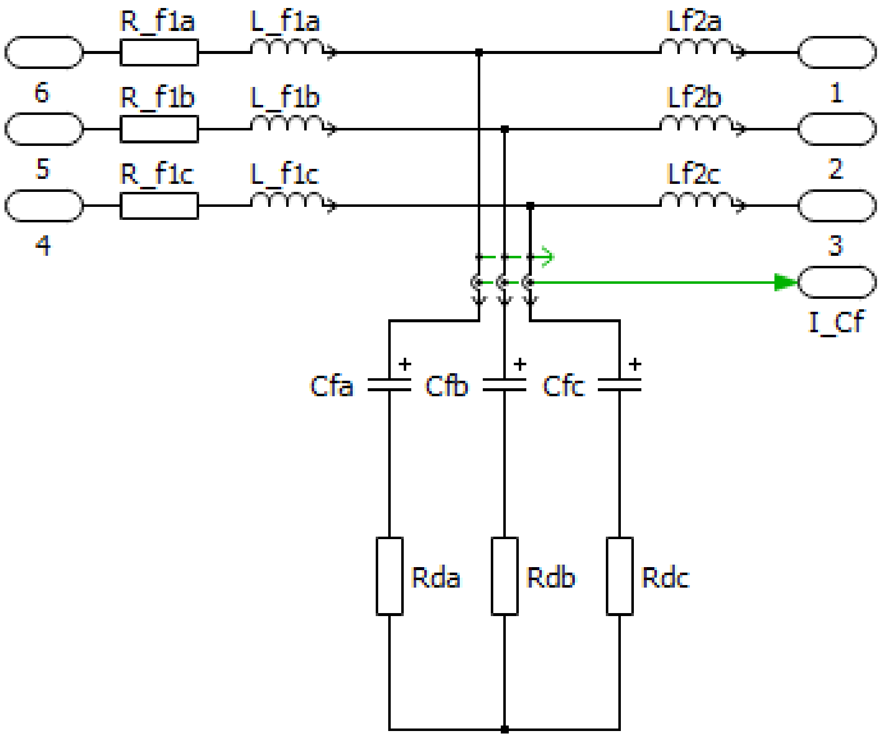

Figure 4.5: LCL filter circuit scheme

in which L_{f1} is the converter side inductor, L_{f2} is the grid side inductor, C_f the filtering capacitor, R_f is the filter resistance and R_d is the damping resistance. The sizing of the filter parameters is performed considering the relation between the base capacitance and inductance of the system considered on the basis of practical experience, following the equations:

$$L_{f1} = 0.06 \cdot L_b \tag{4.8}$$

$$L_{f2} = 0.03 \cdot L_b \tag{4.9}$$

$$C_f = 0.04 \cdot C_b \tag{4.10}$$

$$R_d = 0.1 \cdot Z_b \tag{4.11}$$

where L_b, C_b and Z_b are the base inductance, capacitance and impedence of the system, calculated as:

$$Z_b = \frac{V_b}{I_b} \tag{4.12}$$

$$L_b = \frac{Z_b}{2\pi \cdot f_b} \tag{4.13}$$

$$C_b = \frac{1}{2\pi \cdot f_b \cdot Z_b} \tag{4.14}$$

All the values obtained are reported in the tab. 4.1.

Parameter	**Centralized**	**Multi-string**	**String**	**Unit**
L_f1	12.124	606.19	2425	μH
L_f2	6.062	303.09	1212	μH
Cf	2	0.0401	0.01003	mF
R_d	0.063	0.317	1.26	Ω

Table 4.1: LCL filter parameters

4.3 DC/AC Converter Model

The central core of the model is represented by the DC/AC converter structure, that is carried out by a careful study of the literature, both from a control and power electronics point of view. The aim of this project is not to present a perfectly tuned control system of a three-phase grid connected inverter, but to use it as a starting point to perform a feasibility analysis in order to compare the most suitable solution to the preliminary topology choice for a large-scale PV Plant.
Using the proposed scheme as reference to size a proper converter and detect losses propagation between its parts, permit to simulate different loads and generation conditions to follow the power profile described in the previous section.

4.3.1 Converter model adopted

Following the state-of-the-art for solar generation, the converter scheme adopted is a two-stage cascade conversion:

- Three-level bidirectional three-phase inverter connected to the grid (simulated as a three-phase active load)
- DC/DC boost converter stage to increase the voltage of the panel at the requested DC-link value.

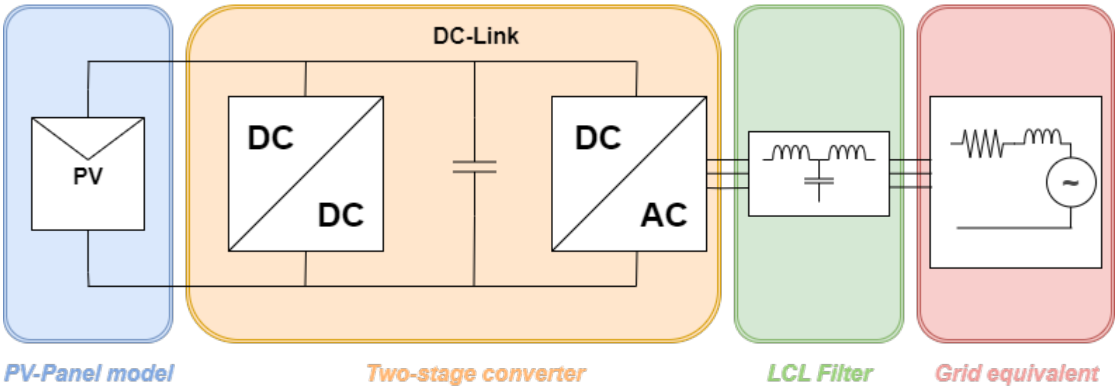

Figure 4.6: System block representation

The connection between the grid equivalent and the two-stage converter is performed by adding an LCL filter to properly smooth the output waveforms of current and voltage.

A proper control is needed to exploit the two stage conversion system, in order to obtain the maximum output of active power from the PV panels. In fact, the DC/DC converter is controlled as a current generator imposing a fixed voltage value on the DC-Link, using a particular algorithm called MPPT (Maximum Power Point Tracking).
The MPPT finds the best working point of the system, based on the irradiance and temperature conditions in which the plant works, giving a specific $V_{PV} = V_{MPP}$ value; the DC/DC boost converter regulates the output on the DC-Link, following the specific V_{MPP} calculated by the algorithm. The inverter (DC/AC converter) regulates the injection of active power (o reactive for grid operations) based on the voltage over the DC-Link capacitor.
The LCL filter is necessary to ensure high quality waveforms entering the grid, avoid the presence of unwanted harmonics that create distortion and, as a direct consequence, losses of all the fungible active power.

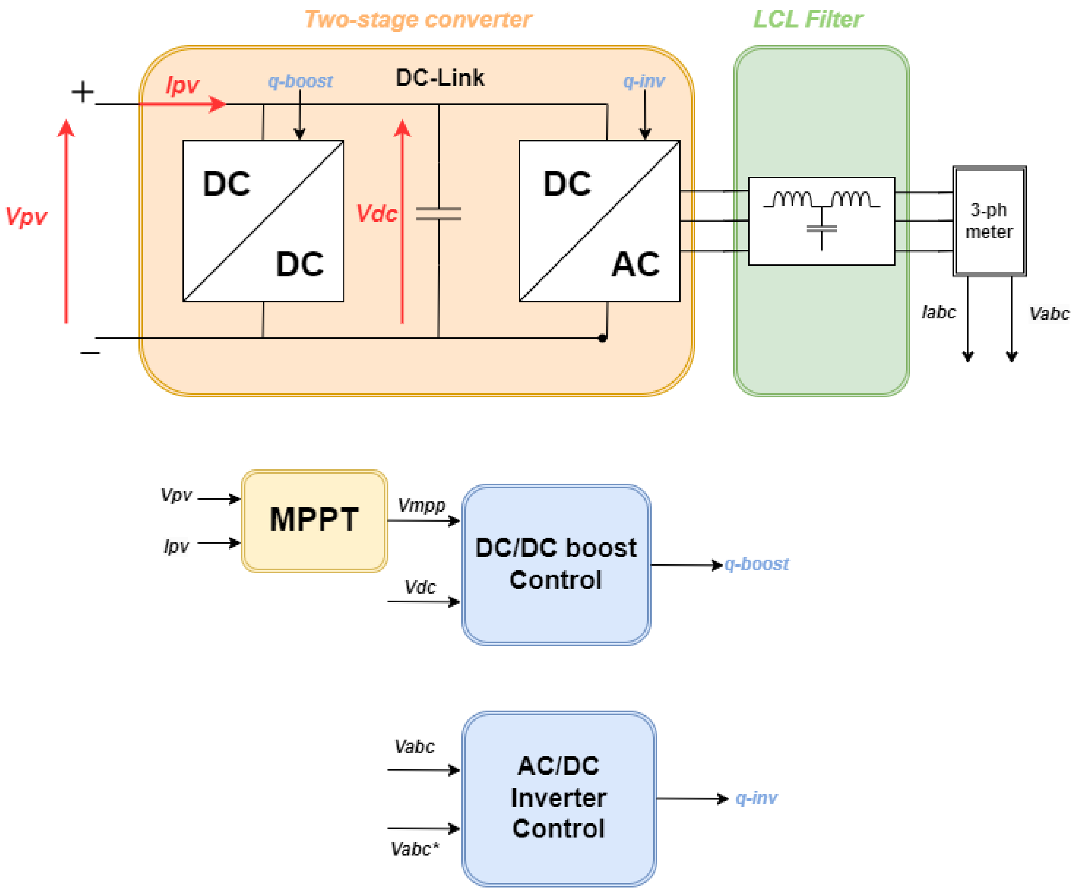

Figure 4.7: Control scheme block representation

in fig. 4.7 is reported a simplified block schematic of the two-stage conversion control, in which the boost and the inverter switching functions are obtained as result of a closed-loop control. The grid equivalent and the photovoltaic model have been omitted to better understand all the parts that take place during the power transformation.

4.3.2 Detailed control model of the inverter

The starting point for the realization of the two-stage conversion, is to size a proper inverter control capable to adapt the output of the desired variables responding to a variation of the input quantities with an acceptable dynamic. Following the appropriate technical literature, the straightforward solution is a cascaded control, in which the inner loop is focused on the current and the outer loop focused on the voltage.
It is important to note that, for a grid-related application, the measured voltages and currents have to be synchronized with the grid phase using a PLL [2] unit. The current control loop is realized directly on the rotating axis *dq*, in which electrical quantities are reported in a reference system that is synchronous with the grid.

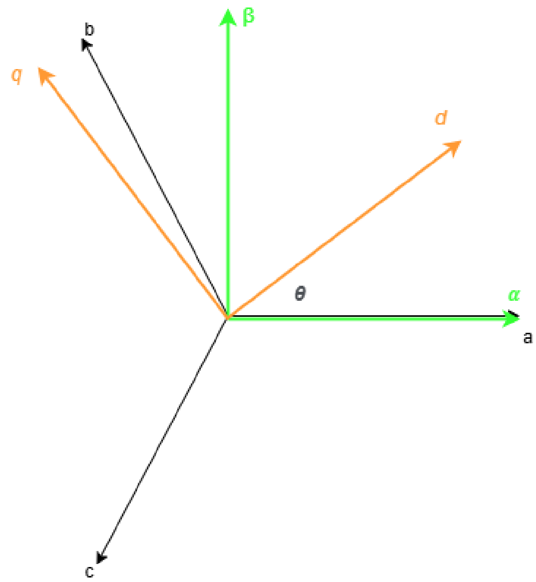

Figure 4.8: Vectorial diagram positions 3-phase, 2-phase stationary and 2-phase rotating equivalent

For the application under analysis, the choice of this specific configuration is preferred for several reasons: first of all, if sinusoidal measures are reported into a PI controller[3], it is possible that the PI is not able to annul the error in steady state, presenting a slow dynamic; second, the computation burden of the simulation is considerably reduced, due to the fact that there is a transformation of the status

[2]Phase locked loop Unit

[3]Proportional Integral controller, most adopted solution for signal comparison

variables from a three-phase world to a two-phase rotating system. In fig.4.8 the is depicted the vectorial scheme of the situation.

The current control is oriented with the d-axis, with the purpose of changing the injected or absorbed active power towards the grid. It is also possible to vary the reactive power with the reference of the q-axis, allowing power flow control operation.

Grid synchronization by PLL *dq*-oriented

The Phase Locked-loop is a specific algorithm used with the purpose to calculate the grid voltage phase angle, to permit a perfect synchronization between the control signal and the grid. An estimation error of this angle could lead to an error in the generated output voltage, which is used for converter control.
Different solutions for the PLL strategy are described in related theory, but the common point is the reconstruction of the fundamental component of the grid voltage which is used for the control loops. The mathematical description of the phenomena starts with a definition of a generic 3-phase voltage system:

$$V_{abc} = \begin{bmatrix} \hat{V} \cdot sin\left(\omega \cdot t\right) \\ \hat{V} \cdot sin\left(\omega \cdot t + \frac{2\pi}{3}\right) \\ \hat{V} \cdot sin\left(\omega \cdot t - \frac{2\pi}{3}\right) \end{bmatrix} \tag{4.15}$$

where $\omega = 2\pi \cdot f_g$ is the fundamental electric pulsation and $\hat{V}$ is the amplitude of the fundamental voltage.
Since this system is considered ideal and the 3-phase quantities are represented as in fig. 4.8, it is possible to apply the Clarke transformation, described in Appendix A which does not variate the amplitude reference, obtaining:

$$V_{\alpha\beta 0} = \begin{bmatrix} \hat{V} \cdot sin\left(\omega \cdot t\right) \\ \hat{V} \cdot cos\left(\omega \cdot t\right) \\ 0 \end{bmatrix} = \begin{bmatrix} V_\alpha \\ V_\beta \\ V_0 \end{bmatrix} \tag{4.16}$$

Due to the nature of the 3-phase connection, the omopolar component can be neglected translating the system into a two-phase equivalent:

$$V_{\alpha\beta} = \begin{bmatrix} V_\alpha \\ V_\beta \end{bmatrix} = \begin{bmatrix} \hat{V} \cdot sin\left(\omega \cdot t\right) \\ \hat{V} \cdot cos\left(\omega \cdot t\right) \end{bmatrix} \tag{4.17}$$

Now, the following step is to apply the rotation to reference system by an angle $\hat{\theta}$, using the rotation transformation R($\hat{\theta}$) (Appendix A), obtaining:

$$V_{dq} = \begin{bmatrix} V_d \\ V_q \end{bmatrix} = \begin{bmatrix} \hat{V} \cdot sin\left(\theta - \hat{\theta}\right) \\ \hat{V} \cdot cos\left(\theta - \hat{\theta}\right) \end{bmatrix} \tag{4.18}$$

where $\theta = \omega \cdot t$. Since in steady state the difference between θ and $\hat{\theta}$ is ideally zero, due to the proprieties of the sinusoidal trigonometric functions, it can be approximated to:

$$V_{dq} = \begin{bmatrix} V_d \\ V_q \end{bmatrix} = \begin{bmatrix} \hat{V} \cdot 1 \\ \hat{V} \cdot \left(\theta - \hat{\theta}\right) \end{bmatrix} \tag{4.19}$$

The physical interpretation of the previous equations shows that closer the difference $\theta - \hat{\theta}$ is to zero, more V_d is equal to the amplitude of the desired output voltage and V_q is equal to the phase error. The algorithm exploits this concept, using the error signal V_q for a position control loop.
The PLL shown in fig. 4.9 is realized by presenting this error signal in front of a PI controller, which has its output equal to the electric pulsation ω_{PLL}, that is integrated to obtain the angle θ_{PLL} (in phase with the grid).

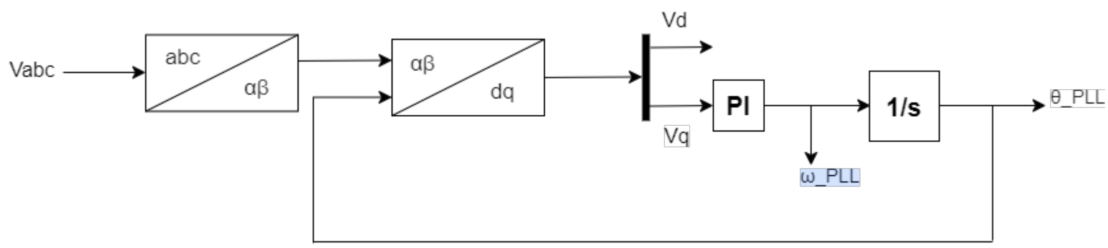

Figure 4.9: PLL block schematic

In steady state, θ_{PLL} follows the $\hat{\theta}$ with a dynamic that depends by PI settings showed in Appendix B and the average ω_{PLL} will be equal to ω of the fundamental component of the voltage.

Current control loop

According to power theory, the active/reactive power balance is related to the currents in the dq- axis in the following way:

$$\begin{bmatrix} P \\ Q \end{bmatrix} = \frac{3}{2} \cdot \begin{bmatrix} V_d & V_q \\ -V_q & V_d \end{bmatrix} \cdot \begin{bmatrix} i_d \\ i_q \end{bmatrix} \tag{4.20}$$

Where P is the active power and Q the reactive one. As previously discussed in the PLL section, all the information to reconstruct the grid voltage are only on the d-axis: due to this important concept, the voltage on the q-axis can be considered equal to zero, simplifying the relation expressed in eq. 4.20 as following:

$$P = \frac{3}{2} \cdot V_d \cdot i_d \tag{4.21}$$

$$Q = \frac{3}{2} \cdot V_d \cdot i_q \tag{4.22}$$

all active power depends by the quantities on the d-axis, while the reactive power is related to the quantities on the q-axis, leaving the possibility to control the proper current according to the desired type of operation (power injection or frequency regulation).

The adopted scheme for the inverter control is shown in fig. 4.10, in which the inner current loop and the outer voltage loop are connected. In the DC-Link voltage loop the reference DC-Link voltage value and the measured one are compared to estimate the voltage error, useful to find the reference value for the current on the d-axis.
As in the voltage loop, the current loop exploits error estimation between current measured values and reference ones to compute the duty cycle of the converter.
The duty, newly calculated, is presented in the modulation block with the purpose of computing the switching leg signals.

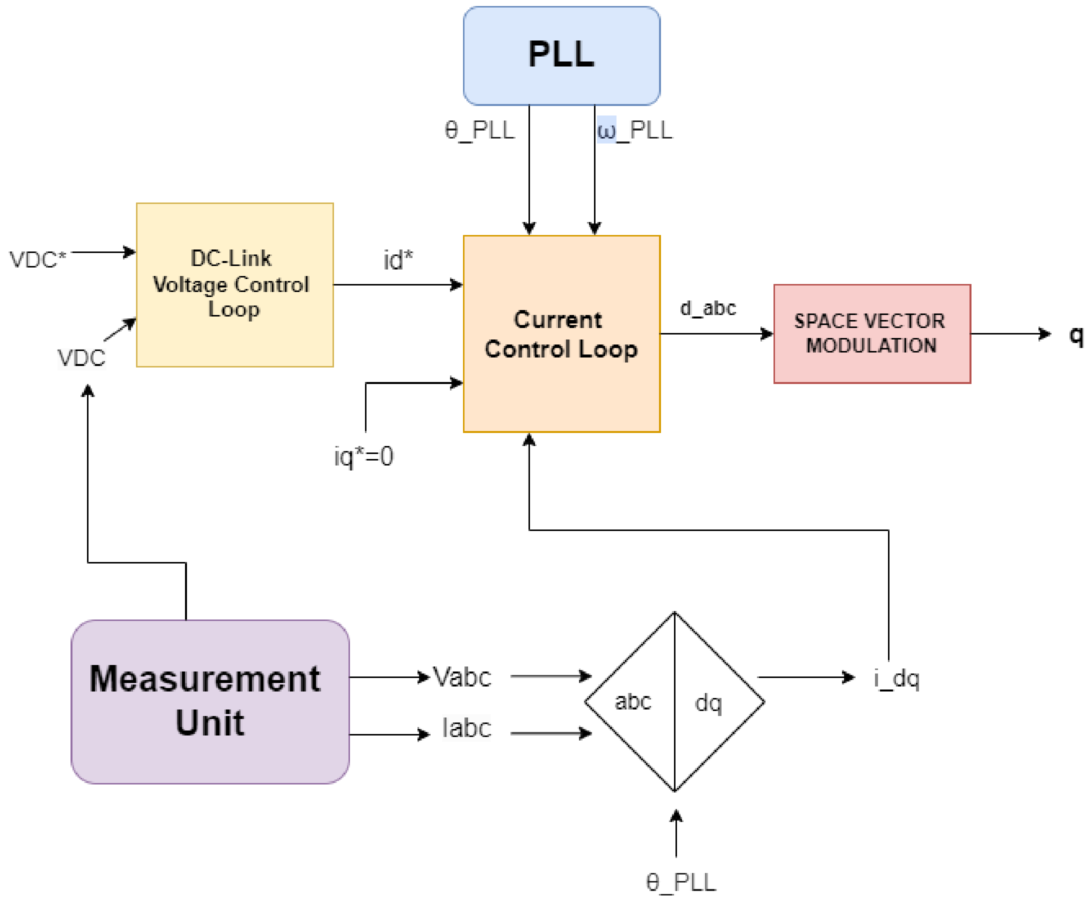

Figure 4.10: Inverter Control Scheme, PLL-Current Loop-Voltage Loop

Since the control is based on the *dq*-frame each measured value has to be transformed on the respective axis, necessitating to know the angle θ_{PLL} derived by the PLL unit for the direct and opposite rotational transform.

The single blocks represented in fig. 4.10 will be described below in detail, explaining also the PLECS implementation, with a dedicated section for the PI tuning in each step of the control.

- **Inner current control loop**
  For the first part of the current control loop description, in fig.4.11 is represented how the reference voltage is calculated, starting from the current error entering in the PI and adding the measured voltage and the motional term (dependent by the opposite axis's current).

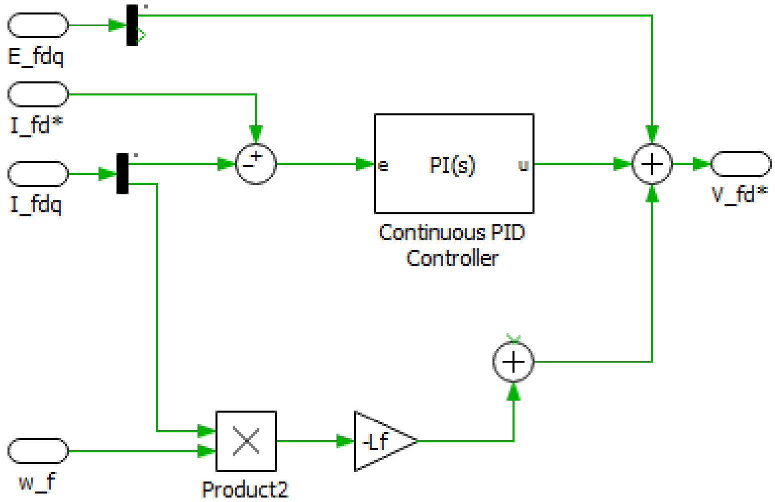

Figure 4.11: d-axis inner current control loop

The same structure of the control is exploited also for the q-axis and is presented in fig. 4.12, presenting as relevant difference the reference value of the current $i_q = 0$, due to the previous considerations made in the PLL section.

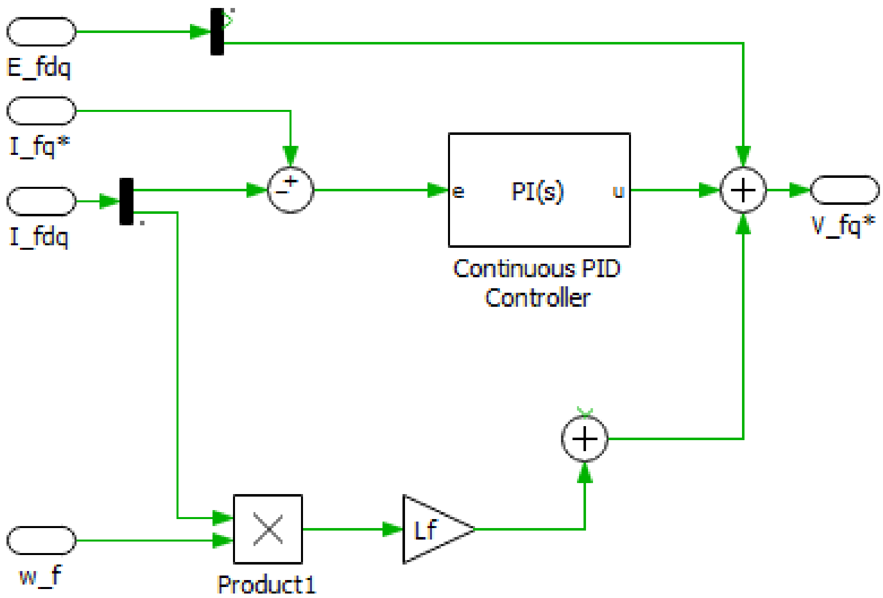

Figure 4.12: Q-axis inner current control loop

- **Outer voltage control loop**

To properly control the DC-Link voltage a current reference on the d-axis, a outer voltage loop is needed, that takes as reference the difference between the desired DC-link value and the measured one. The output of this section became the input of the current loop one.

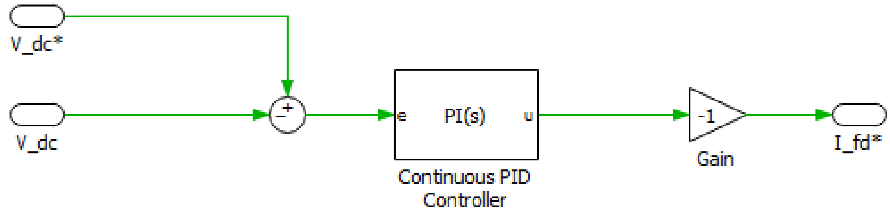

Figure 4.13: External voltage control loop

It is important to underline that, since the proposed control is realized as a cascade, the inner and the outer parts do not have to interfere between each other, taking for the tuning the proper bandwidth with at least a decade of difference for the frequency.

PI Tuning

The central core of the inverter closed-loop control is the section dedicated to the PI tuning. For both current and voltage loops, the transfer function in the Laplace domain is calculated and the resulting scheme are presented in the Appendix B. Looking at the current one, the chosen bandwidth is strictly related to the switching frequency of the converter, with the following equation:

$$\omega_{bw,i} = \frac{2}{3} \cdot f_{sw} \tag{4.23}$$

that has the equivalent frequency as:

$$f_{bw,i} = \frac{\omega_{bw,i}}{2 \cdot \pi} \simeq \frac{f_{sw}}{10} \tag{4.24}$$

Therefore, as the practical experience suggests, there is a factor of 10 between the two frequencies, to avoid a reciprocal disturbance.

To calculate the proportional and integral coefficients, the following relations are exploited:

$$k_{p,i} = \omega_{bw,i} \cdot (L_{f_1}) \tag{4.25}$$

$$k_{i,i} = \frac{\omega_{bw,i}}{10} \cdot k_{p,i} \tag{4.26}$$

in which L_{f1} represents the filter inductance from the converter side (the entire stage is considered purely inductive, since the voltage is constant).
For the voltage loop tuning, the procedure adopted is the same but starting from a lower frequency (in this case 50 times), to avoid disturbances between the two cascaded parts and to permit a decoupling of the tuning of the two parts.

$$\omega_{bw,v} = \frac{\omega_{bw,i}}{50} \tag{4.27}$$

the proportional gain, for the voltage regulation, depends by the input capacitance on the DC-Link, following the relation:

$$k_{p_v} = \omega_{bw,v} \cdot C_{DC} \tag{4.28}$$

The integral gain can be calculated as before:

$$k_{i,v} = \frac{\omega_{bw,w}}{10} \cdot k_{p_v} \tag{4.29}$$

Following the relations expressed in eq. 4.29, 4.28, 4.26 and 4.25, the proportional and integral coefficients are calculated and shown in the tab.4.2

Parameter	Centralized	Multi-string	String	Unit
$f_{bw,i}$	530.52	530.52	530.52	Hz
$f_{bw,v}$	10.62	10.62	10.62	Hz
$\omega_{bw,i}$	3333.4	3333.4	3333.4	rad/s
$\omega_{bw,v}$	66.67	66.67	66.67	rad/s
$k_{p,i}$	0.0404	2.0206	8.0825	Ω
$k_{i,i}$	13.471	673.54	2694.2	$\Omega\cdot\ rad/s$
$k_{p,v}$	3.6841	0.1658	0.0736	S
$k_{i,v}$	24.561	1.1052	0.4912	$S\cdot rad/s$

Table 4.2: Inverter Current and Voltage loops set-up

All these values are calculated directly in the PLECS model and placed inside the PI blocks in their respective parts.
A three-level inverter schematic used for PLECS simulation is reported in fig 4.14, in which the control signals of the transistor are shown with green arrows.

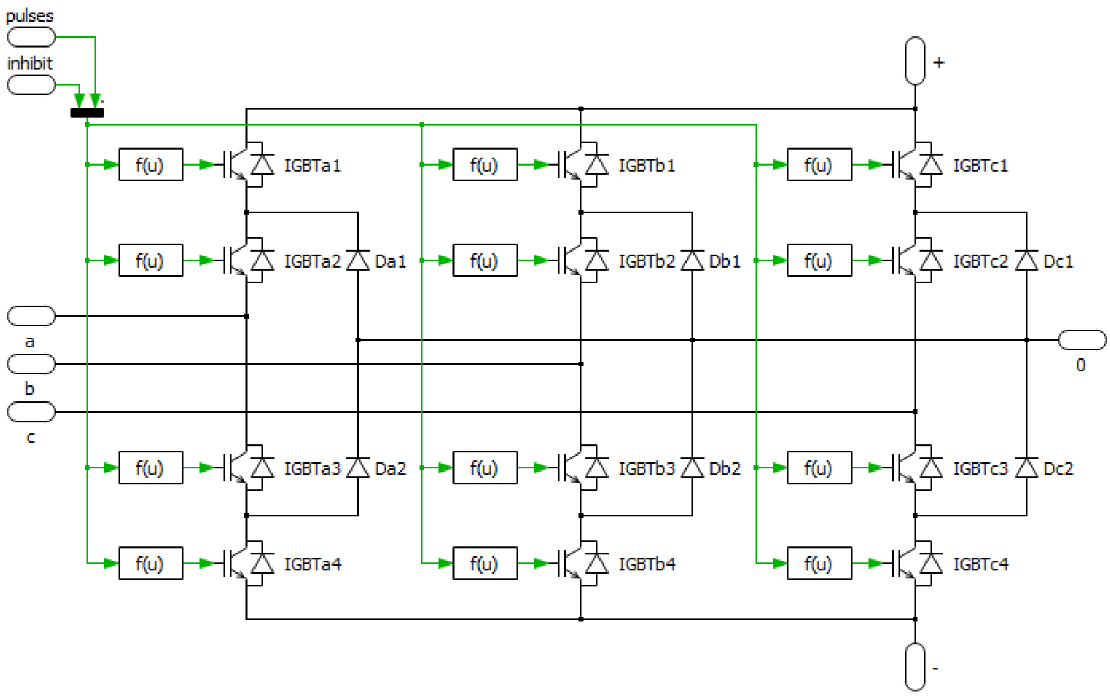

Figure 4.14: Three-level inverter schematic

Inverter's Modulation techniques

The literature([11]) suggests several types of modulation, each of which presents different advantages and disadvantages depending on the selected application.

- **Sinusoidal Pulse Width Modulation**
  Sinusoidal Pulse Width Modulation (SPWM) is one of the simplest modulation techniques. It works by comparing a three-phase balanced sinusoidal waveform (reference) with a high-frequency carrier signal (modulator).
  The outcome of this comparison is used to control the gate drivers of the inverter and consists in a square-wave signal that has as 1 as amplitude when the reference exceeds the carrier and 0 otherwise.
  Increasing the carrier frequency helps reduce the total harmonic distortion in the output voltage, but it also causes higher switching losses, increasing the quality of the output but with an increase of thermal losses.
  The primary advantage of SPWM lies in its straightforward implementation and low computational complexity, as it requires only a single multiplication per phase.

- **Third Harmonic Injection**
  This technique takes advantage of the natural rejection of third harmonics in three-phase systems to achieve a 15% higher output voltage without entering in the overmodulation zone[4].
  In a three-phase systems, third harmonic components are in phase across all three output voltages, which means they do not contribute to the line-to-line voltages.
  By leveraging this characteristic, a reference signal is used where the fundamental component exceeds the carrier signal's peak, while a third-harmonic component is added in such a way that the combined reference signal remains below the carrier peak. As a result, only the fundamental component impacts the load, while the third harmonic is inherently canceled out.

[4]The overmodulation is reached when the duty-cycle of the converter saturates starting to become a trapezoidal waveform, leading to a losses in the output quality and more power dissipation

- **Space Vector Modulation**
  The Space Vector Modulation (SVM) is the most used technique for voltage source inverter, since has a digital-only implementation and is not based on a carrier comparison like the previous one. It has the same advantages of the third-harmonic injection increasing the output range by 15%, but changing the overmodulation zone (even if, for the application under analysis, the overmodulation zone is not reached in normal operation conditions).
  Despite of it common use, the computational burden of the simulation is increased id SVM is employed because several mathematic calculation are required to detect the right position of the voltage vector in space (but is simpler to implement in PLECS workspace).

- **Discontinuous PWM**
  This last paragraph includes all the different discontinuous techniques that have in common a peculiarity of the duty-cycle: it is not a always a continuous waveform, but is clamped in specific points at 1 or 0 (that could also reduce the switching losses of the transistors involved).
  The linear zone is extended also in this case, but each technique has a specific target application. The Min-Max discontinuous PWM are usually the most employed ones.

The chosen topology of modulation adopted for the proposed model is the SVM, which improves the performance and has a dedicated library in PLCES workspace.

4.3.3 DC/DC Stage Converter Scheme

The two stage converter model adopted, as previously discussed, needs a DC/DC conversion stage on the DC-Link to have a specific input voltage on the inverter side, allowing to reduce the overall cost of the application and, more importantly, the implementation of MPPT[5] algorithm.

[5]Maximum Power Point Tracker, mandatory in solar generation application

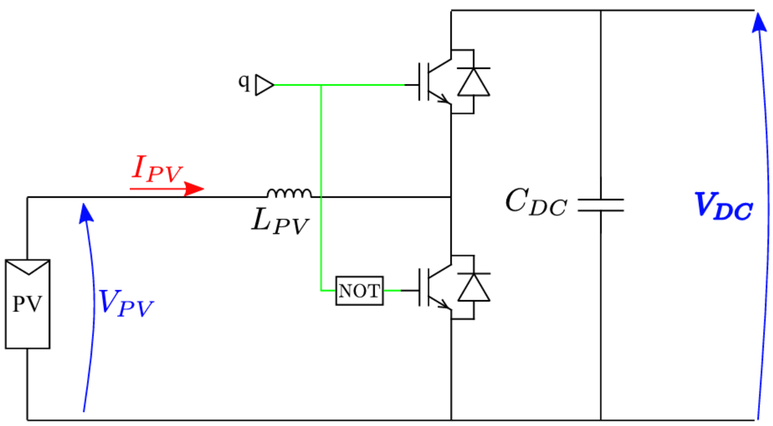

Figure 4.15: DC/DC boost structure

In this specific application the DC/DC converter, represented as a boost converter shown in fig 4.15, is controlled to apply on the DC-link the value of voltage that maximizes the active power extraction from the PV modules.

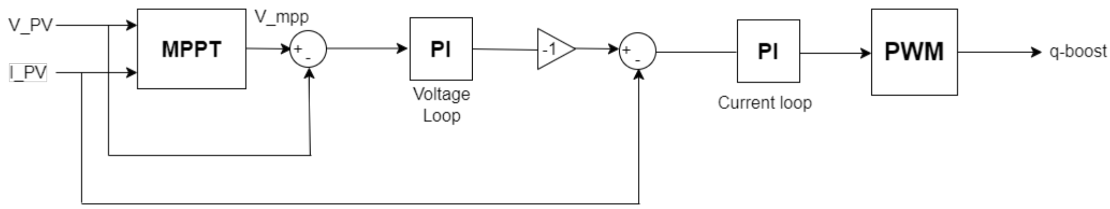

Figure 4.16: DC/DC control schematic with MPPT algorithm

The input inductance is selected as a function of the related DC voltage output of the PV generator, the switching frequency of the converter and the maximum current ripple in the worst case scenario (duty cycle equal to 0.5).

$$L_{DC} = \frac{V_{DC} \cdot 0.5^2}{f_{sw} \cdot \Delta i_L} \tag{4.30}$$

The boost converter is controlled with a cascaded inner current loop with an outer voltage loop, as the AC/AC conversion stage, with the purpose of setting a specific voltage on the DC side, using as reference value the MPPT calculated voltage.

PI current and voltage tuning

The chosen bandwidth for the boost converter is strongly dependent by the switching frequency. As the previous case for the DC/AC conversion with the inverter the $f_{bw_{boost,i}}$ chosen is:

$$f_{bw_{boost,i}} = \frac{f_{sw_{boost}}}{10} \tag{4.31}$$

to avoid any kind of disturbances that could occur if the two frequencies does not respect the relation expressed in 4.31.

For the current loop the proportional and integral gains are calculated as:

$$kp_{i_{boost}} = \omega_{bw,boost} \cdot L_{DC} = f_{bw,boost} \cdot 2\pi \cdot L_{DC} \tag{4.32}$$

$$ki_{i_{boost}} = \frac{\omega_{bw,boost}}{10} \cdot kp_{i_{boost}} \tag{4.33}$$

Also, for the outer voltage loop, chosen a proper frequency at least a decade lower as for the inverter control (4.34), the proportional and integral gains are expressed as:

$$f_{bw_{boost,v}} = \frac{f_{bw_{boost,i}}}{50} \tag{4.34}$$

$$kp_{v_{boost}} = \omega_{bw_{boost,v}} \cdot C_{PV} \tag{4.35}$$

$$ki_{v_{boost}} = \frac{\omega_{bw_{boost,v}}}{10} \cdot kp_{v_{boost}} \tag{4.36}$$

Where C_{PV} is the equivalent capacitance of the PV generator (used for the equivalent PV model). The results of the PI Tuning for the DC/DC converter are summarized in tab 4.3.

Parameter	**Centralized**	**Multi-string**	**String**	**Unit**
$f_{bw,i}$	3000	3000	3000	Hz
$f_{bw,v}$	300	300	300	Hz
$\omega_{bw,i}$	18849	18849	18849	rad/s
$\omega_{bw,v}$	1885	1885	1885	rad/s
$k_{p,i}$	10.857	241.27	542.87	Ω
$k_{i,i}$	20465	454791	1023280	$\Omega \cdot rad/s$
$k_{p,v}$	0.0188	0.01885	0.01885	S
$k_{i,v}$	71.06	71.061	71.06	$S \cdot rad/s$

Table 4.3: Current and Voltage loops set-up boost converter

4.4 MPPT algorithm

The MPPT technique is a mandatory part of solar generation, useful to extract the maximum power from the photovoltaic panel and improve the quality of the system.
For this kind of algorithm, there are several different implementations, each of which presents advantages and disadvantages, depending on the chosen application. The MPPT is employed not only on the solar generation sector, but also in other different areas, such as wind generation, with the same purpose of extracting the maximum power from the source.

Looking at the available literature [7] used for the realization of this project, the most used techniques for the MPPT regulation are:

- *Constant Voltage Reference*: is the simplest method, and is realized by the selection of a constant voltage value, that does not change during the simulation.
  The MPP voltage value, that is the target of the MPPT algorithm, can be estimated directly if the panel specifications are known. Ideally, it is possible to create an algorithm that is able to calculate the MPP value of a chosen panel and impose it on the input of the boost converter voltage regulation loop. Obviously, this works only for a given PV panel and if the panel is changed, a new algorithm is requested to perform the MPPT.
  The Constant Voltage Reference algorithm usually estimates the MPP voltage as the 80% of the panel open circuit voltage, which is given on the datasheet directly from the manufacturer.
  This strategy has the advantage of simplicity and low computational burden, but needs to know the technical specification o the panel before starting.

$$V_{MPP} \approx 0.8 \cdot V_{OC} \tag{4.37}$$

- *Perturb & Observe (P & 0)*: is the most employed solution and it consists of an iterative algorithm, in which in every iteration the output voltage and current of the panel are measured, to calculate the respective point in I-V characteristic. After the point estimation, the strategy perturbs the output voltage and compute again the point on the curve in a infinite loop.
  At each iteration, the voltage perturbations modify the output power: if the power variation (ΔP) is higher than zero, it means that the power point is not reached yet and the algorithm proceeds to increment with the same trend[6] the

[6] The variation will be the same with respect to the previous one

output voltage value with a new perturbation. Instead, if the power variation is negative, the algorithm proceeds to increment with the opposite trend the output voltage.
The P & O continues to operate until the power reaches a value near to the MPP, but without stopping, causing power oscillation at the output.

- *Incremental Conductance*: represents a clear solution that does not suffer of the power oscillation at the output, as it happens with the P & O strategy.
  The INC algorithm is also an iterative method, that aims to calculate the conductance (incremental and instantaneous) by the computation of the voltage variation and the current variation between each step. Looking at the situation from a mathematical point of view, it consists of:

  $$P_{PV} = V_{PV} \cdot I_{PV} \tag{4.38}$$

  That represents the output power of the PV panel. Applying the derivative to the eq. 4.38

  $$\frac{dP_{PV}}{dV_{PV}} = \frac{d(V_{PV} \cdot I_{PV})}{dV_{PV}} = I_{PV} + V_{PV} \cdot \frac{dI_{PV}}{dV_{PV}} \tag{4.39}$$

  The maximum power point presents a derivative of the power with respect to the voltage forced to

  $$\frac{dP_{PV}}{dV_{PV}} = 0 \tag{4.40}$$

  Using the relation in 4.41 and placing it in 4.39, it is possible to discover that:

  $$\delta G = \frac{dI_{PV}}{dV_{PV}} = -\frac{I_{PV}}{V_{PV}} = g \tag{4.41}$$

  in which δG is the incremental conductance and g is the instantaneous conductance.

  In each step of this iterative algorithm the two conductance are calculated and compared, finding the position of the working point of the system:
  if $\delta G = g$ it means that the $\frac{dP_{PV}}{dV_{PV}} = 0$ and the working point is on the maximum power point of the system. Each of these strategies can be updated by the introduction of a custom-made solution, in which the iteration step could be variable.

4.5 Thermal model and efficiency evaluation

The choice to use PLCES workspace to perform the simulations is based on the possibility to implement a custom made thermal model, using as reference the manufacturer datasheets of the chosen devices. In particular, it is possible to calculate with high precision how much energy is wasted in each cycle of operation of the inverter and boost transistors, also computing the internal temperature reached during the simulation.
The losses calculation are crucial for the sizing of a proper system also from an economic point of view, presenting at the end of this project an optimized solution that takes in consideration all of these aspects.

4.5.1 Thermal Equivalent

The thermal modeling is mandatory to estimate the total losses of the converter, which are divided in two main components: the conduction losses and the switching losses.
To size and project a suitable converter for the application chosen, it is important to select the topology of transistor used in each stage of conversion. The state of the art for the solar generator inverter (and DC/DC stage) is to adopt IBGT modules, due to the high current blocking capacity of the IGBT solution and the low frequency (50 Hz) of the output signal, that does not require a fast switching frequency (in which devices like MOSFET or GAN transistors perform better).
The thermal analysis estimates the heat flowing into the junction and the temperature reached by the component during a cycle of operation. If the temperature exceeds a specific threshold, the power devices could be irreversibly damaged. After the choice of a specific IGBT module for each topology, in this section is provided the procedure to realize a thermal equivalent based on the junction packaging data given by the manufacturer.
The model uses the equivalence between thermal and electrical quantities following two possible different solutions:

- *Cauer thermal model:*
  Is a equivalent model that has a physical meaning, in which the current generators correspond to losses in power devices ($I = P_{loss}$), the RC networks represent the heat flow path and the thermal storage for each layer of material (junction to case, case to heatsink and heatsink to ambient), shown in fig. 4.17

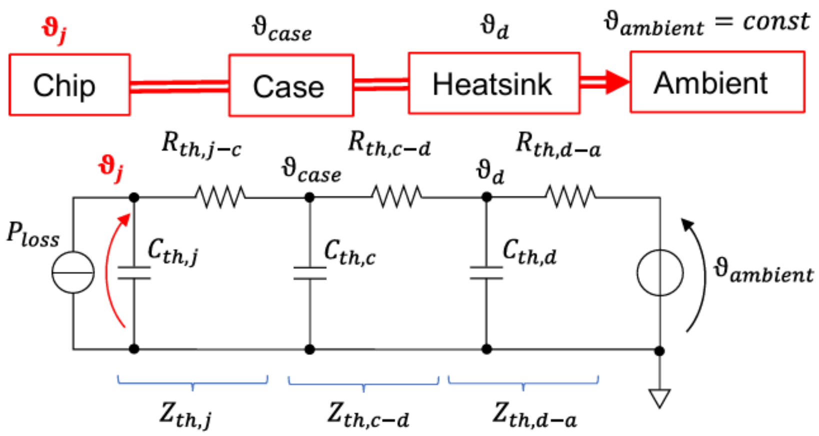

Figure 4.17: Cauer thermal equivalent of a power module

- *Foster thermal model:*
  Is a mathematical approximation of the Cauer model, that does not have a physical meaning. The structure is a series connection of three RC groups having different constants.

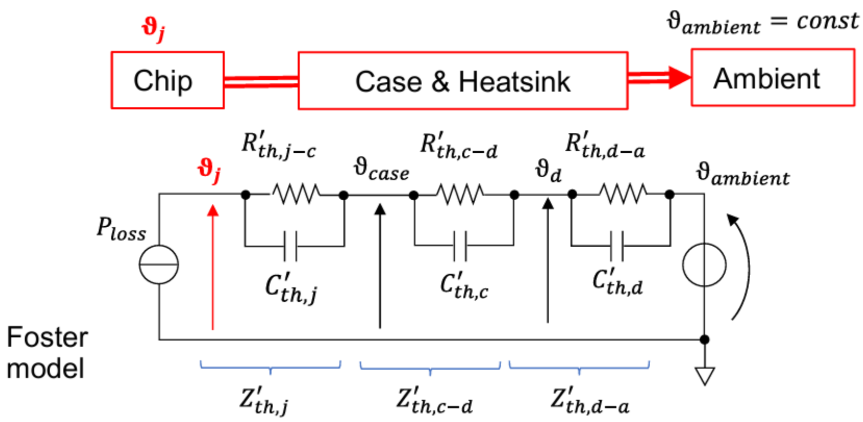

Figure 4.18: Foster thermal equivalent of a power module

Using this equivalence, it is possible to extrapolate the temperature of the junction using

$$\Delta\theta_{ja(t)} = P_{loss} \cdot Z_{th_{j-a}} \tag{4.42}$$

where $Z_{th_{j-a}}$ is the junction to ambient thermal impedance as the total of the three impedance shown in fig. 4.18.

4.5.2 Chosen Power Devices for each Topology

The sizing of the thermal equivalent starts with the choice of a suitable IGBT module for each topology under analysis, based on the power requested by the converter chosen in Chapter 2. In fig. 4.19 is shown the canonical structure of the thermal packaging for the chosen IGBT modules.

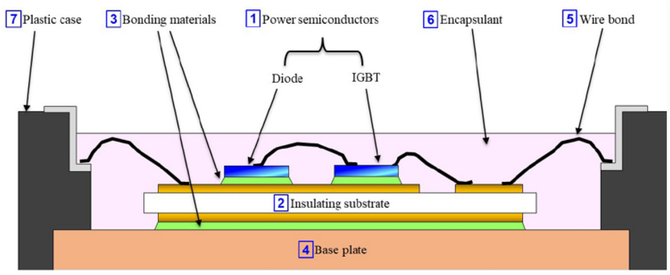

Figure 4.19: Conventional power module thermal package

Centralized topology inverter module

The selected module for the centralized topology is the *FF1200R12IE5* produced by Ifineon [12]: it must satisfy the main crucial aspects summarized in tab. 2.2, 2.3 and 2.4.
It presents a thermal package with a lower side base plate heatsink (which dissipates heat with high efficiency, most common solution for high power device) made of Cu and an internal isolation layer made of Al_2O_3.

FF1200R12IE5	Value	Unit
V_{CE}	1200	V
$I_{C_{DC}}$	1200	A
V_{GE}	+-20	V
$R_{Th_{j-c}}$	28,7	K/kW
$R_{Th_{c-h}}$	22,1	K/kW

Table 4.4: Centr. IGBT module general data

It is important to underline that for a correct implementation of the chosen centralized IGBT module, more than one single device is needed to perform the power conversion, since the current that flows into the junction reaches over 3000 ampere in case of high irradiance values. A parallel connection between three of these devices presents an equivalent transistor able to withstand the converted currents.

Multi-string topology inverter module

For the Multi-string topology, the selected module has to follow the specifications about voltage and current described in tab. 2.8, 2.9 and 2.10.
Looking in this direction, the selected component is the model *NXH350N100H4Q2F2P1G* produced by Onsemi [13] a hybrid Si/SiC (silicon carbide) module with high efficiency and robustness.
It also presents a base plate heatsink configuration on the lower side (the thermal specification for the three solutions are chosen as similar, to reduce the thermal resistance estimation used for PLECS simulations).

NXH350N100H4Q2F2P1G	**Value**	**Unit**
V_{CE}	1000	V
$I_{C_{DC}}$	303	A
V_{GE}	+-20	V
$R_{Th_{j-c}}$	0.22	K/W
$R_{Th_{c-h}}$	0.12	K/W

Table 4.5: Multi-string IGBT module general data

String topology inverter module

The chosen device, as the one used in the centralized topology, is produced by Ifineon, but with a different size in terms of current and voltage, due to the considerable difference in power of the two solutions. The selected model is *FF400R07KE4* [14]:

FF400R07KE4	**Value**	**Unit**
V_{CE}	650	V
$I_{C_{DC}}$	400	A
V_{GE}	+-20	V
$R_{Th_{j-c}}$	0.22	K/W
$R_{Th_{c-h}}$	0.06	K/W

Table 4.6: String IGBT module general data

All the switching and conduction losses characteristics of these three modules are reported in relative datasheets, in which the evolution of the curves is given for different operative temperature by the manufacturer.
This relations are reported directly into PLECS Workspace in thermal description area to run the simulation and estimate the efficiency.

4.5.3 Thermal model implementation on PLECS

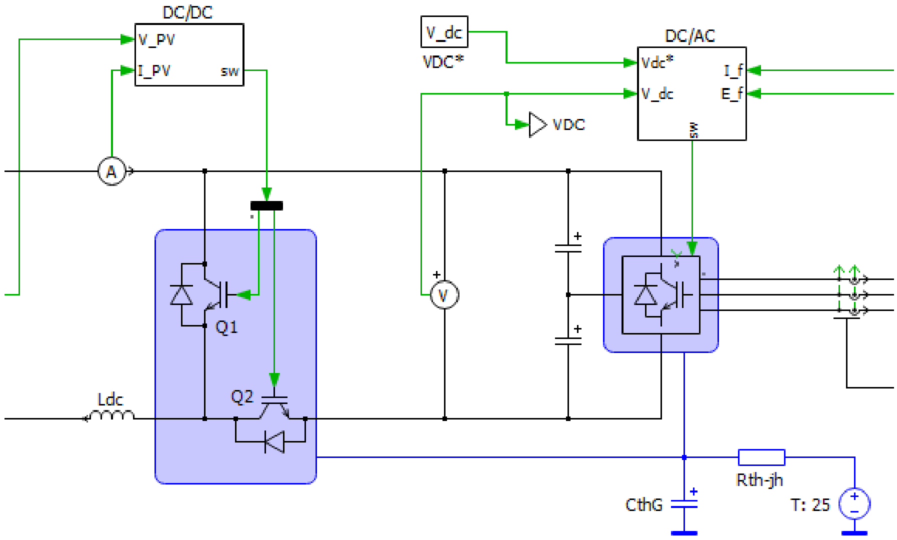

Figure 4.20: PLECS simulation model with thermal equivalent

The dissipation strategy adopted by PLCES simulation follows the mathematical thermal equivalent described by the Foster and Cauer models and is implemented by the virtual heatsink schematic shown in fig. 4.21. To calculate the equivalent thermal resistance and capacity, data are taken from the tab. 4.4, 4.6 and 4.5 and added to the dissipation structure described in fig. 7 The total junction to heatsink

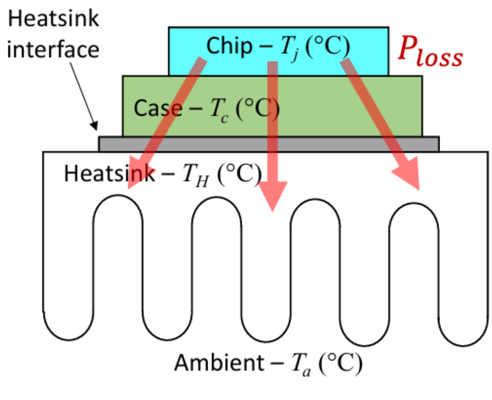

Figure 4.21: Thermal structure adopted

resistance is

$$R_{th_{j-h}} = R_{th_{j-c}} + R_{th_{c-h}} \tag{4.43}$$

where $R_{th_{j-c}}$ and $R_{th_{j-c}}$ are respectively the junction to case resistance and case to heatsink resistance.

	FF1200R12IE5	NXH350	FF400R07KE4	Unit
$R_{Th_{j-c}}$	0.0287	0.22	0.22	K/W
$R_{Th_{c-h}}$	0.0221	0.12	0.06	K/W
$R_{Th_{j-h}}$	0.0508	0.34	0.28	K/W

Table 4.7: Total thermal resistances

For the thermal capacity, the numerical value depends by the heatsink material, the thickness and the working temperature. Using an approximation for the composition of the dissipation layer, the most common value for an aluminum plate is:

$$C_{th} \approx 1450\ J/K \tag{4.44}$$

Since the thermal model evaluates the power losses of each transistor involved in conversion, it is possible to calculate from the PLECS schematic the efficiency following the relation:

$$\eta_{conversion} = \frac{P_{out}}{P_{in}} = \frac{P_{DC} - P_{loss}}{P_{DC}} \tag{4.45}$$

which is implemented in PLECS in fig. 4.22

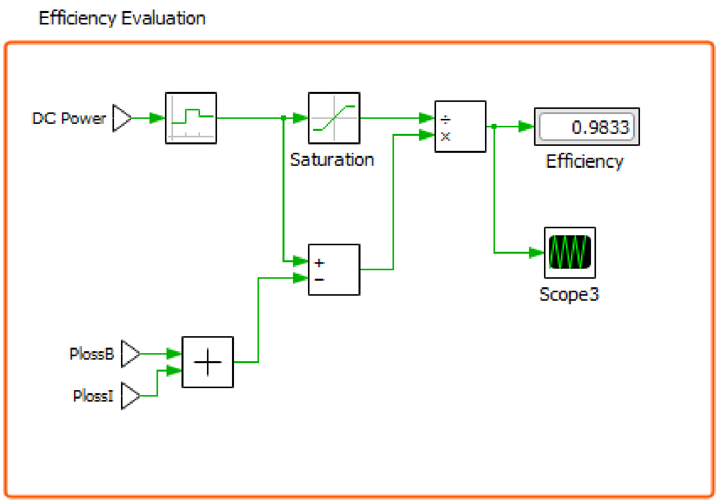

Figure 4.22: Efficiency calculation schematic

Chapter 5

Simulations results

In this section all the simulation results are reported for each kind of topology following a series of different steps:

- Definition of the solar average irradiance daily cycle, for the selected location in a specific moment of the year.
- Validation of the MPPT strategy, with the purpose of extracting the maximum power from the PV module.
- Solar generation plant simulation, focusing on electrical quantities and their variation during the daily cycle.
- Calculation of efficiency and losses for the selected plant topology

5.1 Plant simulation model on PLECS

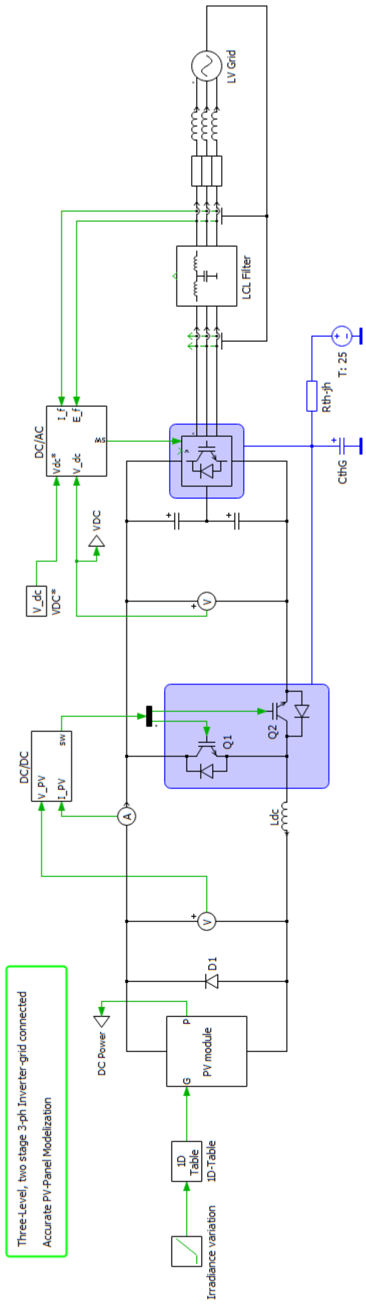

Figure 5.1: Complete PLECS simulation model

The final step of this elaborate is to use all the considerations about the different parts of a solar generation plant made in the previous sections, to implement a

simulation model on PLCES that is able to work under a specific set of conditions, giving a complete overview on electrical and thermal quantities to compare different solutions in a practical way.
The complete simulation model is presented in fig. 5.1.
The working parameters are summarized in tab. 5.1, 5.2 and 5.3.

Centralized Plant	**Parameter**	**Unit**	**Description**
V_{DC}	1200	V	DC-Link chosen Voltage
P_N	2.5	MW	Inverter Nominal Power
C_{DC}	0.05526	F	DC-Link capacitor
C_{PV}	1	μF	PV panel internal capacitor
R_g	0.01	Ohm	Grid equivalent resistance
L_g	10	μH	Grid equivalent inductance
L_{f1}	12.124	μH	Inverter side LCL filter inductance
L_{f2}	6.0619	μH	Grid side LCL filter inductance
C_f	0.002006	F	LCL filter capacitance
R_d	0.00635	Ohm	LCL filter damping resistance
L_{DC}	576	μH	Boost input inductance

Table 5.1: Plant simulation parameters - Centralized Topology

Multi-string Plant	Parameter	Unit	Description
V_{DC}	800	V	DC-Link chosen Voltage
P_N	50	kW	Inverter Nominal Power
C_{DC}	0.00248	F	DC-Link capacitor
C_{PV}	1	μF	PV panel internal capacitor
R_g	0.01	Ohm	Grid equivalent resistance
L_g	50	μH	Grid equivalent inductance
L_{f1}	606	μH	Inverter side LCL filter inductance
L_{f2}	303	μH	Grid side LCL filter inductance
C_f	40.11	μF	LCL filter capacitance
R_d	0.32	Ω	LCL filter damping resistance
L_{DC}	0.0128	H	Boost input inductance

Table 5.2: Plant simulation parameters - Multi string Topology

String Plant	Parameter	Unit	Description
V_{DC}	600	V	DC-Link chosen Voltage
P_N	12.5	kW	Inverter Nominal Power
C_{DC}	0.01105	F	DC-Link capacitor
C_{PV}	1	μF	PV panel internal capacitor
R_g	0.01	Ohm	Grid equivalent resistance
L_g	10	μH	Grid equivalent inductance
L_{f1}	2.4	mH	Inverter side LCL filter inductance
L_{f2}	1.2	mH	Grid side LCL filter inductance
C_f	10.3	μF	LCL filter capacitance
R_d	1.2696	Ohm	LCL filter damping resistance
L_{DC}	0.0288	H	Boost input inductance

Table 5.3: Plant simulation parameters - String Topology

5.2 Average solar cycle definition

The definition of the average solar daily cycle of irradiance is realized to test the plant following the evolution of available irradiance during a specific period of time. The irradiance input is presented at the LUT of the chosen PV panel, to obtain a specific value of photogenerated current and voltage, to find how the system behaves if it is realized in the selected location with the chosen components.

It is important to underline that the software PLECS is studied do return simulations results with a reduced time span of a few seconds, to analyze the behavior of an electric converter even in transient operation: the simulations are conducted over a time horizon significantly shorter than the 24 hours of a full day. However, this does not constitute a problem since the MPPT algorithm is able to bring the photovoltaic generator to an operating point close to the MPP in a few seconds. Consequently, if in the simulated environment changes the irradiance in input in a time span larger than the simulated one, is possible to presume that the closed-loop regulation is able to adapt the output even in an extended simulation.

The chosen irradiance profile is the one adopted in 3.5 in the previous chapter, using PVGIS software to obtain the values. The input 1D LUT is implemented in PLECS as fig. 5.2 shows. In a real operation inverter, there is a limitation on

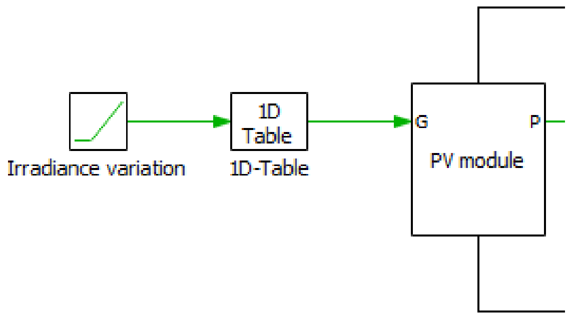

Figure 5.2: 1D LUT irradiance profile on PLECS

the minimum admissible irradiance that generates a power output. The reason behind this limitation is related with the MPP tracking algorithm, which fails to find the correct voltage value to give as reference for the DC/DC control, when the irradiance level is under a certain threshold. This error is not avoidable, at least with a MPPT strategy that does not include specific custom-made solution that can be adopted if the average irradiance level does not reach.

5.3 MPPT implementation and validation

Looking at the previous chapter, it is important to implement a correct MPPT algorithm to exploit the solar generator at maximum of its potential, with the aim of making the system work close to the point with the highest power.
The chosen strategy for MPPT is a *Perturb & Observe* algorithm that starts from a constant voltage level calculated starting from the open circuit voltage given by the panel manufacturer.
The implemented algorithm is visualized in fig. 5.3
The iteration is performed using a Zero-Order Hold (ZOH) block to read the input

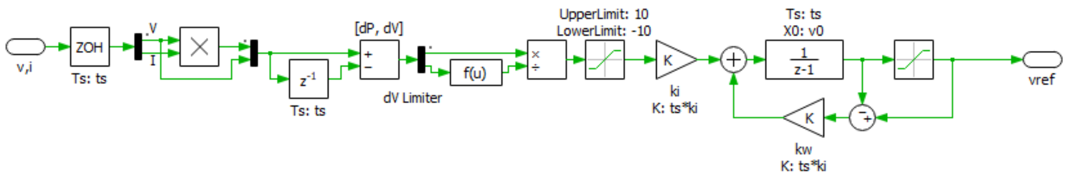

Figure 5.3: MPPT algorithm implementation on PLECS

voltage and store until the next sampling. The measured voltage and current are computed to obtain the power and calculate the voltage and power variation that are the control condition for the *P & O* technique.
Looking at the sign of the power variation and the voltage variation, the function of Perturb & Observe calculates a reference power and, after an integration step with specific limits (that change between the different inverter MPPT working conditions) the reference value is obtained at the output. The input voltage used at the first iteration is calculated as:

$$V_{ref_{init}} = V_{MPP_{approx}} = 0{,}8 \cdot V_{OC_{panel}} \tag{5.1}$$

founded looking at tab. 3.3, described in the previous chapter.

5.3.1 Maximum power point detection results

The first simulation executed wants to validate the MPPT algorithm analyzing the output power of the PV module[1]. The chosen value of irradiance is fixed at the STC conditions, which presents the ideal situation to test the algorithm.

[1]The simulation results presented to test the MPPT technique are based on the high power centralized inverter topology, but the algorithm is realized to work in each of the following topology solutions

The simulation time is reduced to 5 seconds, because the DC/AC converter control reaches the steady-state value quickly, since the input irradiance is considered as the ideal STC conditions.
In fig. 5.4 is show the algorithm voltage detection for the chosen output power:

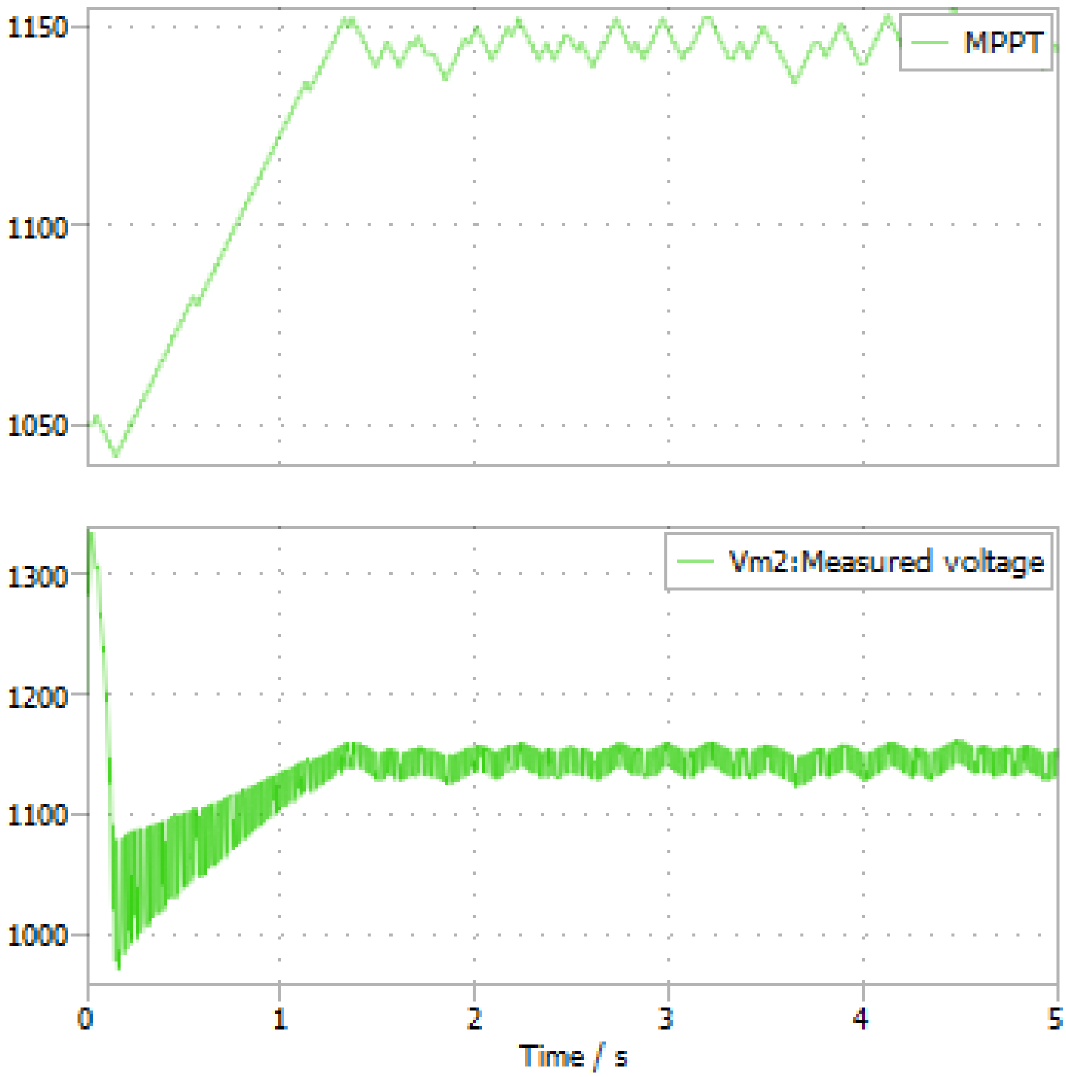

Figure 5.4: MPPT tracking Voltage (1) - Output Boost Converter Voltage (2)

starting from the 80 % of the total open circuit voltage (almost 1000 V), it quickly reaches the $V_{MPP} \approx 1145\ V$.
The Boost converter is able to respond at the MPPT reference voltage command with enough accuracy (even in the initial transient phase, that presents some

unavoidable oscillations) permitting to extract the maximum power possible from the panel. In fig. 5.5 is reported the power output of the PV module, which reaches $P_{DC} \approx 2.2\ MW$, that is the expected value for the chosen module configuration, summarized in the tab. 5.1. However, is possible to reach the nominal power value of $2P_{DC} \approx 2.5\ MW$, simply by increasing the input irradiance from the STC value to the maximum expected value detected by PVGIS and reported in tab. 3.1.
It is also reported the performance of the inverter DC-link voltage control, which is able to keep the $V_{DC} = 1200\ V$ as requested by the application. By using different

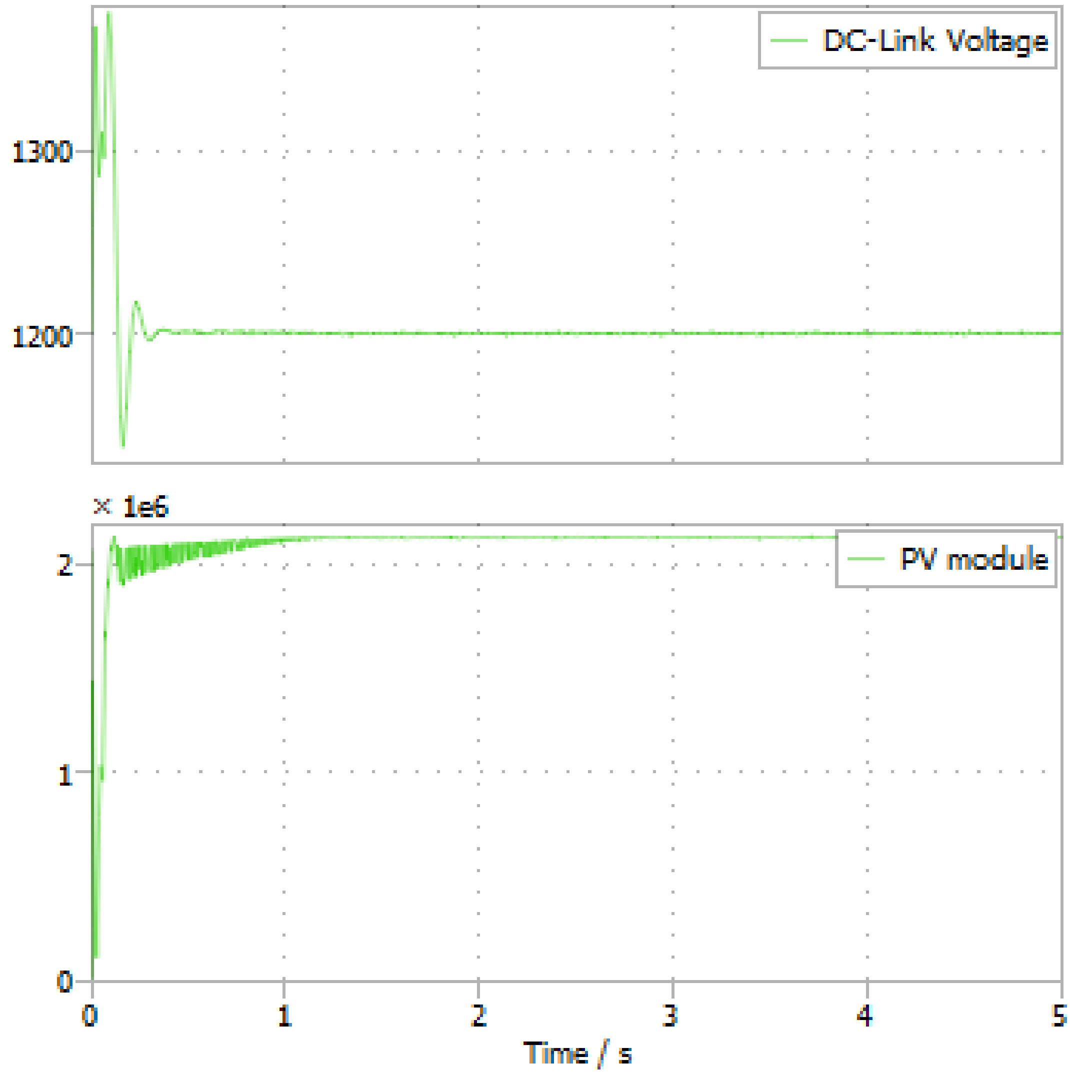

Figure 5.5: DC-Link controlled Voltage - PV Output DC Power

scopes to extract the DC power and voltage produced by the panel, it is possible to visualize the P-V characteristic of the equivalent module: the maximum reached power corresponds to the one defined in tab. 3.3 of $P_{MAX} \approx 610\ W$, as shown in fig. 5.6.

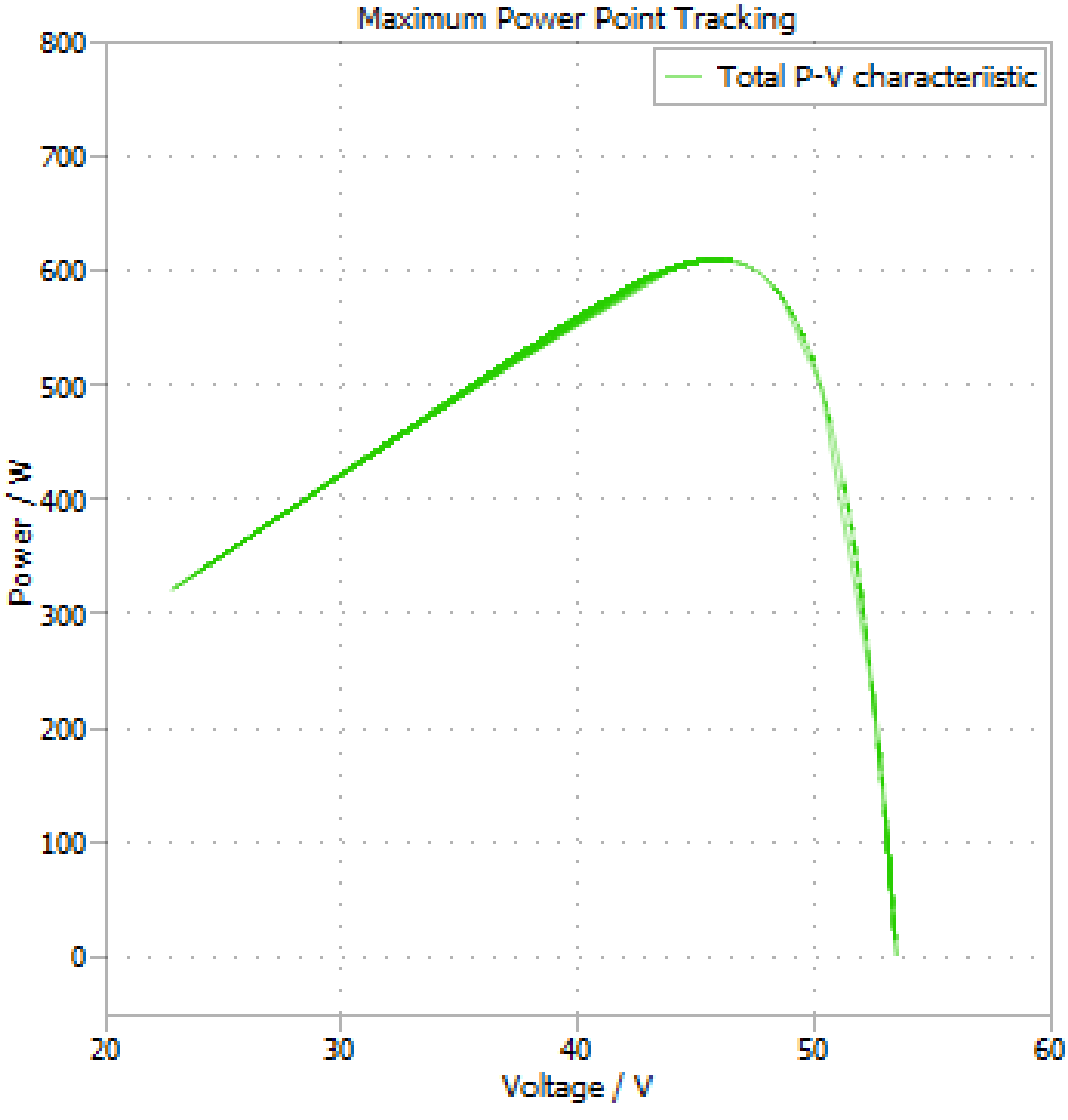

Figure 5.6: P-V simulated panel characteristic

5.4 Plant performance Evaluation

The following section focuses on the performance of each different part of the modeled plant, under different operational conditions, starting from the average cycle of irradiance measured for the target site, up to the maximum irradiance and generation profile.

5.4.1 Centralized plant performance evaluation

Using all the simulation parameters presented in tab. 5.1, with an irradiance input cycle defined in fig. 5.2 it is obtained as output from the model the following characteristics:

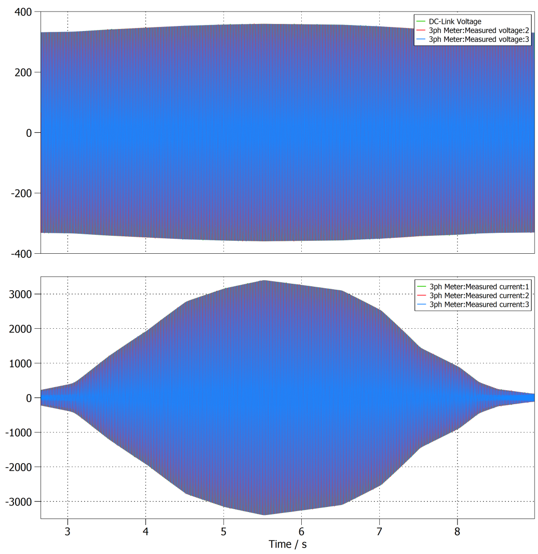

Figure 5.7: Grid quantities evolution - daily cycle

Looking at the fig. 5.7 and 5.8 is possible to visualize the evolution of the injected current that starts from zero, when there is a null value of irradiance impacting the panels, up to the maximum current available of over 3000 A. Looking at the AC Voltage level at the grid, is perfectly contained by the control in a range close to the $V_{AC_{rms}} = 230 \cdot \sqrt{2}$, which is the common standard for low level voltage application (the value changes a bit during the operation, due to the dissipation action of the internal resistance, like the grid one or the damping resistance of the LCL filter). The devices chosen for the internal structure of the inverter are able to withstand such a current without involving the overcurrent protection devices.

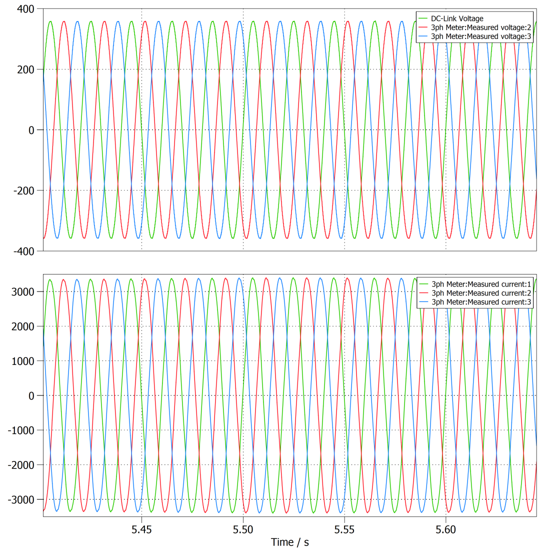

Figure 5.8: Grid quantities zoomed detail in the MPP

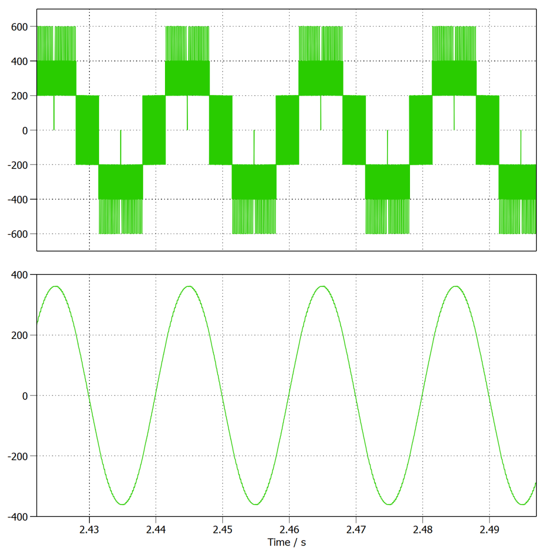

Figure 5.9: Filtering effect on the three level output voltage - phase a

The profile of the injected current follows the irradiance cycle of an average day in July, presenting a peak output power near midday od 2.035 MW DC (fig. 5.10). The expected value of 2.4-2.5 MW is reached only if the incoming irradiance exceeds the value of 1000 W/m^2, expecting a over-production of the selected module, accounted in the previous by the section of NPR parameter.

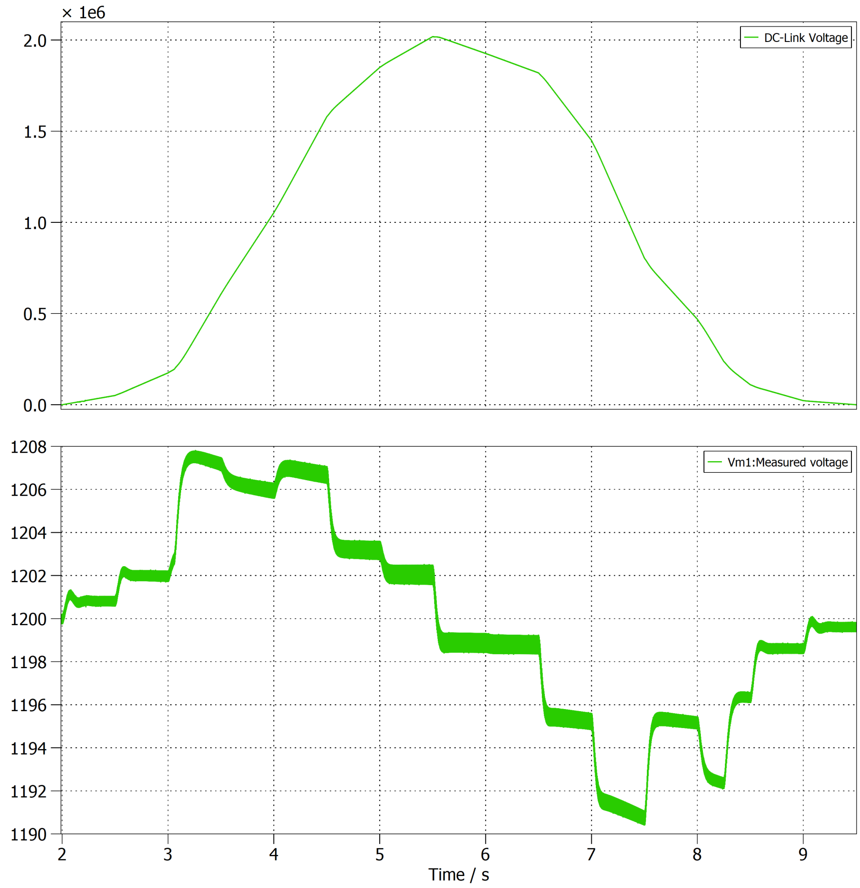

Figure 5.10: DC output Power (1) - DC-link Voltage

For the regulation of the DC-link voltage, in the selected area it is possible to observe a variation from the target value of 1200 V, selected by the inverter voltage control. This is caused by the time scale of the simulation, much faster than a real average converter operation. In fact, since the irradiance rapidly changes from its 20% to the 100 % in a couple of seconds, the converter control does not maintain the chosen level on the DC link always on the selected 1200 V.
However, the percentage of variation of the DC-link voltage presents a $\Delta V_{DC} \approx 16\ V$, above the allowable range for the DC-link capacitor of $\pm 5\%$ of V_{DC}.

5.4.2 Thermal results and Efficiency evaluation

In fig 5.12 is shown the evolution of the thermal losses (expressed in Joule) during the daily cycle operation: the critical part for the dissipation of energy is focused

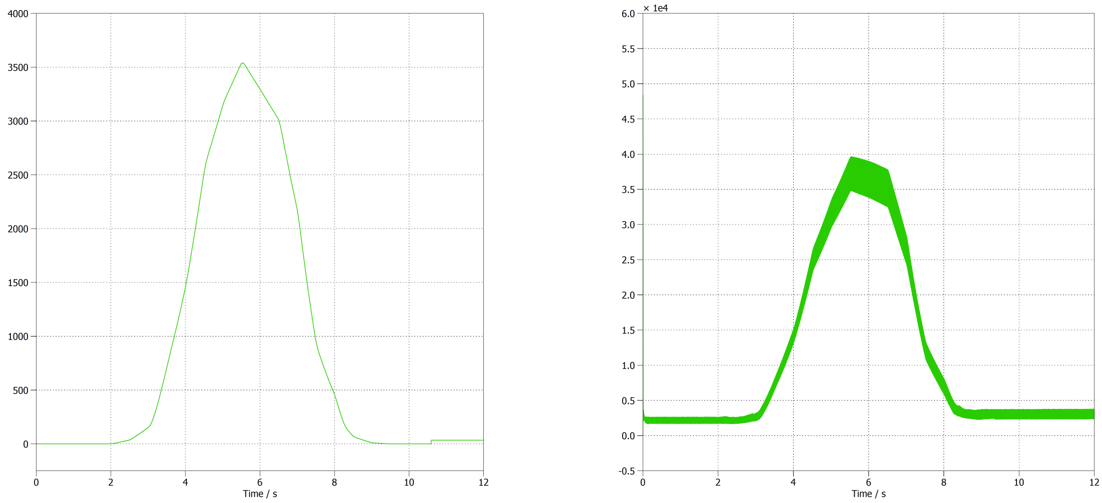

Figure 5.11: DC/AC and AC/AC switching and conduction Losses

for the majority on the DC/AC conversion, since the equivalent structure of the three-level inverter presents a considerable amount of transistors, to perform the electrical conversion.
The energy computation takes into consideration the switching losses, which are influenced by the wasted energy during the turn-on or turn-off operation (directly related to the value of the switching frequency of the converter) and the conduction losses, which depends on the physical characteristic of the chosen device. For a solar generation converter, which presents really high power and high current flowing in the transistors (several thousand of amperes), it is common sense to choose low switching frequency (5-10 kHz), reducing the switching losses and improving the efficiency of the conversion.

The total efficiency of the conversion is computed using the schematic presented in fig. 4.22, with the following results:

It is possible to observe that the PV generator begins to inject power into the grid only if the irradiance exceeds a target threshold and stays above the requested value to simulate the centralized topology (tab. 2.2). The peak value of efficiency is reached at the beginning and the end of the cycle, when the photogeneraed current is lower than the nominal value: this probably because the thermal losses of the power device depends on the current that flows into the junction, which is lower in these time intervals.

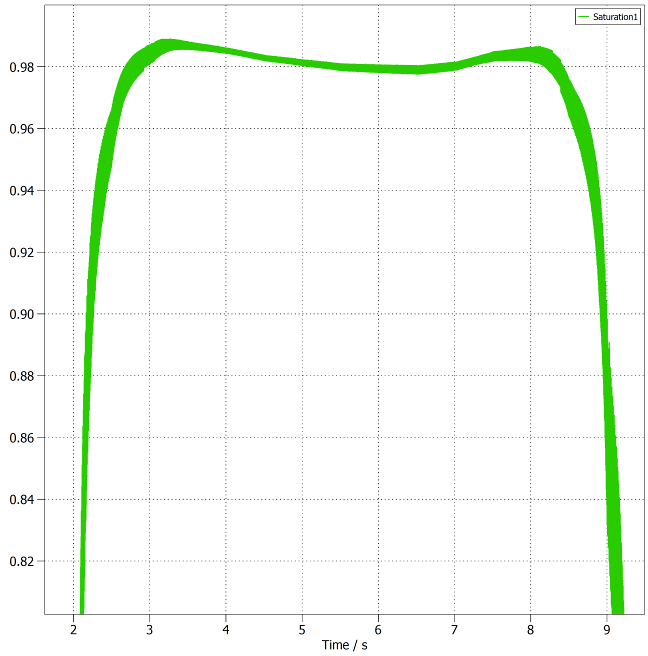

Figure 5.12: Efficiency profile - daily variation

	Parameter	Unit
Peak Efficiency	0.985	-
Average Efficiency	0.98	-

Table 5.4: Centralized topology daily cycle efficiency

5.4.3 Multi-string plant performances evaluation

The model can be adapted to simulate a multi-string solution by modifying the parameters of the plant as the tab. 5.2, by adapting the power settings of the converter and the equivalent structure of the PV panel, to provide the correct value of photo-generated current as the input of the plant (tab. 3.5).
For the efficiency evaluation, also the thermal library needs to be updated following the switch specification summarized in tab. 4.5. The results of the simulation plant defined as before are reported in the following diagrams: The output DC power stays below the threshold of 50 kW requested, to perfectly match the calculations made to avoid the saturation of the converter due to the increasing of the irradiance when the maximum value is reached. If the panel is mounted in a different location, is possible to increase the NPR value to modify the number of series and parallel connection of the equivalent module to produce more than 50 kW during a daily

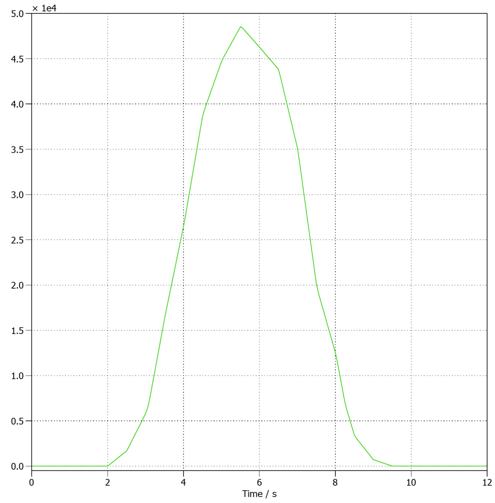

Figure 5.13: DC output Power

cycle. The grid quantities showed in fig. 5.14 follows the generation profile reaching the target grid voltage output chosen by the inverter control.

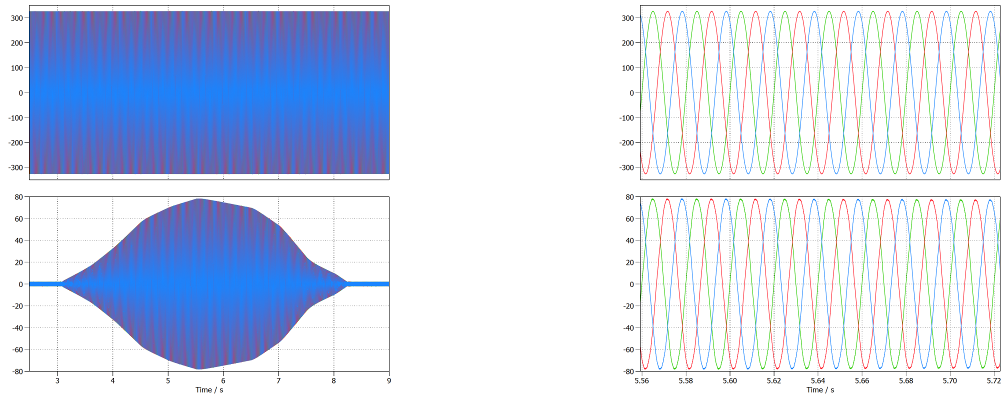

Figure 5.14: AC grid quantities with a zoomed detail in the MPP

Updated the equivalent thermal resistance for the chosen IGBT module 4.5, the total losses are summarized in fig. 5.15

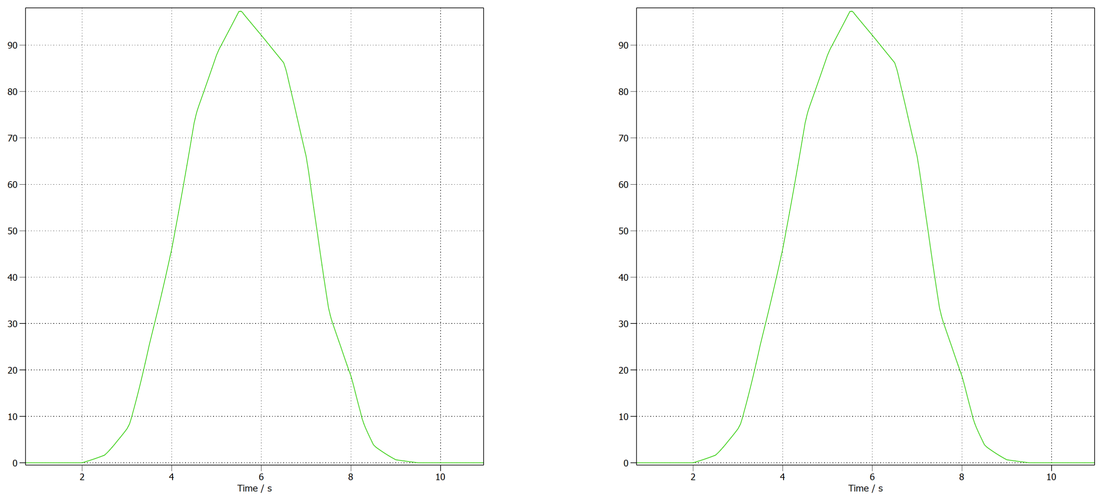

Figure 5.15: DC/DC converter total losses (1) - DC/AC converter total losses (2)

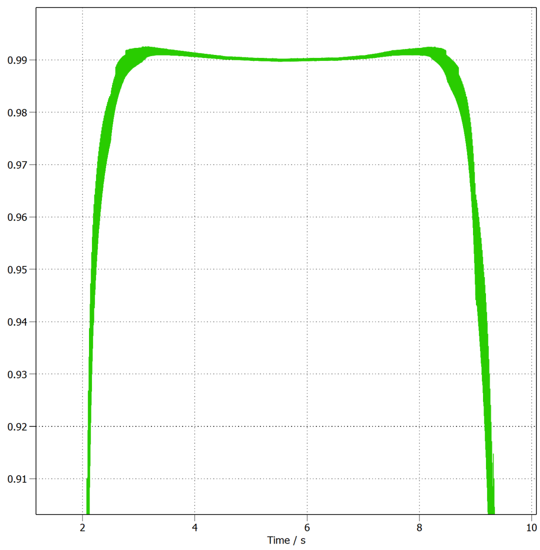

Figure 5.16: Efficiency cycle for multi-string topology

The estimated value for the multi string topology efficiency reaches a peak value over the 99 % that is higher than the previous solution: the results are obviously affected by the thermal model of the converter, which is constructed starting from the IGBT model selection. The multi-string topology has a considerable average power size lower than the centralized one, and probably for this reason, is more efficient to adapt the output at the irradiance variation cycle.

	Parameter	Unit
Peak Efficiency	0.992	-
Average Efficiency	0.989	-

Table 5.5: Multi-string topology daily cycle efficiency

5.4.4 String plant performances evaluation

The last topology simulated is the string plant, which presents the lowest possible number of parallel connection (2 in this case due to the choice of a specific 2 MPPT channels converter), and a power size of 12.5 kW. The concept above the realization of a large scale string plant is quite singular, since this solution is not employed in the reality for economic reasons, but is mandatory in this case to perform a complete comparison between each solution.
The simulation parameters summarized in tab. 3.6 and the thermal quantities described in 4.6 are inserted into the model, giving the following results:

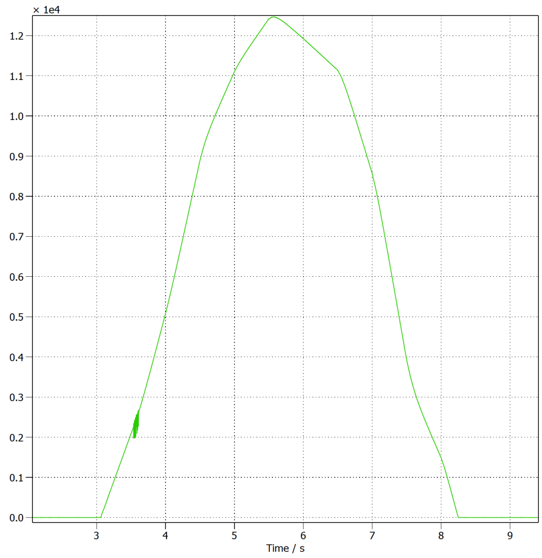

Figure 5.17: Dc output Power

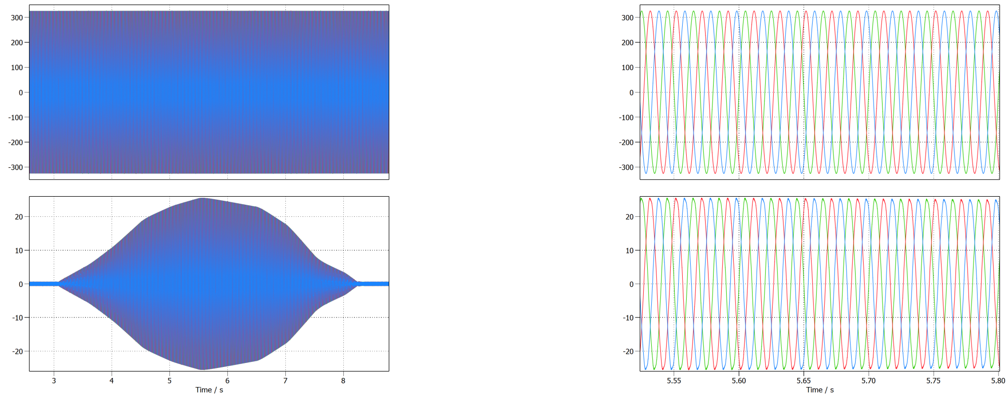

Figure 5.18: AC grid quantities with a zoom in the MPP

The output power (in fig. 5.17) and the output grid quantities (in fig. 5.18) are following the expected profiles, with a maximum generation when the sun irradiance reaches its maximum keeping the output voltage value constant on the European fixed level (as in the previous cases).
The dissipation of energy, in this case, is little less efficient than the multi-string topology but higher than the average output of the centralized one.

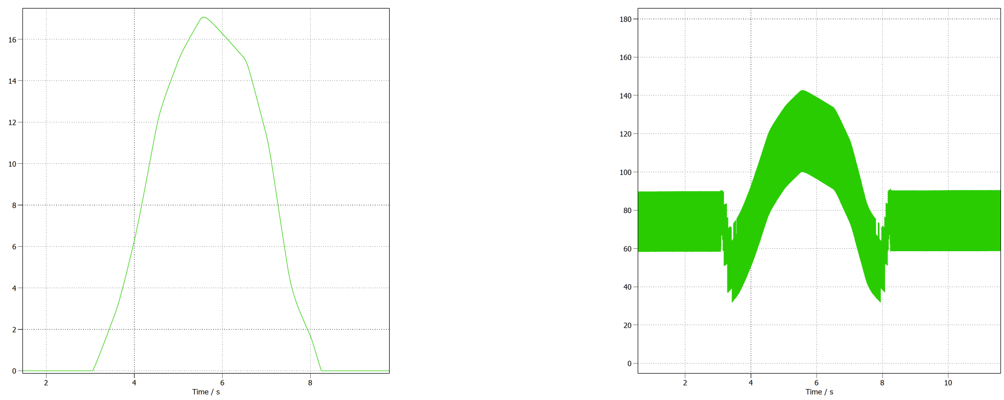

Figure 5.19: DC/DC and AC/DC total switching and conduction Losses

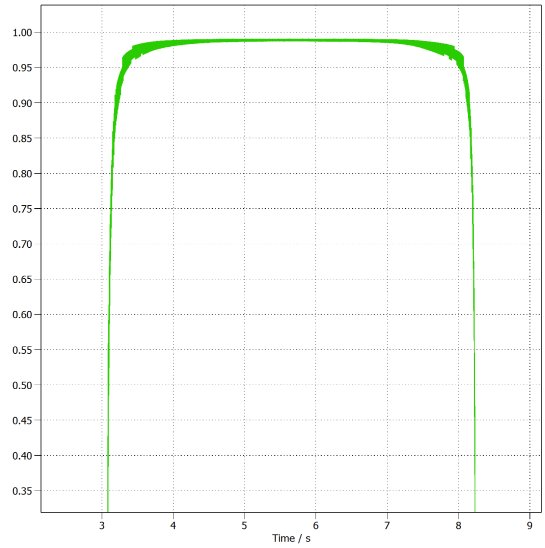

Figure 5.20: Efficiency cycle for string topology

	Parameter	Unit
Peak Efficiency	0.989	-
Average Efficiency	0.987	-

Table 5.6: Multi-string topology daily cycle efficiency

The comparison between the three different topologies points out that, for the chosen model of simulation, the plant responds with a fast dynamic to a variation of the input irradiance, permitting to understand the behavior of each solution. In particular, for the proposed system, the multi-string topology, which represents a compromise between the high efficiency and high robustness of the centralized and the high MPPT resolution of the string, is able to follow the variation of the input irradiance with the total higher efficiency.
Nevertheless, each of the three proposed models fulfills the target expected efficiency behavior described by the datasheets of the chosen components, resulting in a suitable solution from the loss point of view.

Chapter 6

Solar Plant Economic Planning

The implementation of a solar generation power system requires, in addition to a meticulous analysis of the performance and technology involved, a precise planning for cost evaluation and economic impact, especially for a plant of several megawatts. From a cost point of view, in 2023 the global weighted average levelized cost of energy (LCOE) for solar technology decreases by 90 % of its 2010 value, allowing an increase in utilization for this topology for renewable generation [15].
Looking at the cost of photovoltaic panel technology, the average price of a module (from the feedstock to the ship) decreased by 93 % between December 2009 and December 2023. These trends contributed to the reliance on solar generation, increasing the total global average solar generation capacity around the world (only during 2023 the total installed capacity was greater than 1.410 GW).
The reasons behind this growth in the competitiveness of PV are motivated by the continuous research of a sustainable solution in energy production that could lead to a self-sufficient society able to develop without affecting the environment and increasing quality of life. Renewable technologies are the center of this process, and in particular, solar generation is the branch that has experimented with the fastest development in recent years due to a reduction of the technology cost and an increase of the overall efficiency design solution. A general overview is presented in fig.6.1 in which is possible to understand how the most important aspects, such as the total average installation cost, the capacity factor and the LCOE evolved during past years.

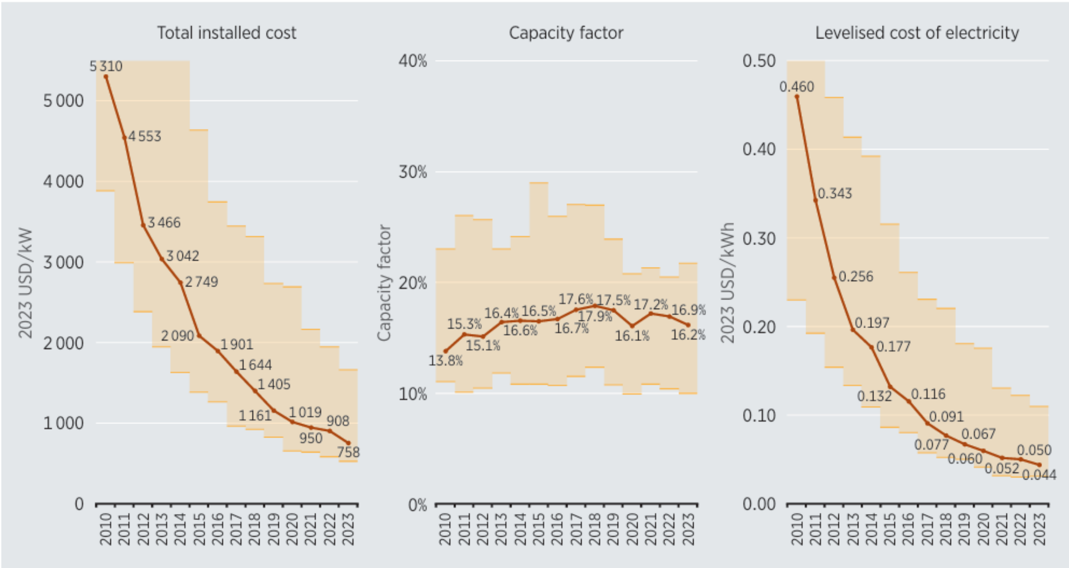

Figure 6.1: Solar technology cost reduction - IRENA [15]

6.1 Total Cost Evaluation

To realize a comprehensive analysis of the economic impact of a solar generation plant, in the following section each part of the system is described from a cost point of view, highlighting the difference and the average prices with the last updated values.
Looking at the situation in more detail, a report of IEA PVPS[1] described in [16] provides a comprehensive description of the total costs applied in the Spanish context, presenting how the projection choice impacts from an economic point of view.
Using this document and the reports [5] and [15], all the relevant aspects are balanced to find the best configuration from an economic point of view.

[1]International Energy Agency - Photovoltaic Power System

6.1.1 PV Module prices trends

The expansion of a precise technology in solar generation is strictly related to the average price of its base unit, the photovoltaic module. The prices of the crystalline silicon module, which is the most widely used technology with the highest average efficiency on the market, varied from 0.11 $\$/W$ for the lower-cost modules, to 0.42 $\$/W$ for higher-cost modules such as bifacial. The situation can be visualized in fig.6.2. Since the selected module for the proposed plant is a n-type

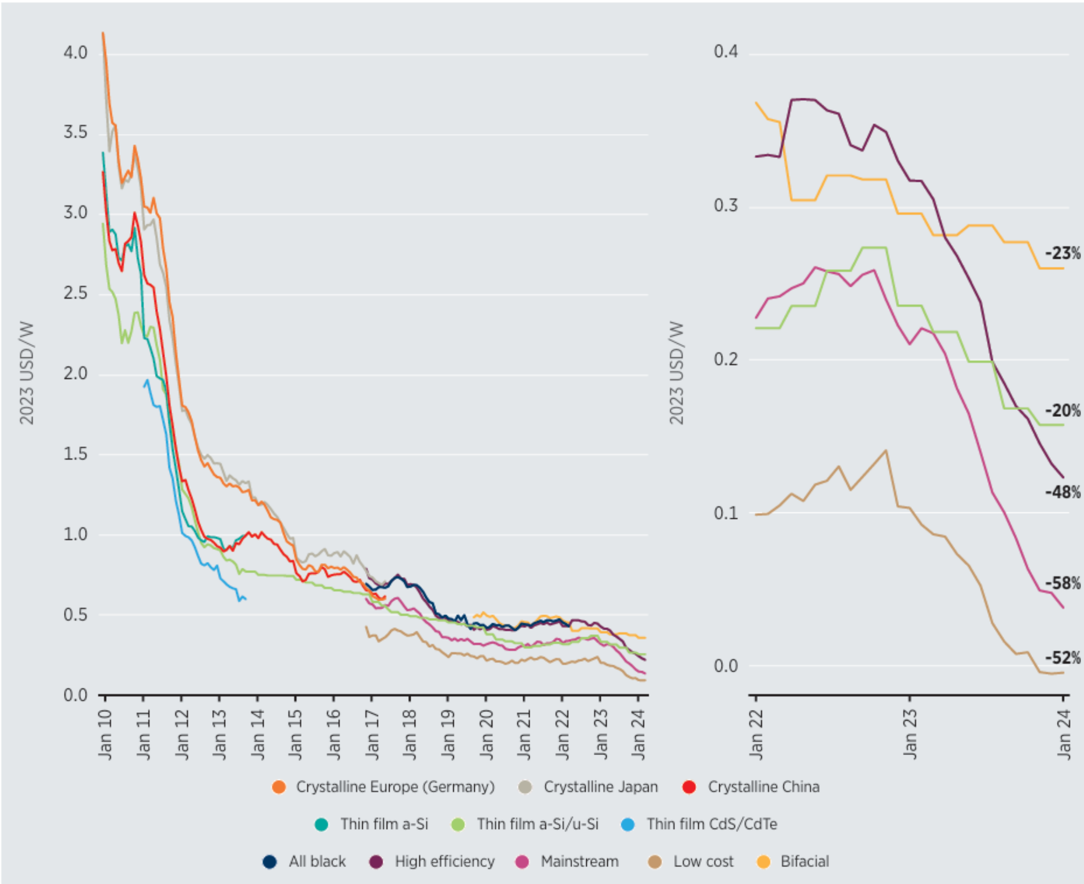

Figure 6.2: PV technologies prices on average

monocrystalline with high efficiency, the estimated average price is 0.23 $\$/W$. This value is representative of the general selected category, but could be affected by the regional price oscillation and the availability of feedstock.

6.1.2 System installation prices trends

Reported PV system prices vary significantly based on factors such as system size, location, customer type, grid connection and technical specifications.
The price of a large utility-scale generation plant starts at approximately 0.758 $\$/W$, considering all the different aspects and components of the system. As expected, the trend has decreased over the years, due to the increasing affordability of resources and common investments in the renewable generation sector.

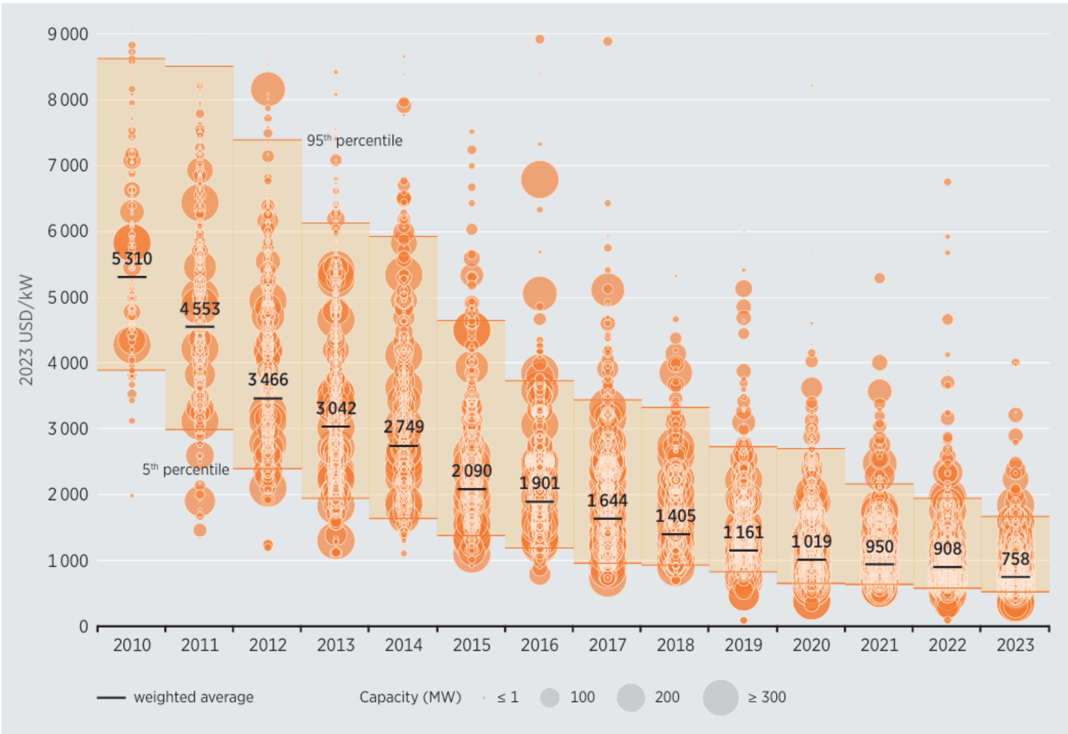

Figure 6.3: Total average system installation costs

To understand what is the best configuration for the plant topology, in the next section a complete review about the different parts is carried out, highlighting the difference on average between a centralized solution and a string/multi-string[2] solution from an economic point of view.

[2]The string and the multi-string topology, from a system installation point of view could be considered as similar, since the power size of the different inverters and the connection strategy are on the same order of magnitude.

6.1.3 Plant Costs Breakdown

The average economic impact is evaluated considering:

- The module average cost, selected in the previous section, which depends by the technology and the availability on the market;
- The inverter cost, which includes the DC/AC converter price and the related transformer;
- The mounting material to install the system;
- The others electrical components cost, which involves cables and protection devices;
- The total soft costs, which does not depends from the selected hardware but are related to the planning, installation, shipping and permissions;

[$ / W]	**Centralized Utility-Scale**	**String & Multi-string**
Module	0.23	0.23
Inverter	0.043	0.129
Mounting material	0.115	0.12
Other electronics	0.35	0.37
Soft costs	0.108	0.108
Total	0.846	0.957

Table 6.1: Total installation costs breakdown

The difference in prices reported in the tab 6.1 are extrapolated from the articles before considering the average price for the string/multi-string inverter as 4 times the price of the centralized one. The higher efficiency in the smaller power-sized solution is reached using an higher number of devices, protections and material, leading to higher costs.
The centralized solution is the system most employed, even if the overall efficiency obtained by the simulation in case of a variation of the solar irradiance, because of the substantial reduction in the average total costs of at least 13 %.
The selected system average planned costs are higher than the value presented in fig.6.3, this probably because of the higher-end devices used for the system definition.

If the target installed power is 275 MW for the selected application, the total amount of initial investment to realize the solar plant becomes:

	Centralized	String/Multi-string	Unit
Total Target Power	275	275	MW
Total cost per W installed	0.846	0.957	$\$/W$
Total planned investment	232.65	263.175	$M\$$

Table 6.2: Total estimated costs

6.1.4 Net Presence Value

After a brief cost evaluation, to realize a complete overview of the project's feasibility, it could be useful to estimate the economic indicators that compute the weight of the investment over time. In particular, in this section the Net Presence Value (NPV) method is presented, which considers the initial investment impact and the yearly revenues calculated on a fixed interest rate.
The NPV is an economic estimation of the time in which the total cost of the investment is payed back, following the relation:

$$NPV = C_I \ + \sum_{k=1}^{N} \frac{R_{PV_k} - C_{OM_k}}{(1 + i*)^k} \tag{6.1}$$

in which C_I and C_{OM_k} are respectfully the initial investment cost and the yearly operative and maintenance costs (estimated as the 1 % of C_I); The interest rate is fixed at 4 %, which is a reasonable value for an industrial ground-mounted installation of this size [16].

To evaluate the time using the NPV method, it is requested to estimate the revenues of the PV solar generation system in a given year. The R_{PV_k} are computed as:

$$R_{PV} = E_P \cdot p_S \tag{6.2}$$

where the E_P is the yearly produced energy (MWh) from the plant and p_S ($\$/MWh$) is the selling price. The first aspect to underline is related to the fact that the selling price for the electricity commodity is constantly varying, since in computed day by day following the trends of the electric market. To present a preliminary solution for the feasibility of this project, the selling price value is fixed at the average price computed in 2023 for the Spanish market, but the social, economic and geopolitical situation heavily modify the revenues during the year.

The annual produced energy depends by:

$$E_P = P_{tot} \cdot Y_R \cdot PR \tag{6.3}$$

in which P_{tot} is the total planned power for the plant (275 MW for the selected application), Y_R is the annual reference yield, which considers the rate between

the total global in-plane irradiation in a specific location and the STC value of irradiance (1 kW/m^2) and PR is the Performance Rate of the generator.
For the chosen location (tab. 3.1), the reference yield production is calculated using PVGIS software, in which a dedicated section is available for productivity estimation using the calculated value for efficiency and losses during a fixed time period.

The performance rate (PR) is the total efficiency of solar generation, which includes:

- DC/AC conversion efficiency (with MPP tracking)
- Intrinsic mismatch and shade efficiency of the module
- Losses due to dirt and unwanted reflection
- Electric losses in cables, protections and diodes
- Over-temperature losses

The value calculated for $PR \approx 0.7 - 0.75$ for the chosen plant configuration.

The data from the economic indicators analysis are collected in the following table for the two different planning solutions: The selling price of electricity is

	Centralized	**String/Multi-string**	**Unit**
Total Target Power	275	275	MW
Y_F - Seville	2201.4	2201.4	$h/years$
PR	0.7	0.7	-
C_I	232.65	263.175	$M\$$
C_{OM}	2.32	2.63	$M\$$
p_S	78.8	78.8	$/MWh
R_{PV}	32.78	32.78	$M\$/years$
NPV >0	10	13	*years*

Table 6.3: NPV evaluation

calculated as the average price presented in the OMIE[3] website in 2023-2024. This value is a strong approximation of the real market situation for the electrical energy: the penetration of renewable energy sources strongly impacts the price in the Spot Market for the electricity affecting the value of this parameter day by day.

[3]OMIE is the designated electric market operator in Spain

The total amount of the initial investment is recovered in less time for the centralized topology: this is the reason behind the choice of the centralized solution, since the related conversion efficiency is approximately the same, but the cost to face is unbalanced. The calculations made in the tab. 6.3 are presented just to give an idea of the economic impact in time, but as stated before, the numbers are really dependent on the selling price of electricity and the total efficiency of the plant (which requires an accurate selection of the components and an estimation of the losses in each part of the system).

The benefits of the string or the multi-string topologies in conversion and in efficiency in case of rapid irradiance variation such as mismatch or shade events, are not enough to justify the higher risk that an investment of this kind could lead in terms of time with respect to the centralized topology one. The market indicator applied in eq. 6.1 is chosen in an optimistic situation: if the selling price is reduced and the real efficiency of the plant is lower than the presented value, the amount of time requested to overcome the investment could increase by several years for the string and multi-string solar generation plants.

Chapter 7

Conclusions

In this project, the realization of a preliminary feasibility study for a large-size photovoltaic plant was carried out, resulting in a detailed comparison between different construction topologies from an efficiency and economic point of view.
Focusing with more detail on the developed work, the starting point was an accurate study of a real time output power data taken on a plant with unspecified inverter and construction topology. The initial aim of this project begins with a complete overview analysis of the available related literature to find the best projecting solution to obtain the same output of power presented by the given data.
My personal contribution was the realization of a complete simulation model of a generic photovoltaic plant with the selected output power target, able to compare different devices found on the market and detect the overall plant behavior and efficiency under different operational conditions.
In particular, the procedure was developed as follows:

- An accurate analysis of the related literature on the most commonly used construction topology for a large-size photovoltaic generation plant.
- The realization of a simulation model, using the PLECS simulation software in which the most important part of a photovoltaic plant was implemented.
- The selection of real devices available on the market for the most important parts of the plant, such as the converters and the PV module for each topology, to realize a thermal model, to find a realistic losses overview in a daily cycle.
- The simulation of each topology under different operational conditions, to find the total efficiency and compare the solutions and finding the most convenient from an energetic point of view.
- After the losses comparison, an economic planning is carried out, looking at economic impact related to the investment that a plant of this kind could lead

during years.

If the choice of a construction topology for a LS-PVP is guided only by the need for the most optimized solution from an efficiency point of view, the multi-string and string solutions are able to respond at changing incoming irradiance from the Sun with higher performance, even if for the presented size of the converters and the output requested power is prohibitive from the number of employed converters and protection devices.
The centralized topology is more straightforward for a solution of this kind, since the overall lower efficiency in the case of changing ambient conditions is counterbalanced with a higher robustness and more options on the market.
The economic analysis strengthens the implementation for a centralized solution, since the realization costs are extremely lower, permitting to recover the investment is a reduced period of time, with respect to the string or multi-string topologies.
For all these aspects, reduced converter size solutions are preferred in a distributed generation solution, in which the total number of required converters is significantly reduced and the potential of this technology could be fully exploited.
Following the future trends presented in the first part of this project, it might be interesting to analyze the situation when the costs of the required components for the string and multi-string solutions becomes comparable with the centralized, making the problem only an efficiency-related analysis in which these topologies shine the most.

Appendix A

Transformations Matrices Adopted

Clarke Transformation - Amplitude Invariant

Given a balanced three-phase system, it is possible to express a generic electrical quantity defined in the three-phase reference frame, in a fixed two-phase reference frame using the Clarke transformation matrix A.
Using the voltage as reference electrical quantity, the Clarke relation could be written as:

$$\begin{bmatrix} V_\alpha \\ V_\beta \end{bmatrix} = \frac{2}{3} \begin{bmatrix} 1 & -\frac{1}{2} & -\frac{1}{2} \\ 0 & \frac{\sqrt{3}}{2} & -\frac{\sqrt{3}}{2} \end{bmatrix} \begin{bmatrix} V_a \\ V_b \\ V_c \end{bmatrix} = A \begin{bmatrix} V_a \\ V_b \\ V_c \end{bmatrix} \tag{A.1}$$

For the signal measurement, could be useful to express the Clarke Inverse transformation A^{-1}, which is defined es follows:

$$\begin{bmatrix} V_a \\ V_b \\ V_c \end{bmatrix} = \frac{3}{2} \begin{bmatrix} \frac{2}{3} & 0 \\ -\frac{1}{3} & \frac{\sqrt{3}}{3} \\ -\frac{1}{3} & -\frac{\sqrt{3}}{3} \end{bmatrix} \begin{bmatrix} V_\alpha \\ V_\beta \end{bmatrix} = A^{-1} \begin{bmatrix} V_\alpha \\ V_\beta \end{bmatrix} \tag{A.2}$$

In PLECS workspace, the two transforms A and A^{-1} are described by the dedicated blocks in fig. A.2:

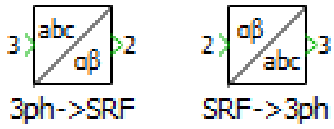

Figure A.1: Clarke PLECS blocks

Rotation Transformation

The equivalent frame synchronous to the rotating axis d,q, can be obtained by the application of the rotational transformation $R(\theta)$ at the (α, β) signal, using the matrix:

$$\begin{bmatrix} V_d \\ V_q \end{bmatrix} = \begin{bmatrix} cos(\theta) & sin(\theta) \\ -sin(\theta) & cos(\theta) \end{bmatrix} \begin{bmatrix} V_\alpha \\ V_\beta \end{bmatrix} = R(\theta) \begin{bmatrix} V_\alpha \\ V_\beta \end{bmatrix} \tag{A.3}$$

and the related Inverse Rotational Transformation, written as:

$$\begin{bmatrix} V_\alpha \\ V_\beta \end{bmatrix} = \begin{bmatrix} cos(\theta) & -sin(\theta) \\ sin(\theta) & cos(\theta) \end{bmatrix} \begin{bmatrix} V_d \\ V_q \end{bmatrix} = R^{-1}(\theta) \begin{bmatrix} V_d \\ V_q \end{bmatrix} \tag{A.4}$$

In PLECS workspace, the two transforms $R(\theta)$ and $R(\theta)^{-1}$ are described by the dedicated blocks:

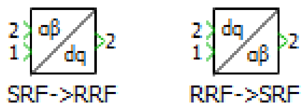

Figure A.2: Rotational Transform PLECS blocks

Appendix B

PI Tuning Section

Current loop PI controller tuning

For the current loop tuning, the block diagram of the situation in the Laplace domain can be summarized as: The system equivalence, neglecting the series

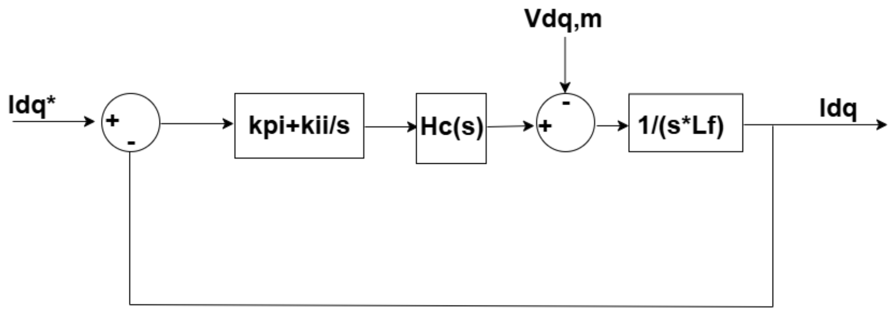

Figure B.1: Inverter Current Control loop in Laplace domain

resistance of the filter and the grid, can be considered as a purely inductive, as the filter inverter side inductance L_f. In the presented schematic, the equivalent converter delay function $H_C(s)$ is presented, in which is considered the effect of the converter presence for the system dynamics.

$$H_C(s) = \frac{1}{1 + s \cdot \tau_{conv}} \tag{B.1}$$

in which the τ_{conv} is the converter's delay. The chosen simulation program, exploits a single sampling control, in which the analyzed electrical quantity is sampled once per switching period introducing a delay between two successive sampling of a $T = T_{sw}$. The total converter delay can be approximated as $\tau_{conv} = 1.5 \cdot T_{sw}$, because of the introduction of a modulation delay due to comparison between the carrier and the modulant of the PWM technique. Starting from this, the open-loop transfer function of the equivalent system became:

$$H_{OL,i}(s) = (k_{p,i} + \frac{k_{i,i}}{s}) \cdot \frac{1}{1 + s \cdot \tau_{conv}} \cdot \frac{1}{s \cdot L_f} \tag{B.2}$$

and the consequent closed-loop function:

$$H_{CL,i} = \frac{s + \omega_{bw}/10}{s^2 + s \cdot \frac{k_{p,i}}{L_f} + \frac{k_{p,i} \cdot \omega_{bw}}{10 \cdot L_f}} \tag{B.3}$$

in which the w_{bw} is the pulsation related to the bandwidth frequency f_{bw} of the chosen current loop. Considering the high frequency approximation, the open loop function becomes:

$$H_{OL,i}(s) \approx \frac{k_{p,i}}{s \cdot L_f} \tag{B.4}$$

Since the bandwidth frequency and the crossover frequency of the system are close to each other and the open loop crossover frequency of the open loop transfer function has a module equal to 1 (0 dB), it is possible to write that:

$$|H_{OL,i}(w_{bw,i})| \approx \frac{k_{p,i}}{s \cdot L_f} = 1 \tag{B.5}$$

obtaining:

$$k_{p,i} = L_f \cdot \omega_{bw,i} \tag{B.6}$$

The integral gain can be calculated imposing a decade of difference between the zero of the regulator and the bandwidth, obtaining:

$$k_{i,i} = k_{p,i} \cdot \frac{\omega_{bw,i}}{10} \tag{B.7}$$

Voltage loop PI controller tuning

The proposed cascaded system presents an outer voltage loop, to regulate the voltage value on the DC-Link. If the chosen bandwidth for the voltage control respects the difference of at least one decade from the current bandwidth, the regulator schematic used to summarize the voltage control can be written in Laplace domain as: The chosen reference DC-Link voltage is selected by the requested level from the inverter datasheet, to perform a correct MPPT algorithm changing the value according to a specific topology.
The resulting open loop function is:

$$H_{OL,v} = (k_{p,v} + \frac{k_{p,i}}{s}) \cdot \frac{1}{s \cdot C_{DC}} \tag{B.8}$$

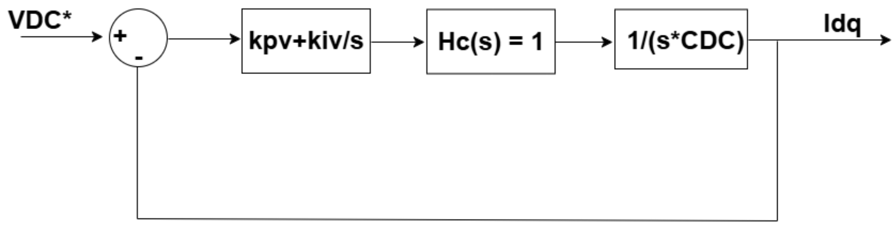

Figure B.2: Inverter Voltage Control loop in Laplace domain

The same high frequency approximation made in eq.B.9 for the current loop tuning is applied for the open loop voltage control, obtaining:

$$H_{OL,v}(s) \approx \frac{k_{p,v}}{s \cdot C_{DC}} \tag{B.9}$$

and the open loop crossover frequency presents a unitary module.

$$|H_{OL,v}(w_{bw,v})| \approx \frac{k_{p,v}}{s \cdot C_{DC}} = 1 \tag{B.10}$$

from which is possible to obtain the proportional gain as:

$$k_{p,v} = C_{DC} \cdot \omega_{bw,v} \tag{B.11}$$

The integral gain can be calculated with the same logic as before, obtaining:

$$k_{i,v} = k_{p,v} \cdot \frac{\omega_{bw,v}}{10} \tag{B.12}$$

The tuning calculations made for the inverter control loop, can be used to describe the boost control loop simply changing with the correct approximation the bandwidth and the crossover frequency of the system, looking at the switching frequency of the DC/DC converter.

PLL PI regulator tuning

The procedure shown in this section of the Appendix B is similar to the current and voltage loop tuning procedure described before. Starting from the high frequency approximation of the schematic presented in fig. 4.9, the open loop transfer function for the PLL becomes:

$$H_{OP,PLL} \approx \frac{k_{p,PLL \cdot |V_{dq}|}}{s} \tag{B.13}$$

$$H_{OP,PLL}(\omega_{bw,PLL}) \approx \frac{k_{p,PLL} \cdot |V_{dq}|}{s} = 1 \tag{B.14}$$

from which is possible to estimate the proportional and the integral gain for the phase-locked loop as:

$$k_{p,PLL} = \frac{\omega_{bw,PLL}}{|V_{dq}|} \tag{B.15}$$

$$k_{i,PLL} = k_{p,PLL} \cdot \frac{\omega_{bw,PLL}}{10} \tag{B.16}$$

Appendix C

MatLab code for LUT creation

LUT generating code

The behavior of the PV module in presence of an environmental characteristics variation, is performed with the creation of a 2D-LUT (Lookup Table) matrix, in which the photo-generated current values are modified and updated w.r.t a irradiance variation.
The lookup table follows the algebraic relations expressed in eq. 4.5 and 4.1.1 to compute the matrix, needed in the respective PLECS block subsystem used in the simulation.

The MatLab code reported is able to update the voltage and current variation parameter, and store the relative photogenerated current value in a matrix with a fixed dimension.

```
G=linspace(200,1000,5);
DeltaI=zeros(length(G));
DeltaV=zeros(length(G));
Isc=zeros(length(G));
Voc=zeros(length(G));

C2=(Vmp-Voc_stc)/log(1-Imp/Isc_stc);
C1=Isc_stc/(1-exp(-Voc_stc/C2));

%Isc and Voc Update due to temperature and G variation
for i=1:length(G)
    DeltaI(i)=Isc_stc*(G(i)/G0-1)+niIsc*(G(i)/G0)*(T0-T0);
```

```
    Isc(i)=Isc_stc+DeltaI(i);
    DeltaV(i)=niVoc*(T0-T0)-Rs*DeltaI(i);
    Voc(i)=Voc_stc+DeltaV(i);
end
V=linspace(0,60,500);
PV_I=real(zeros(length(V)+1,length(G)));
for i=1:length(V)
    for j=1:(length(G)+1)
        if j==1
            PV_I(i,j)=0;
        else
        PV_I(i,j)=Isc(j-1)-C1*exp(-Voc(j-1)/C2)*(exp(V(i)/C2)-1);
        if PV_I(i,j)<0
            PV_I(i,j)=0;
        end
        end
    end
end
save('PV_I.mat','PV_I');
```

The realized code is implemented for the chosen PV panel, with a parameter definition realized starting from tab.3.3 and 3.1.

Bibliography

[1] Union Espanola Fotovoltaica. «UNEF Annual Report 2024». In: *Forging The Transformation Towards Sustainability*. 2024 (cit. on pp. 3, 22).

[2] European Commission. «The Green Deal Industrial Plan». In: 2023 (cit. on p. 4).

[3] European Commission. «The Net Zero Industry Act». In: *Official Journal of the European Union*. 2024 (cit. on p. 4).

[4] European Commission. *The Critical Raw Materials Act*. http://data.europa.eu/eli/reg/2024/1252/2024-05-03. Online document (cit. on p. 4).

[5] Appa Renovables. «Estudio del Impacto Macroeconómico de las Energías Renovables en España 2023». In: *Asociación de Empresas de Energías Renovables APPA*. 2023 (cit. on pp. 4, 5, 22, 83).

[6] European Commission. *Integrated National Energy and Climate Plan Spain 2023-2030*. https://commission.europa.eu/publications/spain-final-updated-necp-2021-2030-submitted-2024_en. Online document (cit. on p. 5).

[7] Filippo Spertino. «Solar Photovoltaic Systems». In: *Renewable Energy Systems, PoliTo*. 2023-2024 (cit. on pp. 6, 8, 27, 34, 35, 55).

[8] Zahra Moradi-Shahrbabak, Ahmadreza Tabesh, and Gholam Reza Yousefi. «Economical Design of Utility-Scale Photovoltaic Power Plants With Optimum Availability». In: *IEEE Transactions on Industrial Electronics* (2014) (cit. on p. 12).

[9] HITACHI. *HITACHI HIVERTER NP215L Datasheet*. https://www.hitachi-hirel.com/pdf/catalogues/grid-tied-solar-inverters/grid_tied_solar_inverters_booklet.pdf. Online datasheet (cit. on p. 17).

[10] S-J. Choi T.N. Olayuwola S-H. Hyun. «Photovoltaic Modeling: A Comprehensive Analysis of the I-V Characteristic Curve». In: *Sustainability* (2024) (cit. on p. 35).

[11] Fabio Mandrile Iustin Radu Bojoi. «Power Electronics for E-Mobility, Polito». In: 2023-2024 (cit. on p. 51).

[12] IFINEON. *FF1200R12IE5 Datasheet*. https://www.infineon.com/dgdl/Infineon-FF1200R12IE5-DataSheet-v03_01-EN.pdf?fileId=5546d46259d9a4bf015a1d74b60a25ad. Online datasheet (cit. on p. 59).

[13] Onsemi. *NXH350N100H4Q2F2P1G Datasheet*. https://www.onsemi.com/download/data-sheet/pdf/nxh350n100h4q2f2p1g-d.pdf. Online datasheet (cit. on p. 60).

[14] IFINEON. *FF400R07KE4 Datasheet*. https://www.infineon.com/dgdl/Infineon-FF400R07KE4-DS-v03_00-en_de.pdf?fileId. Online datasheet (cit. on p. 60).

[15] International Renewable Energy Agency IRENA. *RENEWABLE POWER GENERATION COSTS in 2023*. https://www.irena.org/-/media/Files/IRENA/Agency/Publication/2024/Sep/IRENA_Renewable_power_generation_costs_in_2023.pdf. Online document (cit. on pp. 82, 83).

[16] International Energy Agency - Photovoltaic Power Systems Programme. *TRENDS IN PHOTOVOLTAIC APPLICATIONS 2024*. https://iea-pvps.org/trends_reports/trends-in-pv-applications-2024/. Online document (cit. on pp. 83, 87).